
CHAPTER 6

Reactivity and Dynamics at Liquid Interfaces

Ilan Benjamin

Department of Chemistry and Biochemistry, University of California, Santa Cruz, CA 95064, USA

INTRODUCTION

Many phenomena of interest in science and technology take place at the interface between a liquid and a second phase. Corrosion, the operation of solar cells, and the water splitting reaction are examples of chemical processes that take place at the liquid/solid interface.^{1,2} Electron transfer, ion transfer, and proton transfer reactions at the interface between two immiscible liquids are important for understanding processes such as ion extraction,^{3,4} phase transfer catalysis,^{5,6} drug delivery,⁷ and ion channel dynamics in membrane biophysics.⁸ The study of reactions at the water liquid/vapor interface is of crucial importance in atmospheric chemistry.^{9,10} Understanding the behavior of solute molecules adsorbed at these interfaces and their reactivity is also of fundamental theoretical interest. The surface region is an inhomogeneous environment where the asymmetry in the intermolecular forces may produce unique behavior.

Because of its importance, it is not surprising that the study of the neat liquid surface, as well as of solute adsorption, spectroscopy, and reactivity, goes back many years. However, up until the last decade of the twentieth century most of the experimental studies involved the measurement of macroscopic properties such as surface tension and surface potential,^{11,12} and generally speaking, the spectroscopic techniques employed lacked the specificity and

sensitivity required to probe the surface region. Although these techniques contribute significantly to our knowledge, they lack the ability to provide a detailed understanding at the molecular level.

In recent years, advances in a number of new experimental methods have provided unprecedented sensitivity and selectivity in the measurement of liquid interfacial phenomena. Prominent among these are nonlinear spectroscopic techniques such as Second Harmonic Generation (SHG) and Sum Frequency Generation (SFG), which probe the surface region selectively.^{13–15} These techniques have been used to explore the liquid/vapor interface^{16–18} and buried interfaces, such as liquid/liquid^{19–24} and liquid/solid interfaces,^{25–29} as well as biological interfaces.^{30,31} Other techniques that have been used in recent years to study liquid surfaces and interfaces include light scattering,^{32–36} X-ray and neutron scattering,^{34,37–44} atomic scattering,⁴⁵ fluorescence anisotropy decay,^{46,47} scanning electrochemical microscopy,^{48,49} infrared spectroscopy in a total reflection geometry,^{50,51} and X-ray absorption spectroscopy.^{52,53}

In parallel to these experimental approaches, much progress has been made in theoretical studies of liquid surfaces. Advances in the statistical mechanics of inhomogeneous fluids^{54–57} have contributed significantly to our understanding of the molecular structure of liquid/solid, liquid/liquid, and liquid/vapor interfaces. However, the mathematical complexity because of losing the spherical symmetry of the bulk has limited the application to mainly calculating a small number of properties (such as density profile, surface tension, and molecular orientation) of neat inhomogeneous liquids.⁵⁸

A major breakthrough in the theoretical understanding of the structure and dynamics of neat liquid interfaces, especially the behavior of reactive and nonreactive solutes adsorbed at these interfaces, has occurred over the past two decades thanks to advances in computer simulation methodology and the availability of high-speed computers. Computer simulations were initially used to test the validity of statistical mechanical approximations to calculating bulk and interfacial liquid molecular structure. However, their main contribution, together with experiments, has been to demonstrate the crucial role that the molecular structure of the liquid plays in understanding the spectroscopy, energy relaxation, and reactivity of solute molecules dissolved in the liquid.

While the long-standing picture of the solvent as a structureless medium has been very useful for offering a qualitative understanding of the solvent's effect on structure and dynamics, computer simulations and experiments clearly suggest that a microscopic molecular description of the solvent is necessary. This is particularly so for interfacial phenomena, because the interfacial region itself is only a few molecular diameters thick.

The purpose of this chapter is to discuss the computational tools that were developed to specifically address liquid interfacial systems and to summarize the microscopic insight gained about the structure and dynamics of neat liquid interfaces and the behavior of solute molecules adsorbed at these interfaces. Because most of these computational tools are based on molecular dynamics

and Monte Carlo simulations of liquids, about which many excellent review articles and books exist, we will refer the reader to these sources when needed. As far as the new physical insight that these tools provide, our focus will be on presenting unifying concepts rather than on results that are specific for a given system. Because the subject of liquid–solid interface simulations has already received good coverage in this series,^{59,60} we limit our discussion of these surfaces to presenting a contrasting view with the liquid/vapor and liquid/liquid interfaces.

We begin this chapter with a brief summary of the simulation methodology developed to deal specifically with liquid surfaces and interfaces. We then describe the application of this methodology to the neat interface. The focus is on molecular-level information that in recent years has been compared directly with experiments. This provides the necessary background for discussing the methodology and general insights that computer simulations provided for solute adsorption, transport, relaxation, and reactivity at liquid interfaces. The emphasis is on presenting general concepts that underlie different phenomena and focusing on the unique effect of the interface region in contrast with bulk behavior.

SIMULATION METHODOLOGY FOR LIQUID INTERFACES

Most simulation techniques applied to date to liquid interfaces are based on classical molecular dynamics and Monte Carlo methods. With few exceptions (discussed below), these techniques can be used straightforwardly to simulate the neat interface between a liquid and a second phase and to investigate the thermodynamics and dynamics of solute adsorption and reaction. There are several excellent books on the fundamentals of these techniques^{61–64} as well as free software available on the internet.⁶⁵ (For a library of free software, see <http://www.ccp5.ac.uk/librar.shtml>.)

Force Fields for Molecular Simulations of Liquid Interfaces

In the classical molecular dynamics method, the dynamics of a system composed of N particles are followed by numerically solving the 3 N -coupled Newton equations of motion:

$$m_i \frac{d^2 \mathbf{r}_i}{dt^2} = -\nabla_i U(\mathbf{r}_1, \mathbf{r}_2, \dots, \mathbf{r}_N) \quad [1]$$

where \mathbf{r}_i is the vector position of particle i with mass m_i . These particles are usually identified as the individual atoms in the molecules, but in many applications a particle can represent a group of atoms (“united” atom) or a fictitious

mass for modeling coupling to an external bath⁶⁶ or for describing fluctuating charges in a molecule (see below).

The key ingredient in a molecular dynamics (and a Monte Carlo) simulation is the potential energy function $U(\mathbf{r}_1, \mathbf{r}_2, \dots, \mathbf{r}_N)$ describing the interactions between all the particles. This is sometimes called the “force field” of the system. In principle, this function can be determined by solving the Schrodinger equation for the ground state energy as a function of all the particle positions. Because this is practical only for a system of a few atoms, the approach taken for simulating a condensed phase system composed of thousands of particles is an empirical representation of U in terms of simple functions that are determined by fitting experimental data and utilizing solutions of the Schrodinger equation to small parts of the system (e.g., by looking at a small cluster of molecules). There exists an extensive literature and many databases for empirical force fields used in simulations of condensed phase systems;^{67–70} here we give only a brief summary of the typical force field used in simulating liquid surfaces.

The simplest approach is to express the potential energy function as a sum of interactions between all pairs of particles belonging to different molecules (nonbonded interactions), plus a sum of the bonding interactions in each molecule:

$$U(\mathbf{r}_1, \mathbf{r}_2, \dots, \mathbf{r}_N) = \sum_{i < j} u(r_{ij}) + \sum_k U_{\text{intra}}^{(k)} \quad [2]$$

where u is called the pair potential and $U_{\text{intra}}^{(k)}$ is the function describing the intramolecular bonding interactions in molecule k . The pair potential u depends on the identity of the two particles i and j , which belong to two different molecules, and on the distance r_{ij} between these particles. A typical form of this pair potential represents the interaction between two particles as a sum of coulomb electrostatic energy and a Lennard-Jones 6–12 term:

$$u(r_{ij}) = 4\epsilon_{ij}[(\sigma_{ij}/r_{ij})^{12} - (\sigma_{ij}/r_{ij})^6] + q_i q_j / r_{ij} \quad [3]$$

In this simple approach, the two particles are assigned fixed charges q_i and q_j , which are determined by solving the Schrodinger equation for the individual molecule (or a small cluster), by fitting to experimental dipole moment values, or by fitting to other experimentally measured properties. The Lennard-Jones term includes r^{-12} repulsion and a $-r^{-6}$ attraction terms, which represent approximately the polarizabilities of the two particles and their sizes. These terms are expressed by the parameters ϵ_{ij} and σ_{ij} , respectively. In a system containing n different particle types, there are in principle $n(n+1)$ independent ϵ_{ij} and σ_{ij} parameters (e.g., $n = 5$ is needed to simulate the water/chloroform interface). However, the general practice is to assign to each particle type the “self” terms ϵ_{ii} and σ_{ii} and to use the “mixing rules”⁷¹ to obtain all the other parameters:

$$\epsilon_{ij} = \sqrt{\epsilon_{ii}\epsilon_{jj}}, \quad \sigma_{ij} = (\sigma_{ii} + \sigma_{jj})/2 \quad [4]$$

This is convenient for reducing the number of needed parameters. It is also useful for establishing the so-called transferable force field in which a set of parameters are assigned to atom types that can then be used for similar molecules.

Because the single particle self-parameters ϵ and σ are typically optimized to fit the bulk properties of a liquid with the “mixing rule” in place, there is no guarantee that Eq. [4] is optimal when interactions exist between molecules of different liquids, as is the case in simulating the interface between two different liquids (or mixtures of liquids). One approach is to use the mixing rules for the interactions between molecules of the same liquids but to fit the ϵ_{ij} and σ_{ij} parameters independently for the interactions between molecules of different liquids to reproduce interfacial properties such as surface tension.⁷² As an extreme example, a simple model of two immiscible Lennard-Jones atomic liquids might be one in which one uses a Lennard-Jones potential where the attractive term is altogether missing or reduced in size instead of Eq. [4] to describe the interactions between the two different atoms.^{73,74} A more general issue that has not received much consideration to date is whether potential energy functions fitted to properties of bulk liquids can even be used to simulate interfaces. We discuss this below in the context of many-body force fields.

While the pair approximation of Eq. [2] is efficient for computer simulations, a better agreement with experimental data can sometimes be achieved by utilizing more general force fields. n -Body potentials, which depend on the simultaneous positions of n particles with $n > 2$, provide a more refined description of condensed phase systems,⁷⁵ but only in a few cases have they been used for liquid surfaces.^{76,77} An obvious case where three-(or higher)-body potentials are necessary is when classical MD is used to model a chemical reaction. The simple A + BC atom exchange reaction, for example, has been modeled with the three-body LEPS potential.⁷⁸ The topic of potentials used to model chemical reactions will be further discussed in the section on reactivity at liquid interfaces.

An important subset of many-body potentials shown to be important for simulating interfacial systems are those referred to as polarizable force fields.^{79–96} Various aspects of polarizable force fields, especially for use in biomolecular modeling, is explained by Ren et al. in Chapter 3 of this volume. If one treats the fixed charges in Eq. [3] as parameters to be fitted to obtain the best agreement of the condensed phase simulations with experiments, in many cases one finds that the optimal values are considerably different from those obtained from a fit to a molecular (gas phase) dipole moment or from quantum calculations on isolated molecules. This is because in a condensed medium, the local electric field E_i (at the location of a particle i) is determined by all the fixed charges q_j and by all the induced dipoles \mathbf{m}_j in the system:

$$\mathbf{E}_i = \sum_{j \neq i} \left[\frac{q_j \mathbf{r}_{ij}}{r_{ij}^3} + \mathbf{T}_{ij} \cdot \mathbf{m}_j \right], \quad \mathbf{T}_{ij} = \frac{1}{r_{ij}^3} \left(\frac{3\mathbf{r}_{ij} \circ \mathbf{r}_{ij}}{r_{ij}^2} - 1 \right) \quad [5]$$

where $\mathbf{m}_i = \alpha_i \mathbf{E}_i$, $\mathbf{r}_{ij} = \mathbf{r}_i - \mathbf{r}_j$, and \mathbf{T}_{ij} is the dipole–dipole matrix. Because the value of \mathbf{E}_i needed to determine \mathbf{m}_i depends on the value of \mathbf{m}_i itself, Eq. [5] must be solved iteratively. Once the values of \mathbf{m}_i converge, the additional energy due to this many-body effect is given by

$$U_{\text{pol}} = -\frac{1}{2} \sum_i \mathbf{m}_i \cdot \mathbf{E}_i \quad [6]$$

A simpler approach that is directly related to the observation that the effective charges in the two-body approximation are different from the fixed gas phase charges is to treat the charges in Eq. [2] as fluctuating dynamic variables. These approaches and others are discussed at length in another chapter in this series.⁹⁷

It is important to keep in mind that the simple pair approximation in Eq. [2] is in fact an “effective” two-body description that takes into account the real many-body nature of the system implicitly through the fitting procedure. If this expression is modified by adding any of the above types of many-body interactions, the parameters that go into the two-body term must be refitted.

The second term in Eq. [2] represents the intramolecular potential energy. This term accounts for vibrations and internal rotations in the molecule relative to the equilibrium configuration. When internal motion is of no interest or consequence, it is possible to keep the molecule rigid using several well-known algorithms.^{63,64,98} If the vibrational motion is important (e.g., when calculating vibrational spectra or when accurate modeling of large energy transfer is required), vibrational terms must to be included. The standard choice is to model the bond stretching and bending using harmonic (quadratic) terms, the internal rotations around bonds (torsions) using a series of cosine terms, and to include Lennard-Jones interactions between nonbonded atoms. References to the force field literature mentioned above contain detailed information about these types of potential energy functions and extensive tables of parameters.^{67–70} In closing this section, we note that special effort has been made over the past decades to develop accurate force fields for simulating bulk water, and, in recent years, these force fields have been carefully evaluated for their ability to describe interfacial water. For a detailed survey of water models up to the turn of the twenty-first century, see Ref. 99. More recent water models developed specifically to address properties of interfacial water will be discussed below.

Boundary Conditions and the Treatment of Long-Range Forces

Molecular dynamics or Monte Carlo simulations of bulk liquids employ 3-dimensional (3D) periodic boundary conditions (PBC) (using typically a cubic or a truncated octahedron box), which are designed specifically

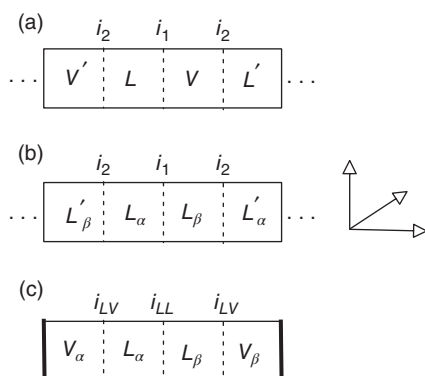


Figure 1 A schematic representation of three typical boundary conditions used in the simulation of the liquid/vapor and liquid/liquid interfaces. See text for details.

to *eliminate* surface effects. We must ensure that the boundary conditions maintain a well-defined and stable interface region. In a laboratory setup, the planar interface between a liquid and its vapors or between two liquids is maintained by gravity. Most simulations of liquid/vapor and liquid/liquid interfaces establish a planar surface by using period boundary conditions in two or three dimensions as depicted in Figure 1. In all of the simulation geometries described below and for the rest of this chapter, we will take the planar interface to be perpendicular to the z axis.

In Figure 1a, a 3D PBC with rectangular symmetry is used to ensure the planar liquid/vapor interface. L and V denote the regions in the central simulation box containing the liquid and vapor phases, respectively. L' and V' are the periodic replicas. In this geometry, there are two independent liquid/vapor interfaces: i_1 and i_2 . (The two planes denoted by i_2 are the opposite faces of the central simulation box, so they are the same plane.) This geometry is typically prepared by starting with a bulk liquid cubic box and extending it along the z direction. Depending on the density of the starting box and the temperature of the system, a stable liquid and vapor phase will coexist.

In Figure 1b, the interface between two immiscible liquids, L_α and L_β , is prepared using a 3D PBC similar to that in Figure 1a. i_1 and i_2 are two independent liquid/liquid interfaces. The central simulation box contains the molecules labeled L_α and L_β , and their replicas are along the z directions. This simulation geometry is created by bringing together two bulk cubic boxes containing the two liquids and equilibrating the system. It has the advantage of using both liquid/liquid surfaces for increased statistics. However, because this simulation geometry typically equilibrates to $p \neq 1$ atm, it must be done at constant pressure (see below). There are additional complications when one studies solute molecules that are constrained to the interface, which will be discussed in the section on Solutes at Interfaces.

To avoid possible interaction between the two liquid/liquid interfaces and other complications, a 2D PBC geometry to simulate a single liquid/liquid interface is depicted in Figure 1c. Here, after bringing the two liquid boxes into contact, the simulation box is extended so that each liquid forms an interface with its own vapor. Only one liquid/liquid interface (denoted in the figure by i_{LL}) exists, as the system is not replicated along the z direction. To prevent mixing of the two vapor phases, a reflecting wall is set at the opposite faces of the box (thick lines).

Related to the simulation geometry is the treatment of long-range forces in molecular simulations. It has long been recognized that due to the finite and relatively small size of the simulation boxes, treating intermolecular interactions at large distances must be approximated, and correction for these approximations must be included when calculating thermodynamic properties. The problem is especially acute for the slowly varying electrostatic interactions. While this topic is discussed extensively in the general references given above,^{61–64} we note below some specific points.

The short-range Lennard-Jones interactions may be truncated at a distance R_c (typically done with a continuous switching function with a continuous first derivative⁶¹), which can be as small as 2.5σ . One expects an error of only about 1% in the total internal energy for this value of R_c . However, the error in liquid-surface-related properties is much higher: 5% and 20% errors in the liquid and vapor densities, respectively, and 50% error in the surface tension.¹⁰⁰ Thus, longer cutoff distances and corrections must be included to obtain reliable and consistent results.^{101,102}

In contrast, truncation at a computationally feasible (i.e., small) value of R_c produces artifacts when the system is strongly ionic because the potential energy is dominated by the slowly varying $1/r$ terms.^{103,104} To address this, a popular approach known as Ewald or lattice sum (similar to the one used to calculate the lattice energy of ionic crystals) is used to sum the electrostatic interactions in the simulation box and all of its replicas. This is done by rewriting the sum of the $1/r$ terms as a sum of a rapidly converged series in real space (so a small cutoff can be used for these terms) and a much more slowly varying smooth function that can be approximated by a few cosine and sine terms in reciprocal (k) space.^{61,105,106} These are expensive calculations that scale like $N^{3/2}$, where N is the number of particles but can be made more efficient (scales like $N \log N$) by approximating the k -space calculations with a discrete convolution on an interpolating grid, using the discrete Fast-Fourier transforms (FFT). Several implementations have been discussed.^{107–111}

To sum the long-range coulomb interactions for an interfacial system, one can use the 3-dimensional Ewald (3DE) method and its variants mentioned above, provided that the 3D-periodic boundary condition geometry is used (see Figure 1a and b). If the system is only periodic in two dimensions (a “slab” geometry, see Figure 1c), one must use a 2-dimensional version (2DE), which is computationally expensive. There are ways to approximate the Ewald sum

in 2D using the 3DE equations by adding a large empty space in the direction normal to the interface,¹¹² or by using other correctional terms.^{113,114} Promising new method for fast Ewald summation in planar/slab-like geometry, which uses spectral representation in terms of both Fourier series and integrals, has been suggested recently.¹¹⁵

It should also be mentioned that approaches for treating long-range coulomb interactions with a pairwise compensation scheme have been developed.^{116–118} They are based on shifting and damping the pair potential energy such that this function and its first and second derivatives decay continuously to zero at the cutoff distance. Physically, this method is equivalent to placing countercharges at the cutoff sphere. Variations of this method were described and tested for different systems¹¹⁸ and for liquid interfaces¹¹⁹ by comparison to infinite lattice sums and to the Ewald method.

Statistical Ensembles for Simulating Liquid Interfaces

In classical molecular dynamics, phase space is sampled by following the particles' trajectories by solving the deterministic equations of motion using the forces on the particles. Constant energy trajectories provide a microcanonical sampling of phase space. Several algorithms were developed for keeping the temperature and pressure fixed by a modification to these dynamics, which allows for the sampling of the isothermal (*NVT*, also called canonical) and the isothermal-isobaric (*NPT*) ensembles.^{61–64,120,121} In the thermodynamic limit ($N \rightarrow \infty$), ensemble averages calculated by the different ensembles should be equal, but, in simulations with relatively small N , the proper choice of an ensemble can accelerate the convergence to the thermodynamic equilibrium value.

When simulating a liquid/vapor interface, an *NVT* ensemble is a straightforward choice, because in this two-phase, single component system, fixing the temperature determines the vapor pressure. The choice of volume determines the number of molecules in the vapor phase and thus its density. The situation at a liquid/liquid interface is more complicated and depends on the type of boundary conditions used. Zhang et al. discussed five different statistical ensembles that can be used to simulate the liquid/liquid interface with the boundary conditions of Figure 1b.¹²² The available choice is in part because of the fact that the normal pressure, tangential pressure, and surface tension can be fixed independently. Different ensembles can be useful for different applications. For example, to study the water/oil interface a convenient ensemble is constant normal pressure and constant surface area ensemble. But for computing pressure/area isotherms of adsorbed monolayers, the ensemble in which the tangential pressure and the length normal to the surface are held constant is more appropriate. Computing the surface tension is discussed in the section "The Neat Interface."

Comments About Monte Carlo Simulations

If one is interested in equilibrium canonical (fixed temperature) properties of liquid interfaces, an approach to sample phase space is the Monte Carlo (MC) method. Here, only the potential energy function $U(\mathbf{r}_1, \mathbf{r}_2, \dots, \mathbf{r}_N)$ is required to calculate the probability of accepting random particle displacement moves (and additional moves depending on the ensemble type^{61,123}). All of the discussion above regarding the boundary conditions, treatment of long-range interactions, and ensembles applies to MC simulations as well. Because the MC method does not require derivatives of the potential energy function, it is simpler to implement and faster to run, so early simulations of liquid interfaces used it.^{124,125} However, dynamical information is not available with this method. We also point out here that the MC method can be used to simulate phase equilibria without creating physical contact between the phases (no interface present). This is done in the Gibbs Ensemble Monte Carlo (GEMC) method proposed by Panagiotopoulos¹²⁶ and applied to many systems (e.g., water phase equilibria¹²⁷). The GEMC method involves two simulation boxes, one of which includes a bulk liquid phase and the other a vapor phase at the same temperature. In addition to the usual particle displacement moves in each box, the volume is allowed to change, and particles can be exchanged between the boxes.

THE NEAT INTERFACE

The structure and dynamics of the neat (no solute present) interface between a liquid and its vapor or between two immiscible liquids have been the subjects of numerous theoretical, computational, and experimental studies. Molecular-level insight was first provided by MD and MC simulations in the late 1970s. The first MC simulation of a liquid/vapor interface was used to calculate the density profile and surface tension of a system containing 129 Lennard-Jones particles by applying an external potential to keep the system stable.¹²⁴ The first MD simulation followed a few years later.¹²⁸ The system studied is the liquid–vapor interface of molten potassium chloride containing either 288 or 504 ions using the two-dimensional periodic boundary condition scheme. The computed surface tension at a temperature just above the melting point was within 30% of the experimental value. Self-diffusion at the interface is enhanced by 50% or more in comparison with the bulk, particularly for the direction perpendicular to the interface. The first study of a neat liquid/liquid interface was an MC investigation by Linse of the water/benzene interface.¹²⁵ That was followed by molecular dynamics studies by Smit¹²⁹ and by Meyer, Mareschal, and Hayoun¹³⁰ of a model liquid/liquid interface made from Lennard-Jones particles that were kept immiscible by tuning their intermolecular interactions. Density profiles and structural properties were calculated in all of these studies.

This activity has accelerated significantly in the past few decades and has been documented in several dozen articles, whose main results and insights are discussed below. A noteworthy point is that much of the computationally derived insight preceded experimental verification. This has been forthcoming in recent years with the development of nonlinear spectroscopy and other highly specific and sensitive experimental techniques. Today the experimental and computational approaches are an integral part of research in this field. We now summarize the insight gained from simulations and, whenever available, briefly provide consistent experimental evidence for it. Our main interest in the neat interface is to provide the background needed for understanding the behavior and reactivity of solute molecules adsorbed at the interface that will be covered later.

Density, Fluctuations, and Intrinsic Structure

In a bulk homogeneous liquid, the longtime (or ensemble) average of the number of particles $\langle n \rangle$ occupying any region of volume v depends on the temperature and pressure, not on the spatial location. The density of the liquid $\rho_L = \langle n \rangle / v$ is constant. In contrast, at a planar liquid/vapor or liquid/liquid interface the average density depends on the location z along the interface normal. The density profile is formally given by

$$\rho(z) = \left\langle \frac{1}{A} \sum_{i=1}^N \delta(z - z_i) \right\rangle \quad [7]$$

where A is the surface area, z_i is the coordinate of particle i along the interface normal, N is the total number of particles, and δ is the Dirac delta function. In practice, the density profile is calculated by a coarse-graining procedure: The simulation system is divided into slabs of thickness d parallel to the surface. If $n(z)$ is the average number of particles in a slab whose center is at z , then $\rho(z) = n(z)/(Ad)$. d needs to be large enough to get a smoothly varying ρ but small enough to be on the scale where ρ changes substantially. Typical values of d used are 1–3 Å.

Figure 2 depicts typical shapes of the density profile of liquids. Panel A shows the density profile (reduced units) of a Lennard-Jones liquid at equilibrium with its vapor at two different (reduced) temperatures. These profiles have been calculated and reported extensively in the literature using MD, MC, and several approximate statistical mechanical theories.^{55,57} The profiles shown in panel A are reproduced from the most accurate molecular dynamics simulations to date.¹³¹ Similar profiles are obtained for many other molecular liquids such as water^{132,133} and alcohols.¹³⁴ The density changes monotonically from the bulk liquid density ρ_L to the bulk vapor density ρ_V over a distance of a few molecular diameters, that is, 4–10 Å. It can be fitted with reasonably good

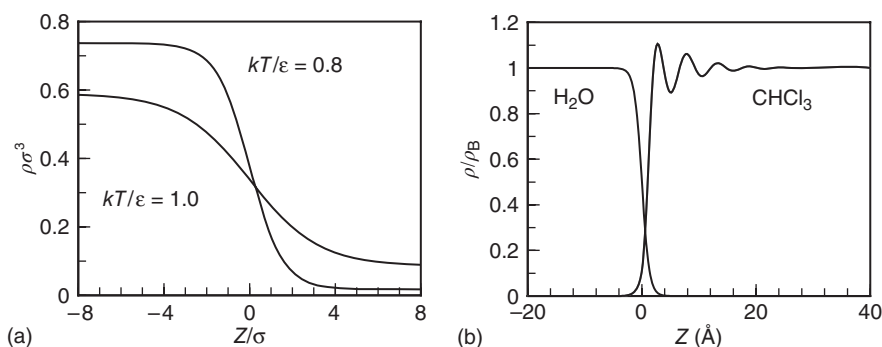


Figure 2 (a) Density profiles (reduced units) of the liquid/vapor interface of a Lennard-Jones fluid at two temperatures (reduced units). Data adapted from Ref. 131. (b) Density profile of the water/chloroform liquid/liquid interface at $T = 298\text{K}$. (Adapted with permission from Ref. 635. Copyright 2010 American Chemical Society.)

accuracy to the following expression (obtained from the van der Waals mean field approximation⁵⁵):

$$\rho(z) = 1/2(\rho_L + \rho_V) - 1/2(\rho_L - \rho_V) \tanh(z/2\delta) \quad [8]$$

where the liquid bulk phase occupies the region $z < 0$, $z = 0$ is the position where the density is equal to the average density of the two bulk phases, and δ is a measure of the interface width. A common way to express this width is to note the distance over which the density changes from 90% to 10% of the bulk density. This is equal to 4.4δ if the mean field expression for ρ (Eq. [8]) is used. As the temperature increases, the width of the liquid/vapor interface increases (further discussed below).

The density profile is used to define the Gibbs Dividing Surface (GDS), used extensively in thermodynamic analysis of the system as well as (a somewhat crude) expression for the average location of the interface. The GDS is defined as the plane $z = z_G$ parallel to the surface, such that the molecular “deficit” on the bulk side ($z < z_G$) is balanced exactly by the “surplus” on the vapor side ($z > z_G$):

$$\int_{z_L}^{z_G} (\rho(z) - \rho_B) dz + \int_{z_G}^{z_V} (\rho(z) - \rho_V) dz = 0 \quad [9]$$

where z_L and z_V are locations in the bulk liquid and vapor phases, respectively. It is easy to confirm that for the density profile of Eq. [8], $z_G = 0$. The GDS is approximately where the water density is half the bulk liquid value.

In Figure 2 panel B we show a typical liquid/liquid density profile. While the water density looks similar to a liquid/vapor density profile, the organic liquid (chloroform, in this case) density exhibits dampened oscillations. While the

source of these oscillations (which is well understood to represent molecular packing when a liquid is in contact with a solid) is not quite clear here; these oscillations have been observed in many liquid/liquid simulations^{93,125,135–143} and have also been predicted by classical statistical mechanics density functional calculations.¹⁴⁴ For example, molecular dynamics simulations of two immiscible Lennard-Jones liquids revealed stable equilibrium oscillatory structures in the density profiles, but those oscillations were reduced significantly when the surface area was increased.¹³⁷ A more recent MD study and density functional calculation were carried out on a similar model liquid/liquid interface where Lennard-Jones particles are kept immiscible by reducing the attractive interaction between unlike particles. The density profiles of the liquids display oscillations that vanish when approaching the liquid–vapor coexistence, while the total density of the system shows a significant depletion at the interface.¹⁴⁵ However, X-ray reflectivity studies of two different water/oil interfaces do not support with the existence of this depletion.¹⁴⁶

At the liquid/liquid interface, no unique GDS exists because an equation similar to Eq. [9] can be used to define a dividing surface with respect to either liquid by setting $\rho_V = 0$. If z_A and z_B are locations in bulk liquid A and liquid B, respectively, the GDS with respect to liquid A is given by

$$z_G(A) = z_A + \frac{1}{\rho_A^{\text{bulk}}} \int_{z_A}^{z_B} \rho_A(z) dz \quad [10]$$

where $\rho_A(z)$ is the density profile of liquid A assumed to vary from $\rho_A = \rho_A^{\text{bulk}}$ at $z = z_A$ to $\rho_A = 0$ at $z = z_B$. An analogous expression for the GDS defined with respect to liquid B can be written. In discussing the water/liquid interface, we will define the GDS with respect to the water density. As in the case of the liquid/vapor interface, the GDS is close to the plane where the water density is about half the bulk value.

The average density profile gives a useful indication of the thickness of the interface region, but any fluctuations in density along the normal and in the xy plane parallel to the interface are averaged out. While these fluctuations exist even in a homogeneous liquid, their size and the range of their correlations are much more evident at an interface. We will also see later that they are important for understanding solute behavior at the interface. A simple framework for characterizing density fluctuations at the interface is the continuum-level Capillary Wave (CW) theory. This theory has been discussed extensively.^{55,56} Here, we note briefly some useful relations and focus on molecular dynamics simulations that have been used to characterize the density fluctuations and to test the validity of CW theory down to a molecular-length scale.

Capillary wave theory considers the density variation at the interface to be the result of the superposition of thermally excited density fluctuations on a bare intrinsic profile. Mathematically, the instantaneous local density at a

location $\mathbf{r} \equiv (x, y, z) \equiv (\mathbf{s}, z)$ is given by

$$\rho(\mathbf{r}) = \rho_A + (\rho_A - \rho_B)H[\zeta(\mathbf{s}) - z] \quad [11]$$

where $H(u)$ is the step function: $H(u < 0) = 0$, $H(u > 0) = 1$ and $z = \zeta(\mathbf{s})$ is a two-dimensional curved surface separating the two phases whose bulk densities are ρ_A and ρ_B . Snapshots of molecular dynamics simulations of liquid/vapor and liquid/liquid interfaces are qualitatively consistent with this ideal view, and this will be quantified below. The curved surface fluctuates due to thermal motion, and the average over all these fluctuations gives rise to the density profile. CW theory approximates the free energy associated with these fluctuations^{55,56} and shows that ζ is a random Gaussian variable with probability distribution $P(\zeta) = (2\pi\langle\zeta^2\rangle)^{-1/2} \exp[-\zeta^2/2\langle\zeta^2\rangle]$ (without loss of generality $\langle\zeta\rangle$ is taken to be zero), in which the average square fluctuations are given by

$$\langle\zeta^2\rangle = \frac{k_B T}{4\pi\gamma} \ln \frac{1 + 2\pi^2 l_c^2 / \xi_b^2}{1 + 2\pi^2 l_c^2 / A} \quad [12]$$

where k_B is the Boltzmann constant, T the temperature, γ the surface tension, A the system surface area, ξ_b a molecular length scale taken to be the bulk liquid correlation length (defined as the distance where the bulk liquid radial distribution function's asymptotic value is equal to 1), and $l_c = [2\gamma/(g|m_A\rho_A - m_B\rho_B|)]^{1/2}$ is called the capillary length and is on the order of a few millimeters (g is the gravity constant and m_A and m_B are molecular masses). Performing the average of Eq. [11] over ζ gives a density profile that is mathematically similar in shape to the mean field expression (Eq. [8]):

$$\rho(z) = 1/2(\rho_A + \rho_B) - 1/2(\rho_A - \rho_B)\text{erf}(z/\sqrt{2\langle\zeta^2\rangle}) \quad [13]$$

where erf is the error function. In the case of the liquid/liquid interface, this gives the total density at the location z . $\sqrt{\langle\zeta^2\rangle}$ is a measure of the interface width (more precisely, the distance over which the density changes from 90% to 10% of the bulk density, which is $1.51\sqrt{\langle\zeta^2\rangle}$). Equation [12] shows that in the thermodynamic limit ($A \rightarrow \infty$), the surface width diverges as $(-\ln g)^{1/2}$, while at zero gravity one obtains

$$\langle\zeta^2\rangle = \frac{k_B T}{4\pi\gamma} \ln(A/\xi_b^2) \quad [14]$$

and the width diverges in the thermodynamic limit. While the issue of the existence of the interface at zero gravity is not completely clear,¹⁴⁷ using Eq. [14] for systems with sizes typically used in computer simulations is acceptable because for these systems $\xi_b \ll l_c \gg \sqrt{A}$, and Eq. [12] reduces to Eq. [14].

Molecular dynamics simulations have been used to test the validity of the CW theory down to distances comparable to ξ_b . Equation [14] predicts a specific dependence of the interface width on the temperature. Simulations at different temperatures can be used to determine $\langle \zeta^2 \rangle$ (by fitting the density profile to Eq. [13]). This, combined with surface tension calculations (see below), can be used to verify that $\sqrt{\langle \zeta^2 \rangle}$ is proportional to $\sqrt{T/\gamma}$. Figure 3 shows this plot generated using the data published in the very recent million particles simulation of the Lennard-Jones liquid/vapor interface.¹³¹ As can be seen, the relation in Eq. [14] holds quite well at low T . Another simple approach is to obtain ξ_b from the bulk radial distribution function ($g(\xi_b) \approx 1$) and confirm the validity of Eq. [14] using the independently calculated surface tension and $\langle \zeta^2 \rangle$, as has been done for several liquid/liquid interfaces.^{135,138} Alternatively, if several simulations with different surface areas are performed, Eq. [14] suggests that a plot of $\langle \zeta^2 \rangle$ versus $\ln A$ should be a straight line with a slope of $k_B T/4\pi\gamma$.^{142,143,148}

A more direct test of the underlying assumptions of CW theory can be done by computing the spectral representation of the fluctuating surface $z = \zeta(\mathbf{s})$. This surface is represented by the superposition of capillary waves of different wave numbers \mathbf{q} :

$$\zeta(\mathbf{s}) = \sum_{\mathbf{q}} \alpha(\mathbf{q}) e^{i\mathbf{q} \cdot \mathbf{s}}, \quad \alpha(0) = 0 \quad [15]$$

where $\mathbf{q} = (2\pi/L)(n_x, n_y)$, L is the box length and $(n_x, n_y = \pm 1, \pm 2, \dots L/\xi_b)$, so each mode \mathbf{q} contributes $\langle \alpha(\mathbf{q})\alpha(-\mathbf{q}) \rangle$ to the average of the square width. The

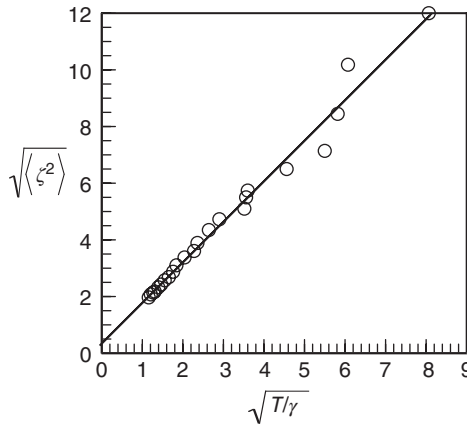


Figure 3 A test of capillary wave theory for a Lennard-Jones liquid/vapor interface. The circles represent independent simulations of the interface width at different temperatures. γ is the surface tension. (Data adapted from Ref. 131. Copyright 2012 American Institute of Physics.)

detailed calculations of CW theory give:⁵⁵

$$\langle \alpha(\mathbf{q})\alpha(-\mathbf{q}) \rangle = \frac{kT}{\gamma L^2(\mathbf{q}^2 + 2/\xi_b^2)} \quad [16]$$

For a typical system size used in simulation, $q = |\mathbf{q}| \gg \xi_b^{-1}$, and a plot of $\log \langle \alpha(\mathbf{q})\alpha(-\mathbf{q}) \rangle$ versus $\log q$ should be a straight line with slope 2. The key to this approach is determining the instantaneous surface $z = \zeta(\mathbf{s})$. This can be accomplished by finding the contact points (on a grid) between a probe sphere of a fixed radius and the interfacial molecules¹⁴⁹ once the set of interfacial molecules is determined.^{133,150,151} Another approach is to construct

a coarse-grain density by a convolution of the 3D density field $\sum_{i=1}^N \delta(\mathbf{r} - \mathbf{r}_i)$ with a Gaussian function.¹⁵² Jorge et al. recently reviewed these methods.¹⁵³

Experimental measurement of the density variation at liquid/vapor and liquid/liquid interfaces down to the nanometer length scale is possible with X-ray and neutron reflectivity measurements.⁴³ In a test of capillary wave theory, X-ray reflectivity was used to study the interface between water and n-alkanes, C_nH_{2n+2} with $n = 6-10, 12, 16$, and 22 . For all interfaces except the water-hexane ($n = 6$) interface, the interfacial width disagrees with the prediction of capillary wave theory. However, the variation of the observed interfacial width $\langle \zeta^2 \rangle_{\text{obs}}$ with the number of carbon atoms can be described by combining the capillary wave prediction for the width $\langle \zeta^2 \rangle_{\text{cap}}$ (Eq. [12]) with a contribution that takes into account the finite molecular size:

$$\langle \zeta^2 \rangle_{\text{obs}} = \langle \zeta^2 \rangle_{\text{cap}} + \sigma_0^2 \quad [17]$$

where σ_0 was found to match the radius of gyration of the shorter alkane molecules or the bulk correlation length for the longer alkanes.¹⁵⁴ A number of simulations have later demonstrated the applicability of Eq. [17].^{142,143,148}

An additional contribution to the interface width due to the finite molecular size can also be demonstrated by the calculation of the so-called intrinsic density profile. This profile can be thought of as a generalization of the simple zero thickness assumption, which is implicit in the step function representation in Eq. [11]. The intrinsic density profile can be obtained by computing the density relative to the instantaneous location of the dividing surface $\zeta(\mathbf{s})$:^{56,140,142,143,155,156}

$$\rho_{\text{int}}(z, q) = \left\langle \frac{1}{A} \sum_{i=1}^N \delta(z - z_i + \zeta(\mathbf{s}_i; q)) \right\rangle \quad [18]$$

where $q = |\mathbf{q}|$ is the wavevector value (see Eq. [15]) determining the resolution at which the instantaneous surface ζ is computed. The intrinsic density profile essentially removes from the average smooth density profile the blurring

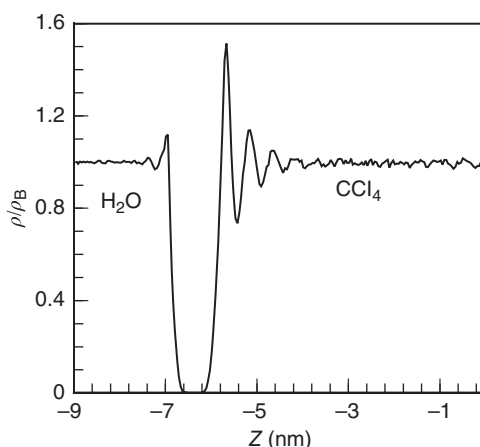


Figure 4 Intrinsic normalized density profiles for water and CCl_4 obtained by selecting the optimal grid resolution (see text). (Adapted with permission from Ref. 153. Copyright 2010 American Chemical Society.)

effect of the capillary fluctuations. An example of the intrinsic density profile of water and of carbon tetrachloride at the liquid/liquid interface is presented in Figure 4. In this example, the intrinsic surface $\zeta(s)$ is determined (for each liquid independently) using the grid method mentioned above, with a grid size given by the largest atomic site in each liquid. Other methods are reviewed in the paper by Jorge et al., from which this figure was reproduced.¹⁵³ Note the oscillatory density profile of the water, reflecting an underlying layered structure similar to that from the oxygen–oxygen radial distribution function $g(r)$ (see the discussion of $g(r)$ below). Demonstrated below is that other properties of the neat interface and of solute molecules adsorbed at the interface can also be described relative to the intrinsic surface.

Several other approaches for demonstrating the fact that a liquid surface is a rough but relatively sharp region of a two-phase system have been discussed. For example, by showing that the probability distribution of the surface height (defined as the maximum value of $\zeta(s)$ when s is sampled over a grid of varying sizes^{125,135,142,143}) is a Gaussian. As will be discussed later, the local density and its fluctuations have a profound effect on the spectroscopy, dynamics, and reactivity of adsorbed solute molecules.

Surface Tension

The surface tension of a liquid/vapor or liquid/liquid interface can be calculated readily from MD or MC simulations. The goal of these calculations has typically been to test the validity of the force fields utilized, since experimental data on surface tension are readily available. As discussed earlier, the force fields used in simulations of interfacial systems are often optimized to reproduce bulk

liquid properties, so there is no guarantee that they will independently reproduce this surface-specific property. It turns out that most simulations that use the simple mixing rules to determine the interactions between the molecules of two different liquids seem to give reasonable results, however.⁷²

Several approaches for calculating the surface tension have been developed and are briefly summarized here. The fundamental definition of the surface tension γ depends on the statistical mechanical ensemble used. For example, at constant N, V, T :

$$\gamma = \left(\frac{\partial F}{\partial A} \right)_{N,V,T} \quad [19]$$

where F is the Helmholtz free energy. Other expressions may be written, as discussed in Chapter 2 by Rowlinson and Widom.⁵⁵ Beginning with this definition, several approaches for calculating the surface tension between two phases from molecular simulations have been developed, and they are generally called the “thermodynamic route.” These methods are based on directly calculating the change in the system’s Helmholtz free energy associated with a change in the interfacial area at constant particle number, volume, and temperature. The performance of these thermodynamic techniques was recently presented by Errington and Kofke.¹⁵⁷

Other approaches for computing the surface tension start from the statistical mechanical expression for the Helmholtz free energy or for the pressure. The Kirkwood–Buff formula for the surface tension of a liquid/vapor interface of an atomic liquid described by the pair potential approximation is:

$$\gamma = \frac{1}{2A} \left\langle \sum_{i>j} \frac{r_{ij}^2 - 3z_{ij}^2}{2r_{ij}} \frac{\partial u}{\partial r_{ij}} \right\rangle \quad [20]$$

where the sum is over all pairs of atoms and the average is in the canonical ensemble. The factor of $1/2$ accounts for the existence of two surfaces. Generalized to molecular fluids, the formula is¹²⁵

$$\gamma = \frac{1}{2A} \left\langle \sum_{i>j} \frac{r_{ij}^2 - 3z_{ij}^2}{2r_{ij}} \sum_{m,n} \frac{\mathbf{r}_{ij} \cdot \mathbf{r}_{mn}}{r_{ij}r_{mn}} \frac{\partial u}{\partial r_{mn}} \right\rangle \quad [21]$$

where r_{mn} is the distance between atom m that belongs to molecule i and atom n that belongs to molecule j , and r_{ij} is the distance between the centers of mass of molecules i and j . This formula can also be used at the liquid/liquid interface (without the factor of $1/2$ if we have a single interface). Long-range corrections to the surface tension calculated with this expression assume that for distances $r > r_c$ (the simulation cutoff distance) one may set the radial distribution function to 1 when calculating the ensemble average in the above equations.¹⁵⁸

These long-range corrections take the form of integrals involving the pair interaction energy, and they can contribute significantly (10–30%), especially at high temperatures. Early experience using the Kirkwood–Buff formula resulted in slow convergence due to large fluctuations,¹²⁵ but with the brute force computational power available today, this no longer seems to be an issue.

In the Irving and Kirkwood method¹⁵⁹ the surface tension is expressed as the integral over the difference between the local components of the pressure tensor

$$\gamma = \int (p_N(z) - p_T(z)) dz \quad [22]$$

where $p_N(z)$ and $p_T(z)$ are the normal and tangential components of the pressure tensor along the normal to the surface, respectively, and the integral is over the region that includes the interface (in a bulk homogeneous fluid, $p_N(z) = p_T(z)$). In practice, the components of the pressure tensor are calculated in slabs parallel to the interface, and the integral is replaced by a sum over these slabs. The expression for the pressure tensor is similar to that for the pressure calculated in a simulation of homogeneous systems, except that there is ambiguity in the interfacial term because no unique way exists to determine which intermolecular forces contribute to the force across a given slab. These choices are discussed briefly in the book by Rowlinson and Widom⁵⁵ and in more detail in Refs. 160–162. Expressions for the long-range corrections in the Irving–Kirkwood method were also developed.¹⁶³ We should mention that it is also possible to rewrite the Kirkwood–Buff formula as a sum of local contributions from different slabs.¹⁶⁴

It is important to point out that being an equilibrium property, the surface tension can be calculated in a molecular dynamics or Monte Carlo simulation. The force calculations are of course already done in the MD code, but the calculation of the potential energy derivatives needs to be added to the MC code if the Kirkwood–Buff or Irving–Kirkwood methods are used.

The methods discussed above have been used extensively in the literature, recent example of which is a calculation of the surface tension of six common water models at different temperatures.¹⁶⁵ Particular noteworthy is the recent detailed calculation of the surface tension at the liquid/vapor interface for a series of alcohols by MC simulations, using many of the mechanical and thermodynamics methods described above. The surface tension, saturated liquid densities, and the critical points compare well with experiments.¹³⁴

Molecular Structure

The interface region is characterized at the molecular level by a strong asymmetry in the molecular interactions due to the gradient in the number density along the interface normal. The pair-interactions themselves may effectively be different in the bulk versus the interface. For example, if a polarizable force field is used, the different local electric fields in these two regions will induce a

different electric dipole moment on the interfacial molecules, resulting in different effective charges on these molecules. Consequently, molecular structure and dynamics at the interface may differ significantly from the bulk. Molecular simulations have been particularly useful for elucidating this effect especially because experimental probes of interfacial molecular structure is challenging. In this section, we briefly discuss the most important molecular level structural properties derived from MD and MC simulations over the past 2–3 decades. This is followed by a discussion of dynamical properties of the neat interface.

Molecular Orientation

The orientation of molecules at interfaces impacts other structural properties (such as hydrogen bonding) and surface reactivity and, accordingly, has been the subject of statistical mechanical theories,¹⁶⁶ simulations, and experiments.^{19,167–173} Any axis that is fixed in the molecular frame will be randomly oriented in bulk homogeneous liquids, but will typically have a nonuniform distribution at the interface due to the asymmetry in forces experienced by the molecule there. Because of the cylindrical symmetry of the planar interface, only the angle between a molecular axis and the interface normal is typically of interest. However, because three linearly independent vectors are generally needed to fully determine the orientation of a rigid body, a complete description of surface molecular orientation involves determining the joint probability that a molecule (whose center of mass is at z) will have its three vectors at angles α , β , and γ with respect to the interface normal. For example, in the case of water molecular orientation, only two vectors are needed for a complete specification, that is, the water molecular dipole (the vector in the molecule plane, bisecting the HOH angle) and one of the OH bonds. Most reports of water orientation at interfaces provide the orientational profile $P(\alpha, z)$, which gives the probability that the water dipole or the water OH bond (or the HH vector) forms an angle α with respect to the interface normal when the molecule is in a slab located at z . Besides this two-dimensional probability distribution, it is also useful to show the orientational order parameter profile, defined as:

$$S(z) = (3\langle \cos^2 \alpha \rangle - 1)/2 \quad [23]$$

where the angular brackets denote the equilibrium average over all the molecules in the slab located at z . $S = 0$ corresponds to an isotropic orientation, while values of $S = +1$ and -0.5 correspond to orientations that are perpendicular ($\alpha = 90^\circ$) and parallel ($\alpha = 0$) to the interface normal, respectively.

The orientational profiles of water and other liquids at interfaces have been reported in many simulation studies.^{93,125,132,135,138,140,142,143,151,174–179}

It is interesting to note that the orientational profiles of the water dipole at the water liquid/vapor interface and at the interface between water and a non-polar liquid all exhibit similar behavior: The water dipole tends to lie parallel to the interface (possibly with a slight tilt toward the bulk) but with a broad distribution. At this orientation, the water molecule is able to maximize its ability to hydrogen bond with other water molecules. The orientation becomes fully isotropic in the bulk at distances that are 1 nm or less from the Gibbs surface. More refined orientational profiles without the capillary wave broadening can be obtained with respect to the intrinsic surface. These intrinsic orientational profiles can better identify the orientational ordering at the interface.^{140,142,143,151,176,177,179} Complementary (and sometimes consistent) experimental information has been provided in recent years mainly by nonlinear spectroscopic methods (second harmonic and sum frequency generation), discussed below.^{19,167–173}

While the profiles of a single orientational variable can be useful, Jedlovsky et al.,¹⁷⁵ point out that care must be exercised in using them to draw conclusions about the complete orientational structure; a bivariate distribution (represented, e.g., by two-dimensional maps) calculated in successive slabs may be necessary.^{142,143,151,175–177,179} In particular, the independent profiles of a single variable cannot be used to reconstruct the full joint distribution.¹⁷⁵

Pair Distributions

Unlike density and orientational profiles that describe the distribution of single particle properties in space (albeit influenced by interactions with other particles), pair distributions or pair densities describe the mutual correlation between two particles. Specifically, the pair distribution function $\rho^{(2)}(\mathbf{r}_1, \mathbf{r}_2)$ is proportional to the probability of simultaneously finding two particles at locations \mathbf{r}_1 and \mathbf{r}_2 . In a bulk homogeneous liquid (of density ρ_L), $\rho^{(2)}(\mathbf{r}_1, \mathbf{r}_2)$ is a function of the distance $r = |\mathbf{r}_2 - \mathbf{r}_1|$ alone, because of translational and rotational symmetry. The mutual correlation of two particles is then described more conveniently in terms of the *radial distribution function* $g(r)$, such that $4\pi r^2 g(r) \rho_L dr$ is the number of particles in a spherical shell of thickness dr and radius r centered on a given particle. At a flat liquid interface, the spherical symmetry is replaced by a cylindrical symmetry, and the pair distribution becomes a function of the distance r between the two particles as well as their locations z_1 and z_2 along the interface normal. Equivalently, one can use (in addition to r) the location z of the given particle and the angle θ between the interface normal and the vector $\mathbf{r}_2 - \mathbf{r}_1$.

Statistical mechanical approaches to the structure of the neat interface generally employ some approximations of the pair distribution function to develop a theory of density profile or surface tension. An example of such an approximation⁵⁵ is using the pair distribution of the homogeneous liquid at the density appropriate to the location z . For a direct calculation of $\rho^{(2)}(r, z, \theta)$, one

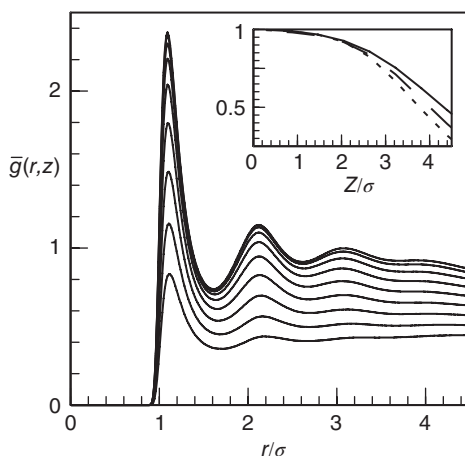


Figure 5 The orientationally averaged $\bar{g}(r, z)$ radial distribution functions for the liquid/vapor interface of a Lennard-Jones fluid at $T^* = 1.0$. The different lines correspond to 0.58σ -thick slabs parallel to the interface. The insert shows the height of the first peak of $\bar{g}(r, z)$ relative to the height in bulk liquid. (Adapted with permission from Ref. 384.)

typically must resort to simulations. Instead of attempting to compute the full 3-dimensional dependency of this distribution function, however, a more practical approach for gaining insights into the particles' mutual correlations at the interface has been to compute the orientationally averaged $g(r)$ within a slab of some thickness parallel to the interface. Thus, while the bulk $g(r)$ is computed by binning all the pair distances, we can obtain an average $\bar{g}(r, z) = g(r, z, \theta)$ at the interface by binning the pair distances when one particle is located inside a narrow slab centered at z . Figure 5 shows the $\bar{g}(r, z)$ for a Lennard-Jones liquid/vapor interface at $T^* = 1.0$. The different lines correspond to 0.58σ -thick slabs parallel to the interface. $z = 0$ is the middle of the bulk region, and $z = 4\sigma$ is the location of the Gibbs surface. As the surface is approached, a monotonic decrease in the value of $\bar{g}(r, z)$ is found at each value of r but with no appreciable change in the *location* of the maxima (around 1.1σ). Because approximately half of the configuration space at the Gibbs surface has a near zero density (vapor) as $r \rightarrow \infty$, $\bar{g}(r, z_G)$ approaches 0.5 rather than the bulk value of 1. The insert shows how the height of the first peak is scaled down relative to the bulk for three temperatures. The significant reduction in the first peak without a significant change in its position has been demonstrated to some degree for water when a nonpolar solute is near the Gibbs surface.^{135,142,143} This reduction reflects the diminished density of the solvent. If one normalizes the local $g(r)$ by the local density¹³⁵ (using the density profile), any observed variation in $\bar{g}(r, z)$ as a function of z reflects the intrinsic change in solvation structure. This concept will be useful when examining solute–solvent correlations below.

Hydrogen Bonding

An example of a pair distribution of particular importance is one that deals with hydrogen bonding and specifically hydrogen bonds involving water at interfaces. This topic has been the subject of numerous investigations using MD and MC methods. A discussion of hydrogen bonding requires its definition, and several such definitions have been proposed. The most popular are based on energy^{180–182} or geometric^{183–185} criteria. For example, two water molecules are considered hydrogen bonded when (a) their mutual interaction energy is more negative than -10 kJ/mol or (b) when the O–O distance is less than 3.5 Å (the location of the first minimum of the bulk water oxygen–oxygen radial distribution function) with the OHO angle deviating by no more than 30° from linearity. A systematic approach for developing H-bond criteria using a geometric cutoff on the basis of a two-dimensional potential of mean force has been described by Kumar et al.¹⁸⁶ Although these definitions are somewhat arbitrary, the exact choice used does not seem to have much impact on the conclusions discussed below.¹⁸⁷ Regardless which definition is used in the simulation of bulk water, it is found that each water molecule is hydrogen bonded by an average of $N_{\text{HB}} \approx 3.5$ hydrogen bonds to other water molecules. Given that the coordination number of water in the bulk is about $N_{\text{C}} = 4$, this shows that the probability for any given hydrogen bond to exist is about $P_{\text{HB}} = N_{\text{HB}}/N_{\text{C}} \approx 0.87$. At the interface, the number of hydrogen bonds per water molecule decreases. For example, at the water/nitrobenzene interface¹³⁸ it is an average of about 2.5 for water molecules near the Gibbs surface. However, at the same time, the coordination number also decreases, in this case to a value of about 2.4 . Thus, the probability that any of the water molecules in the first coordination shell is hydrogen bonded is a higher value (0.96) at the interface than in the bulk. The same qualitative picture emerges in several water interfacial systems.^{135,136,138,141} It is interesting to note that when the hydrogen bond statistic is computed relative to the intrinsic interface,¹⁴⁰ P_{HB} exhibits a maximum, since there is a significant drop in the coordination number for the interfacial molecules in the outermost layer. The result that on average $P_{\text{HB}}(\text{interface}) > P_{\text{HB}}(\text{bulk})$ is consistent with a less mobile interfacial hydrogen-bonding network at the interface. This can be demonstrated more directly by computing the hydrogen bond lifetime (for more details, see below).

While experimental data about water structure and the hydrogen-bonding environment can be obtained with a variety of techniques (X-ray and neutron diffraction, IR and Raman spectroscopy, and X-ray absorption and emission spectroscopy), experimental data about hydrogen bonding at interfaces is becoming available through the application of SFG spectroscopy. This technique provides information about the vibrational spectra of interfacial molecules, which are influenced strongly by the number, strength, and type of hydrogen bonds, as described in the next section.

The Vibrational Spectrum of Water at Interfaces

A single water molecule has IR- and Raman-active symmetric and antisymmetric OH stretch fundamentals at 3657 and 3756 cm⁻¹, respectively. The bulk liquid IR spectra are broad (full width at half maximum \approx 375 cm⁻¹) and redshifted significantly (peak at 3400 cm⁻¹). The bulk spectrum is typically interpreted by deconvoluting it into overlapping Gaussians representing different classes of water molecules experiencing different local H-bond environments. See Refs. 188 and 189 for two recent examples containing many references to earlier work. However, as can be gleaned from reading these references and considering other issues such as temperature dependence,¹⁹⁰ the interpretation of these spectra has been controversial.

At the liquid/vapor interface, as well as at hydrophobic liquid/water interfaces, the “top” water molecules (farthest away from the bulk) are hydrogen bonded to one or two other water molecules. This is evident from the hydrogen-bonding discussion in the previous section and from the result of water OH bond orientations at interfaces, and it suggests that a significant fraction of interfacial water molecules will have one of their OH bonds “free.” This uncoupled stretching mode will appear in the spectra as a sharp peak shifted to frequencies near the gas phase fundamentals. A direct experimental demonstration of the existence of the “free” OH bond at the water liquid/vapor interface was provided first by Shen and coworkers using SFG spectroscopy.^{191,192} Since then, it has been demonstrated for several other water surfaces, for example, at the water/CCl₄ interface by Richmond and coworkers.¹⁹³

In SFG spectroscopy, a visible, linearly polarized laser beam (with a fixed frequency ω_{VIS} and polarization direction \mathbf{j}) and a linearly polarized IR laser beam (direction \mathbf{k} and variable frequency ω_{IR}) are focused at the interface. An output beam with the sum frequency $\omega_{\text{VIS}} + \omega_{\text{IR}}$ and polarization direction \mathbf{i} is generated from the interface but not from the bulk, because of symmetry-based selection rules.¹³ The output light intensity is proportional to the square of the medium second-order nonlinear susceptibility χ_{ijk} . To a good approximation,

$$\chi_{ijk}(\omega_{\text{VIS}}, \omega_{\text{IR}}) \approx \chi_{ijk}^{\text{R}}(\omega_{\text{IR}}) + \chi_{ijk}^{\text{NR}}(\omega_{\text{VIS}}) \quad [24]$$

where the two terms on the right-hand side correspond to resonant (R) and nonresonant (NR) parts. As the IR laser frequency is varied, the output signal is enhanced when a symmetry-allowed molecular vibration is in resonance with the IR laser frequency. Since the first application by Shen, the technique has been applied to many molecular systems and reviewed extensively.^{16,18,28,194–197} Increased sensitivity has been achieved in recent years by employing broad-band heterodyne-detected sum frequency generation (HD-SFG). Here, the signal intensity decreases linearly (vs quadratically in the older SFG method) with decreasing surface coverage, thus improving the detection limit. An additional improvement is provided by the ability of measuring the phase of the HD-SFG signal. This helps remove the nonresonant

background (a problem with the older method).¹⁹⁴ HD-SFG was recently applied¹⁹⁸ to the air/deuterated water interface and revealed that the donor hydrogen bond of the water molecule straddling the interface is only slightly weaker than bulk phase water hydrogen bonds. This suggests an extremely thin interface region, a rare confirmation of two decades of computer simulation results.

Depending on the importance of quantum effects, nonlinear coupling, and dynamical contributions, many methods with varying degrees of sophistication employing fully quantum, semiclassical, and fully classical approaches have been developed for the MD calculation of vibrational spectra of condensed phase molecules. Especially challenging is the problem of calculating the IR and Raman spectrum of bulk water, because this system includes high-frequency coupled anharmonic oscillators, where dynamics and quantum effects are important. Detailed coverage of this important subject is outside the scope of this chapter, and the interested reader can consult a recent review article.¹⁹⁹

Some of the methods developed for bulk liquids have also been used to calculate the hypothetical IR spectra of water at interfaces. Those studies are consistent with the experimental observation of dangling interfacial OH bonds.^{200–202} However, to compare directly with SFG experiments, several groups developed simulation techniques for computing the SFG spectrum. The work in this area is an excellent demonstration of the benefit of combining experiments and simulations to gain insight into the microscopic structure of water at interfaces. In particular, theory has been able to demonstrate the degree to which the spectrum is surface specific and to attribute specific features in the spectra to specific molecular structures.^{178,203}

The computational approaches up to 2006 were reviewed by Perry et al.²⁰⁴ Briefly, these methods are based on representing the SFG spectrum by the Fourier transform of a polarizability–dipole quantum time correlation function (QTCF). A fully classical approach to computing the SFG spectrum is then obtained by replacing the QTCF by a classical expression including a harmonic correction factor:

$$\chi_{ijk}^R(\omega) \propto \frac{i}{\hbar} Q_H(\omega) \int_0^\infty e^{i\omega t} \langle \alpha_{ij}(t) \mu_k(0) \rangle dt \quad [25]$$

where $Q_H(\omega) = 1 - e^{-\hbar\omega/kT}$ is a slowly varying function of ω that represents an approximate quantum correction,²⁰⁴ α_{ij} is the ij component of the molecular polarizability tensor, and μ_k is the component of the electric dipole moment in the k direction. The classical model uses flexible molecules with terms describing the dependence of the molecules' dipole and polarizability on their internal coordinates. This approach was used by Morita and Hynes to calculate the SFG spectrum of the water liquid/vapor interface and is in reasonable agreement with experiments.^{205,206} Improvements on the original approach and additional applications are discussed in Ref. 204.

The main problem with the fully classical approach is that the energy of the $0 \rightarrow 1$ transition of the OH stretching vibration is significantly larger than kT and corresponds to a region of the potential energy not sampled in classical trajectories. One way to handle this problem is to use a mixed quantum/classical treatment, focusing on a single vibrational mode that is treated quantum mechanically, while the liquid molecules are treated classically. This worked well, for example, in the case of a dilute HOD in liquid D_2O . Using this approach requires information about the dependence of the OH frequency, transition dipoles, and transition polarizability on the instantaneous local environment. Skinner and coworkers used this approach (which was originally developed for computing the bulk IR and Raman spectra) to calculate the real and imaginary parts of the resonant susceptibility.²⁰⁷ Good agreement with experiments was found. They were able to show that the SFG spectrum is dominated by single-donor molecules with a total of two or three hydrogen bonds. More recently, they also used this approach to interpret phase-sensitive vibrational sum-frequency experiments of the surface consisting of mixtures of HOD and D_2O .^{77,208,209} They found that good agreement with experiments (specifically, the imaginary part of the sum-frequency susceptibility) required using a three-body potential for water. Interesting conclusions from this work include the lack of evidence for any special ice-like ordering at the surface of liquid water, and the spectrum can be interpreted as arising from overlapping and canceling positive and negative contributions from molecules in different hydrogen-bonding environments.

We note that in the (inhomogeneous) limit of slow frequency fluctuations, the expression used by Skinner and coworkers is reduced²⁰⁷ to the one used earlier by a number of researchers to calculate SFG line shapes.^{178,210}

Dynamics

The atoms or molecules forming a liquid phase are at constant translational and rotational motion. (We discuss vibrational dynamics later.) These dynamics can be characterized by transport properties and time correlation functions. Significant advances in describing equilibrium dynamics in bulk liquids have been made and applied slowly in recent years to characterizing molecular dynamics at liquid interfaces. We expect the reduced density and the anisotropic forces to have significant effects on the dynamics as in the case of molecular structure. The work to date has been focused mainly on using MD simulations to compute diffusion constants, rotational correlation functions, and hydrogen bond lifetimes. We again limit the scope of the discussion to processes that take place at liquid/vapor and liquid/liquid interfaces and refer the reader to a recent review that focuses on dynamics near solid surfaces and in confined geometries.²¹¹

Diffusion at the Interface of Neat Liquids

On a timescale longer than a few molecular collisions (tens of femtoseconds), the translational dynamics in most liquids follow a simple diffusion law. This can be characterized in bulk homogeneous liquids by a diffusion coefficient D that can be obtained easily by computing the equilibrium mean square displacement (MSD) time correlation function:

$$\langle R^2(t) \rangle = \langle [\mathbf{r}(t) - \mathbf{r}(0)]^2 \rangle = \frac{1}{N} \frac{1}{T} \sum_{\tau=0}^{T-1} \sum_{i=1}^N [\mathbf{r}_i(t + \tau) - \mathbf{r}_i(\tau)]^2 \quad [26]$$

where $\mathbf{r}_i(t)$ is the vector position of particle i at time t , and the sum is over all N particles and over all T time origins. Statistical mechanical arguments show²¹² that for time $t > \tau_{\text{mol}}$, $\langle R^2(t) \rangle = 6Dt$, where τ_{mol} is on the order of a few molecular collision times (or more accurately, it is the time it takes for the velocity autocorrelation function to decay to zero). A plot of $\langle R^2(t) \rangle$ versus time shows that at very early times $\langle R^2(t) \rangle \propto t^2$ (inertial motion regime), but at longer times a straight line is obtained with a slope of $6D$.

At an interface, the dynamic parallel and perpendicular to the interface may differ, and both may depend on the distance along the interface normal. The single bulk diffusion coefficient must be replaced by diffusion coefficients in the direction normal (D_{zz}) and parallel ($D_{xx} = D_{yy}$) to the interface: and these (one may naïvely assume) can be calculated from expressions similar to those in Eq. 26:

$$\begin{aligned} \langle [z(t) - z(0)]^2 \rangle &\approx 2D_{zz}t \\ \langle [s(t) - s(0)]^2 \rangle &\approx 4D_{xx}t = 4D_{yy}t \end{aligned} \quad [27]$$

where $\mathbf{s} = (x, y)$ is the component of the vector position in the plane parallel to the interface. D_{zz} and $D_{yy} = D_{xx}$ depend on z , but we expect both to become equal to the bulk diffusion coefficient D when z is far from the Gibbs surface (or from the solid surface in the case of liquid/solid interfaces). The relations in Eq. [27] have been used to estimate the diffusion coefficient at different liquid/vapor and liquid/liquid interfaces with sometimes conflicting results.

The problem with the naïve application of Eq. [27] (especially for computing D_{zz}) is that as an interfacial molecule moves, it changes its z location. For example, the typical time required for a Lennard-Jones atom to traverse a molecular diameter is similar to its surface residence time.²¹³ Thus, the validity of using the asymptotic behavior of the parallel and perpendicular MSDs breaks down and, in particular, $\langle [z(t) - z(0)]^2 \rangle$ reaches a plateau.^{214–216} Berne and coworkers proposed a method to overcome this problem.²¹⁷ The diffusion coefficient parallel to the interface is determined from the MSD and from the (time-dependent) probability that a molecule remains in the slab centered at z . The diffusion coefficient perpendicular to the interface (D_{zz}) is determined by

finding the value of the friction coefficient ζ that gives the best match of the survival probabilities in each slab calculated by MD and by solving the Langevin equation. The diffusion coefficient is then determined from the Stokes Einstein relation $D_{zz} = k_B T / \zeta$ as a function of distance of the layers from the interface. Calculating the diffusion coefficient of water as a function of distance from the liquid vapor interface shows²¹⁷ that, as expected, the diffusion is found to be isotropic far from the interface, and the diffusion coefficient has the value $D = 0.22 \text{ \AA}^2/\text{ps}$, in agreement with what is found from independent bulk simulations. The diffusion at the interface is anisotropic and faster, with values of $D_{xx} = D_{yy} = 0.8 \text{ \AA}^2/\text{ps}$ and $D_{zz} = 0.5 \text{ \AA}^2/\text{ps}$. This reflects the fact that with fewer hydrogen bonds per molecule at the interface, the barrier to diffusion is smaller in either parallel or perpendicular directions.

An approach was reported by Duque et al.²¹³ for calculating the diffusion coefficient perpendicular to the interface. It takes into account the finite residence time (by employing a solution to a stochastic differential equation), but avoids using slabs and considers the molecule positions relative to the intrinsic surface. The main conclusion of their study is that, even if a diffusion coefficient can still be computed, the turnover processes by which molecules enter and leave the intrinsic surface are as important as diffusion itself.

A detailed study of water translational dynamics at the water/hydrocarbon interface was carried out by Chowdhary and Ladanyi.²¹⁸ The dynamics were probed in the usual laboratory frame as well as the intrinsic frame to provide insight about the effect of capillary waves on the dynamics. The distribution of residence times was fitted by stretched exponentials. The diffusion constant parallel to the interface was determined as above. In agreement with other studies, they found diffusion to be faster at the interface than in the bulk and also faster when viewed in the intrinsic frame.

Reorientation Dynamics

A useful and common way of describing the reorientation dynamics of molecules in the condensed phase is to use single molecule reorientation correlation functions.^{219,220} These will be described later when we discuss solute molecular reorientational dynamics. Indirect experimental probes of the reorientation dynamics of molecules in neat bulk liquids include techniques such as IR, Raman, and NMR spectroscopy.²²⁰ More direct probes involve a variety of time-resolved methods such as dielectric relaxation, time-resolved absorption and emission spectroscopy, and the optical Kerr effect.²²¹ The basic idea of time-resolved spectroscopic techniques is that a short polarized laser pulse removes a subset of molecular orientations from the equilibrium orientational distribution. The relaxation of the perturbed distribution is monitored by the absorption of a second time-delayed pulse or by the time-dependent change in the fluorescence depolarization.

All these methods are not surface specific and generally cannot be used to study the reorientation dynamics at liquid interfaces. Although the effect

of orientational dynamics on the SFG line shape was discussed sometime ago,^{222,223} using direct experimental probes of reorientation dynamics of interfacial molecules has gained significant momentum only recently by utilizing time-resolved SFG and SHG spectroscopy.^{224–227} The basic idea is similar to the pump-probe studies in bulk liquids, except that one probes the SFG signal emitted specifically by the surface molecules. For example, Bonn and coworkers have shown that recovery of the SFG signal following vibrational excitation with linearly polarized light can be used to extract the timescale of surface molecular reorientational diffusive motion.²²⁵ They found that the reorientation of interfacial water occurs on the subpicosecond timescale, which is several times faster than in the bulk. This behavior is consistent with fewer hydrogen bonds at the interface. Molecular dynamics simulations of interfacial water dynamics are in quantitative agreement with experimental observations and show that, unlike in bulk where the dynamics can be mostly described as random jumps, the interfacial reorientation is largely diffusive in character.²²⁷

The first molecular dynamics computation of single molecule orientational correlation functions at liquid interfaces was reported by Benjamin.²²⁸ In bulk water, the water dipole correlation time (4 ± 0.2 ps) and the water HH vector correlation time (1.5 ± 0.1 ps, which can be approximately deduced from the NMR line shape) are in reasonable agreement with experiments. The reorientation was found to be faster at the water liquid/vapor interface. The reorientation dynamics of water molecules at the water/1,2-dichloroethane interface is, in contrast, slightly slower (to 6 ± 0.3 and 2.3 ± 0.2 ps for the dipole and the HH vectors, respectively).¹³⁵ Similar results were found in a recent study by Chowdhary and Ladanyi of water reorientation near hydrocarbon liquids having different structure (different branching).²¹⁸ The slower reorientation was limited to water molecules immediately next to the organic phase. Slower dynamics were observed when the reorientation was calculated in the intrinsic frame (thus eliminating the effect of capillary fluctuations).

It is interesting to note that recent simulations²²⁹ show the reorientation dynamics of water next to surfaces of varying polarity to exhibit a nonmonotonic behavior, with slower dynamics observed next to both highly polar and highly nonpolar surfaces and faster dynamics next to a surface of intermediate polarity. Insight into this behavior as well as into the mechanism governing the reorientation was provided recently by MD simulations and analytic modeling.^{230,231} Two competing factors – hydration structure, which controls the number of “free” OH bonds and surface binding energy – explain the nonmonotonic reorientation dynamics. The dynamics can be explained using the extended jump model of Lagge and Hynes, where a relatively large jump in the orientation is followed by a slow diffusion of the O–O vector of two hydrogen-bonded molecules.²³²

Hydrogen Bond Dynamics

The reorientation and translational dynamics of water molecules is closely related to the dynamics of making and breaking hydrogen bonds, because translations and rotations are responsible for bringing two water molecules to the distance and orientation necessary for forming the bond. This topic has been discussed extensively experimentally^{233–239} and theoretically^{185–187,240–247} in bulk water and in aqueous solutions. It is important for understanding spectroscopy, reactivity, and the behavior of hydrated solute molecules. With the advent of time-resolved SFG spectroscopy, there has been some interest in understanding the hydrogen-bonding dynamics at aqueous interfaces.^{230,248–257}

Hydrogen bond dynamics can be studied theoretically using the time correlation function approach originally developed for calculating reaction rate.²⁵⁸ Using any of the definitions of a hydrogen bond described earlier, a dynamical random variable h is then defined this way: Consider two *tagged* water molecules that are hydrogen bonded at $t = 0$. $h(t)$ is equal to 1 if these two molecules are still bonded at a later time t ; otherwise it is equal to zero. Other definitions are possible. For example, one can ignore the past history of $h(t)$ (so $h(t)$ may become 1 again later if *these* two water molecules reform their bond), or one may ignore a short time interval where the bond is broken and immediately reforms. The reader should consult Refs. 187, 240, and 241 for more details.

A normalized equilibrium autocorrelation function $c(t)$ is defined using the random variable h :

$$c(t) = \frac{\langle h(0)h(t) \rangle}{\langle h(0)h(0) \rangle} \quad [28]$$

where the ensemble average is over all pairs and all time origins. (Note that $\langle h(0)h(0) \rangle = \langle h \rangle$, as $h^2 = h$.) The function $c(t)$ gives the probability that a given hydrogen bond exists at time t , provided it existed at time zero. Clearly, $c(t)$ starts at 1 and decays to zero with a time constant τ_{rx} , where $c(\tau_{\text{rx}}) = 1/e$. This decay involves the breakup of a hydrogen bond due to the mutual diffusion and reorientation of a pair of initially hydrogen-bonded water molecules. A detailed analysis can provide information about the intrinsic forward (k_f) and backward (k_b) rate constants for breaking a hydrogen bond and thus the lifetime $\tau = 1/k_f$ of a hydrogen bond.^{187,240,241} The function $c(t)$ is also useful for a qualitative account of the lifetime.

To examine hydrogen bond dynamics as a function of its location normal to the interface, the simulation box can be divided into slabs. $c_n(t)$ is computed for the n th slab by including the contributions of all the hydrogen bonds between pairs of water molecules, where at least one of the molecules belongs to the given slab. If a water molecule changes its initial slab during the simulation, its time history then contributes to the average in the new slab.

A hydrogen bond's lifetime is found to be longer at the water/metal²⁵¹ and water/protein^{248–250,255} interfaces than in bulk water. Berne and coworkers

examined the hydrogen bond dynamics at the water liquid/vapor interface.²⁵² They found faster hydrogen bond dynamics at the interface than in bulk water for the polarizable water models, but slower dynamics if nonpolarizable models are used. Even with the polarizable models, however, the shorter lifetime at the interface was attributed to more rapid translational diffusion at the interface rather than to faster kinetics of hydrogen bond formation. This can be demonstrated by removing the contribution of the relative diffusion of water molecules by defining a new correlation function:

$$c_{\text{nd}}(t) = \frac{\langle b(0)b(t)H(t) \rangle}{\langle b(0)H(t) \rangle} \quad [29]$$

where $H(t) = 1$ if the O–O distance is less than the hydrogen bond defining distance of 3.5 Å (but for any orientation), and using the relation $b(0)b(0) = b(0)$. $c_{\text{nd}}(t)$ is the conditional probability that a hydrogen bond exists at time t given that it existed at $t = 0$ and that the two water molecules have not diffused away from one another. The relaxation of this correlation function is slower at the interface than in the bulk. This is explained by the fact that the number of water molecules next to a hydrogen-bonded pair that are available to accept or donate a hydrogen bond is smaller at the interface than in the bulk.

The hydrogen bond dynamics at the interface between water and a series of organic liquids of varying polarity and surface structure were examined by Benjamin.²⁵³ The hydrogen bond population relaxation time was found to be slower than in bulk water and strongly dependent on the nature of the organic phase. Profiling the lifetime shows dependence of the lifetime on the location of the water molecules along the interface normal, with the bulk relaxation rate reached at approximately two layers “below” the Gibbs surface. The slowest relaxation was found at the interface that is characterized by the tendency to form the most water protrusions. This is due to the lack of adjacent but non-hydrogen-bonded molecules, which increases the timescale for a water molecule to reorient itself toward a new hydrogen-bonding “partner.”

Chowdhary and Ladanyi investigated how the chain length and branching of liquid alkanes influence the dynamics of hydrogen bonds in water next to these liquids.²⁵⁶ They found that the hydrogen bond dynamics of interfacial water are weakly influenced by the identity of the hydrocarbon phase and by capillary waves. However, they found that hydrogen bond dynamics are sensitive to the initial orientation of the molecules participating in the hydrogen bond.

SOLUTES AT INTERFACES: STRUCTURE AND THERMODYNAMICS

As with neat liquids at interfaces, the molecular structure of solvated molecules at an interface can be discussed using probability distribution functions.⁵⁵ We

focus here on the single particle distribution (or solute density profile) and the pair distribution, because they have received much attention. We also remark briefly on the subject of solute orientational profiles.

Solute Density

Basic Definitions and the Gibbs Adsorption Equation

The single particle distribution function $\rho^{(1)}(\mathbf{r}_s)$ gives the probability density of finding the center of mass of a solute molecule at the location \mathbf{r}_s . In bulk homogeneous solutions, $\rho^{(1)}(\mathbf{r}_s) = \rho_b = \text{constant}$, but at a planar liquid/vapor or liquid/liquid interface $\rho^{(1)}(\mathbf{r}_s)$ depends on the solute location along the interface normal z_s . For simplicity of notation we will denote it by $\rho_s(z)$. Computationally, one counts the number of solute molecules per unit volume in a thin slab centered at z to obtain the density distribution $\rho_s(z)$. The integral of $\rho_s(z)$ along z gives the total number of solute molecules per unit area, and in general this is not equal to the integral of the constant density ρ_b over the same interval (which includes the interface region). The difference is called the surface excess density Γ , which is related to the surface tension of the solution γ and the solute chemical potential μ using the Gibbs adsorption equation:⁵⁵

$$d\gamma = -\Gamma d\mu \quad (\text{fixed temperature}) \quad [30]$$

If there are c components, the left-hand side is generalized to $d\gamma = -\sum_{i=1}^c \Gamma_i d\mu_i$.

The surface excess density Γ can be measured easily. It is typically done as a function of the bulk solute concentration ρ_b to obtain the so-called *adsorption isotherm*.¹¹ If $\Gamma > 0$, the solute is considered surface-active, and according to Eq. [30] this is associated with a decrease in the surface tension relative to pure solvent(s).

A direct simulation of a solute's density profile is feasible for relatively concentrated solutions. For example, a 1 M aqueous solution containing 100 solute molecules (so that reasonable statistical accuracy can be achieved) must include approximately 5500 water molecules. Such simulations were reported for neutral^{259,260} as well as ionic solutions, with the goal of elucidating the structure of the interface as well as establishing the ability of the simulation methodologies to reproduce the relationship between surface tension and surface excess. Of particular recent interest has been the study of ionic distributions at the water liquid/vapor interface because of its relevance to the heterogeneous photochemistry of sea salt aerosols, a system implicated in ozone depletion. These types of simulations were the first to indicate the presence of ions at the top-most layer of aqueous solutions,^{261–269} followed by a number of possible experimental confirmations.^{264,265,270,271} A molecular dynamics study of the SFG spectra of ionic solutions shows, in agreement with experiments, that adding sodium iodide to water leads to an increase in

SFG intensity in the spectral region that is associated with an increase in the ordering of hydrogen-bonded water molecules.²⁷² The increase in the SFG intensity was attributed to an increase in the ordering of water molecules caused by the formation of an ionic double layer at the interface.

The Potential of Mean Force – Methodology

The solute density profile is related closely to the local free energy or the free energy profile:⁵⁵

$$A(z) = -RT \ln \rho_s(z) \quad [31]$$

where R is the gas constant (8.314 J/mol/K), and T is the temperature. $A(z)$ is also sometimes called the Potential of Mean Force (PMF), because it represents the canonical ensemble average of the effective potential experienced by the solute. $A(z) - A(z_{\text{bulk}})$ is the free energy change associated with moving the solute from the bulk to the location z . If the solute is surface active, $A(z)$ will typically have a minimum at some interface location z_{int} , and $\Delta A_{\text{ads}} = A(z_{\text{int}}) - A(z_{\text{bulk}})$ is the solute adsorption free energy (negative). It can be obtained from the experimentally determined adsorption isotherm.¹¹

Unlike the adsorption isotherm, the experimental determination of $\rho_s(z)$ is much more difficult, and only recently have X-ray reflectivity measurements been used as the first experimental technique to measure ions' density profiles directly at the water–organic liquid interface.^{273,274} Thus, most of our knowledge of $\rho_s(z)$ and $A(z)$ has been obtained from computer simulations.

If solute–solute interactions can be neglected, $\rho_s(z)$ can be calculated by a canonical ensemble average of a system that includes a single solute molecule:

$$\rho_s(z) = \langle \delta(z - z_{\text{cm}}) \rangle = \frac{\int e^{-\beta H} \delta(z - z_{\text{cm}}) d\mathbf{r}}{\int e^{-\beta H} d\mathbf{r}} \quad [32]$$

where z_{cm} is the center of mass of the solute along the interface normal calculated relative to the system's center of mass. If, in a given interval, $A(z)$ varies significantly (more than several RT s), calculating the ensemble average in Eq. [32] by a direct sampling of z_{cm} is not feasible, and well-known “tricks” for simulating rare events must be employed. In the “windowing” (also called “umbrella sampling”) method,^{61,212,275} the interval of interest is divided into a series of n overlapping “windows,” such that within each window a statistically meaningful sampling of z_{cm} can be obtained. A series of $A_i(z)$ segments ($i = 1, 2, \dots, n$) can then be combined by using their overlapping regions^{276,277} to arrive at the final free energy profile for the entire region of interest. The solute is typically restricted to a given window by a window potential (which is zero

when the solute is inside that window but rises rapidly when the solute's center of mass attempts to escape the window).

If $A(z)$ varies rapidly in a given region, the requirement of many overlapping windows becomes computationally inefficient. It is possible to increase the sampling statistics by utilizing a "biasing potential." This is based on the fact that if one adds to the Hamiltonian H in Eq. [32] a term $U(z_{\text{cm}})$, which is a function of z_{cm} alone, the resulting biased distribution is related to the original distribution by:⁶¹

$$\rho_s^{\text{bias}}(z) = e^{-\beta U(z)} \rho_s(z) \quad [33]$$

If U is selected to be a reasonable guess of $-A(z)$, the biased distribution will be nearly flat, and the original distribution can be recovered from this relation. The umbrella sampling method has been applied mainly to chemical reactions (see below) and in some cases to solute adsorption.²⁷⁸

Another approach used to compute the PMF for solute crossing an interface is based directly on the concept of mean potential:^{266,273,279–282} We denote by $f_N(z)$ the normal component of the average total force on the solute's center of mass, when the solute center of mass is fixed at the location z . The series of $f_N(z)$ values computed along a fine grid allows for calculating the integral, which is the negative of the PMF:

$$A(z_2) - A(z_1) = - \int_{z_1}^{z_2} f_N(z) dz \quad [34]$$

Expanding this to the case of a more general coordinate and to the case when this coordinate is unconstrained has been discussed by Darve and Pohorille.²⁷⁹ We point out that calculating the PMF is just one example of free energy calculation methods that have been developed and discussed extensively in the literature. The reader can consult the many excellent sources on general simulation techniques mentioned earlier in this chapter and others,²⁸³ as well as a chapter in this book series dedicated to this topic.²⁸⁴

The Potential of Mean Force – Applications

The methods discussed above have been applied mainly to calculating the potential of mean force for the adsorption of ions at the liquid/vapor interface of water. This was motivated by fundamental questions in atmospheric chemistry and by the problem of ions and other solutes' transfer across the water/organic liquid interface, found in electrochemistry, solvent extraction, and phase transfer catalysis.

The Gibbs adsorption equation and the fact that the surface tension of most inorganic aqueous salt solutions increases with the salt's bulk concentration suggest a negative surface excess for these ions and thus a positive free energy of ion adsorption at the water surface. Continuum electrostatic model calculations give rise to a monotonic increase in the free energy

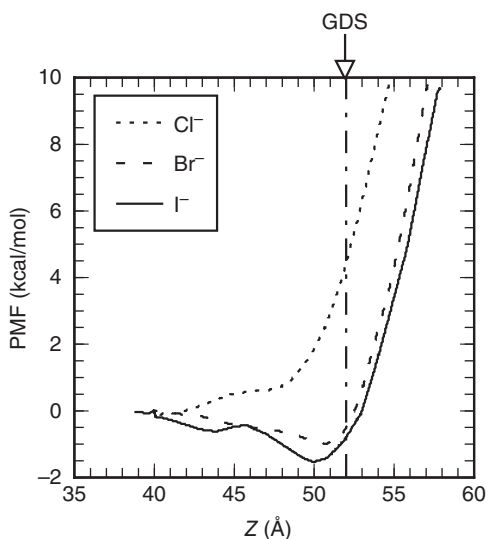


Figure 6 Potential of mean force of several halide ions across the water liquid/vapor interface at $T = 300$ K. GDS is the Gibbs dividing surface. (Reprinted with permission from Ref. 280. Copyright 2002 American Chemical Society.)

profile as an ion approaches the interface from the higher dielectric medium region.^{228,285–289} This effect is known as the image charge repulsion. Early molecular dynamics calculations gave qualitatively similar results for small nonpolarizable ions^{228,285} such as Li^+ , Na^+ , and F^- . Those results have been confirmed in more recent calculations using polarizable ions and water models.^{95,280} Contrary to the simple electrostatic picture, however, molecular dynamics calculations^{261–268,290} and experiments^{264,265,270,271,291,292} suggest a local surface enhancement of larger polarizable anions such as I^- , thiocyanate anion,^{264,265} and dicarboxylate dianions.²⁶² An example is shown in Figure 6. The small local minimum in the iodine ion PMF near the Gibbs surface corresponds to an increase in local concentration. Note that the total surface excess, which includes the depleted sublayer, still gives rise to an overall negative surface excess in agreement with the Gibbs adsorption equation.^{268,290} In addition to the mutual induced polarizabilities of the water and the ions, other entropic and energetic²⁹³ considerations and surface water fluctuations²⁹⁴ have been implicated in the local surface enhancement of ions.

Of particular fundamental and practical interest has been the recent and sometimes conflicting work on the surface behavior of the hydronium and hydroxide ions.^{264,295–301} Experimental and theoretical work has established that the concentration of hydronium cations is enhanced at the water liquid/vapor interface compared with the bulk. Some surface tension measurements as a function of bulk water pH along with electrophoretic and titration measurements of air bubbles or oil droplets in water suggest strong affinity

of hydroxide anions for the water/vapor interface. Surface-selective nonlinear spectroscopies, photoelectron spectroscopy, and molecular simulations, in contrast, show at most a weak surface affinity of hydroxide ions.^{297,298}

PMF calculations of ion and solute transfer across the water/immiscible liquid interface generally show a monotonic change between the two phases.^{273,274,281,282,302–310} The net change in the PMF – $A(\text{bulk liquid}) - A(\text{bulk water}) \approx \Delta G_{\text{transfer}}$ – gives the Gibbs free energy of transfer from the water to the immiscible liquid phase. Results are in qualitative agreement with experimental data and with continuum electrostatic models,^{288,289,305} although in the latter case adjustable parameters (the size of the spherical cavity used to model the ion) were needed to obtain a good fit.³⁰⁵

While most comparisons of the free energy profile between experiments and simulations have been limited to just the net free energy of transfer, X-ray reflectivity measurements can probe the total ionic density across the interface between two immiscible electrolyte solutions and can be used to make a comparison with the full PMF. The PMF of Br^- and tetra butyl ammonium cation (TBA^+) across the water/nitrobenzene interface, calculated by MD, have been used to derive the ionic density distribution. The total distribution was found to agree well with the measured one over a wide range of bulk electrolyte concentration.^{273,274} This contrasts with the predictions of the continuum electrostatic Gouy–Chapman theory, where ionic density distributions vary substantially from the X-ray reflectivity measurements, and this underscores the importance of molecular-scale structure at the interface.

Of course, if one is interested only in the net free energy of transfer, then calculating the full PMF is not necessary. Instead, one may calculate the absolute free energy of solute solvation in the bulk of each solvent and simply take the difference. This, however, ignores the possibility that ions (especially small hydrophilic ones) may retain a partial hydration shell while being transferred into the organic phase. This approach was demonstrated for the free energy of transfer of alkali and halide ions from water to 1,2-dichloroethane (DCE). Free energy calculations of different-size ion-water clusters (different numbers of water molecules) in bulk DCE³¹¹ reproduce the free energy of transfer (ΔG_t) of ions from water to this solvent, in reasonable agreement with the experimental data. We will see below that accounting for the possibility of ions retaining part of their hydration shell is critical for a correct interpretation of several dynamical phenomena as well.

The topic of ion transfer free energy across the liquid/liquid interface is closely related to the problem of ion channels in biological membranes,^{312,313} but this is outside the scope of this chapter.

Solute–Solvent Correlations

The solute–solvent pair correlation function $\rho^{(2)}(\mathbf{r}_s, \mathbf{r}_l)$ gives the probability of finding the solute molecule center of mass at location \mathbf{r}_s , given a solvent

molecule at \mathbf{r}_l . In bulk liquid, $\rho^{(2)}(\mathbf{r}_s, \mathbf{r}_l)$ is a function of only the solvent–solute distance $r = |\mathbf{r}_s - \mathbf{r}_l|$ and is proportional to the solvent solute radial distribution function $g_{sl}(r)$. However, at a planar interface $\rho^{(2)}(\mathbf{r}_s, \mathbf{r}_l)$ is a function of r, z (the solute center of mass location) and the angle θ that the solute–solvent vector $\mathbf{r}_s - \mathbf{r}_l$ forms with the interface normal. Direct information about this quantity has been provided mainly by computer simulations. As was the case for the pair correlations in neat liquid surfaces, one typically computes $g_{sl}(r; z)$ by averaging $g_{sl}(r, z, \theta)$ over θ with the solute center of mass allowed to move in a slab of some small width (a few Å) centered at z .

In Figure 7 we demonstrate an important principle governing ion behavior at aqueous interfaces, namely, that ions are able to keep their hydration shell intact to some degree and that depends on their charge and size.^{228,280,285,290,314,315} This figure shows the orientationally averaged $g_{X-O}(r; z)$ at three locations: in bulk water (solid line), near the Gibbs surface of the water liquid/vapor interface (dashed line), and at a slab whose center is located 3 Å “above” the Gibbs surface (dotted line). The top panels show the results for $X = \text{Li}^+$ (small ion) and $X = \text{I}^-$ (large ion). The small ion is able to keep its hydration shell intact when it is moved to the liquid/vapor interface. The interfacial orientationally averaged $g(r)$ is almost identical to the bulk $g(r)$ for $r < r_{\min}$, where r_{\min} is the location of the first minimum of

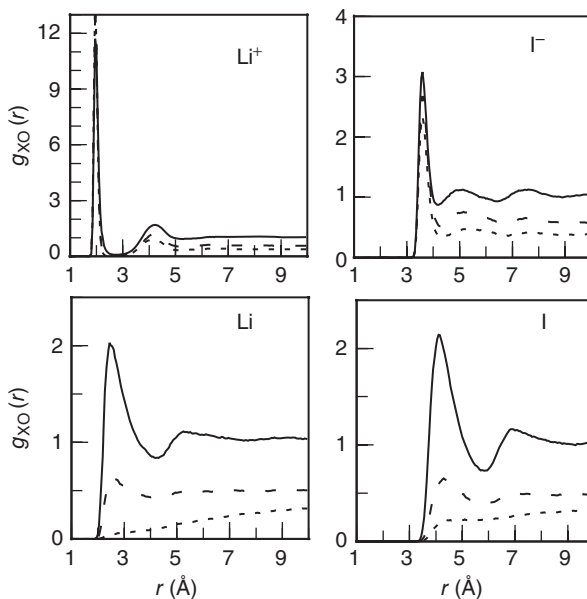


Figure 7 The orientationally averaged g_{X-O} for different charged and uncharged ions at three locations: in bulk water (solid line), near the Gibbs surface of the water liquid/vapor interface (dashed line), and 3 Å “above” the Gibbs surface (dotted line).

$g(r)$, which is the region of the first hydration shell. The ability of the larger ion to do this is significant but somewhat diminished. The bottom panels depict calculations done for fictitious particles identical to Li^+ and I^- in their size, but with no charge. Here, in contrast with the case of charged particles, there is a significant depletion in the number of water molecules in the first hydration shell. Note that in all cases, the second hydration shell is diminished significantly. Note also that the asymptotic value of $g(r)$ reflects the average density of the medium. Another way to demonstrate this effect is to compute the total solvation energy profile of the ion $E(z)$ and the energy of the first hydration shell $E_{1\text{shell}}(z)$, calculated when the ion is in different z locations. While $E(z)$ drops significantly as the ion is moved to the liquid/vapor interface, $E_{1\text{shell}}(z)$ remains essentially constant.

This semi-invariance of the ion's hydration structure manifests itself during ion transfer across the liquid/liquid interface. Depending on its size and charge, the ion is able to drag all or part of its hydration shell as it is transferred from the aqueous to the organic phase.^{281,282,302,306–308,314,316–318} Closely related to this concept is the role played by the fluctuations in the solvent–ion interactions in driving small ions toward and away from the interface.²⁹⁴

The ability of ions to interact with liquid surfaces in this manner has important implications for understanding several aspects of spectroscopy and dynamics involving ionic solutes, to be discussed below.

Solute Molecular Orientation

As in the case of molecular orientation at the interface of neat liquids, solute molecular orientation can provide insight into the local intermolecular interactions at the interface, which, in turn, is useful for interpreting dynamics, spectroscopy, and reactivity. The simple picture that the hydrophilic part of an asymmetric solute molecule tends to point toward the bulk aqueous phase, while the hydrophobic part points toward the opposite direction, has been confirmed in both simulations and experiments. Polarization-dependent SHG and SFG nonlinear spectroscopy can be used to determine relative as well as absolute orientations of solute molecules with significant nonlinear hyperpolarizability.^{16,17,172,173,319,320} The technique is based on the fact that the SFG and the SHG signals coming from an interface depend on the polarization of the two input and one output lasers. Because an interface with a cylindrical symmetry has only four elements of the 27-element second-order susceptibility tensor being nonzero, these elements (which depend on the molecular orientation) can be measured. This enables the determination of different moments of the orientational distribution:

$$\overline{\cos^n \phi} = \int_0^\pi \cos^n \phi P(\phi) \sin \phi d\phi \quad [35]$$

from which one can model $P(\phi)$. These orientational distributions are typically found to be broad, in part due to the capillary broadening of the interface region.

Much more detailed information can be obtained from molecular dynamics and Monte Carlo simulations. This includes the solute orientational profile, which can be expressed using the orientational probability distribution $P(\phi; z)$. If \mathbf{d} is a vector fixed in the molecular frame of a solute molecule, the probability distribution of the angle ϕ between this vector and the normal to the interface is calculated easily using computer simulations as a function of the solute location z . For relatively large dye molecules with a slow reorientation time, convergence can be slow, so it is important to verify that the computed $P(\phi; z)$ is uniform for z values in the bulk region. Only a few molecular dynamics studies have been reported, with results that generally show an orientational preference with broad distributions.^{321–323}

SOLUTES AT INTERFACES: ELECTRONIC SPECTROSCOPY

Experimental and theoretical studies of visible and UV spectra of solute molecules in the condensed phase have a very long history. These techniques provide detailed and rich information about the molecular structure, dynamics, and interactions governing solvation.^{324–334} The development of nonlinear optical spectroscopic techniques¹³ has enabled the study of electronic transitions in solute molecules adsorbed at liquid interfaces, and in this section we focus on some computational aspects of solute electronic spectroscopy at liquid/vapor and liquid/liquid interfaces. We consider here static spectroscopy and postpone the discussion of related dynamic phenomena to the section on solute dynamics at interfaces.

A Brief General Background on Electronic Spectroscopy in the Condensed Phase

For simplicity we focus on transitions between two electronic states of a solute molecule $|a\rangle \rightarrow |b\rangle$, in a dilute solution (so solute–solute interactions and energy transfer are not considered). We can think of the states $|a\rangle$ and $|b\rangle$ as the ground and excited states, respectively, for an absorption spectrum and having the reverse role for discussing the emission spectrum. The solvent–solute interactions will modify the energy of the two states, so the transition energy will change compared with that in the gas phase, $\Delta E_0 = E_0^b - E_0^a$. The relatively sharp transition in the gas phase (with linewidth generated by lifetime and vibrational broadening) acquires an additional width due to fluctuations in the positions of the solvent molecules relative to the solute. Thus, solvent effects on

electronic spectra contain valuable information about solvation structure (and dynamics) and solvent–solute interactions.

Because our focus is on the solvent effects at interfaces, we consider as a simple model a two-level quantum system coupled to a classical bath. In a more realistic system one must include the contributions of intramolecular solute vibration and their coupling to a semiclassical or quantum bath.^{333,334} The classical treatment allows us to obtain the transition energy for a particular solvent configuration by $\Delta E = H_b(\mathbf{r}) - H_a(\mathbf{r})$, where H_a and H_b are the total (solvent + solute) Hamiltonian of the system when the solute is in the $|a\rangle$ and $|b\rangle$ electronic states, respectively. For a weak electromagnetic field, neglecting solvent dynamics and assuming an infinite excited state lifetime, the (area normalized) static line shape is given in the Franck–Condon approximation by the distribution of transition energies in the initial state:

$$I(\omega) = \langle \delta[\omega - \Delta E(\mathbf{r})/\hbar] \rangle_a \quad [36]$$

where δ is the Dirac delta function and $\langle \dots \rangle_a = \frac{\int e^{-\beta H_a} \dots d\mathbf{r}}{\int e^{-\beta H_a} d\mathbf{r}}$ represents the

canonical ensemble average when the system's Hamiltonian is H_a . Eq. [36] is the basis for a classical computer simulation calculation of the line shape: One runs MD or MC simulations with the Hamiltonian H_a and bins the instantaneous energy gap to obtain the spectrum. By replacing the delta function with its Fourier representation,

$$\langle \delta(\omega - x) \rangle = (2\pi)^{-1} \int_{-\infty}^{\infty} e^{-i\omega t} \langle e^{ixt} \rangle dt \quad [37]$$

and using the second-order cumulant expansion of $\langle e^{ixt} \rangle$, it is straightforward to show that these line shapes are Gaussians, with peak positions given by $\omega = \langle \Delta E/\hbar \rangle_a$.^{329,335,336}

$$I(\omega) = \frac{1}{\sqrt{2\pi\sigma^2}} e^{-(\omega - \langle \Delta E/\hbar \rangle_a)^2 / 2\sigma^2}, \quad \hbar^2 \sigma^2 = \langle \Delta E^2 \rangle_a - \langle \Delta E \rangle_a^2 \quad [38]$$

These expressions have been used as the starting point for the development of a number of approximate statistical mechanical and continuum model formulas for the solvent-induced spectral shift. Because a detailed discussion of this topic is outside our scope, we refer the reader to the literature for a few examples of these results.^{81,92,324,329,330,335–341}

However, it is useful for future reference to highlight some results. If the solute is modeled as a point dipole inside a spherical cavity of radius R

and the solvent as a dielectric continuum with a dielectric constant ϵ , the solvent-induced shift in the peak spectrum is then given by

$$\Delta\omega = \frac{4\mu_g(\mu_g - \mu_e)}{R^3} \frac{\epsilon - 1}{\epsilon + 2} \quad [39]$$

where μ_g and μ_e are the solute's electric dipole moments in the ground and excited states, respectively. This formula shows that if the excited state dipole is larger than that of the ground state, the spectrum is redshifted (*positive solvatochromism*), while if $\mu_e < \mu_g$ the spectrum is blueshifted (*negative solvatochromism*). This follows simply from the fact that the state with the larger dipole is stabilized to a greater degree by a polar solvent.

It is well known experimentally that the ability of a solvent to interact differently with the ground and excited states typically involves much more than just its dielectric constant; it may also depend on the details of the solvent–solute interaction and the solvent structure. The solvent *polarity scale* is an empirically based approach to express quantitatively the differential solvation of the ground and excited states of a solute.^{327,342–344} It uses the electronic spectral shift as a convenient one-parameter characterization of the ability of the solvent to interact with the solute. Several solvent polarity scales have been developed on the basis of the spectral shift of several different dye molecules. For example, one of the most widely used scales, called the $E_T(30)$ scale, is equal to the spectral shift in kcal/mol for the $\pi \rightarrow \pi^*$ transition in pyridinium N-phenolate betaine dye. The $E_T(30)$ values, as well as other polarity scales, have been tabulated for many solvents.³³²

It is important to point out that using the polarity scale to quantify the liquid's solvation power works well if the solvent–solute interactions are nonspecific. It will fail if specific interactions, such as hydrogen bonding, play important roles.^{332,344,345} If that happens one can introduce additional parameters to describe these specific interactions. For example, in the Kamlet–Taft empirical approach, one introduces a parameter to describe hydrogen-bond donor acidity (alpha) and another parameter to describe hydrogen bond acceptor basicity (beta).^{342,346,347} The ability of such an approach to describe the hydrogen bonding (or other specific interactions) of the solvent generally depends on finding an indicator molecule that interacts with the solvent primarily through hydrogen bonding (or other specific interactions of interest). For a recent review with extensive references, see Ref. 332.

Experimental Electronic Spectroscopy at Liquid Interfaces

To measure electronic spectra of solute molecules at interfaces, one must overcome the problem that most of the UV and visible signals absorbed or emitted from solute molecules are generated in the bulk. Unless most of the solute molecules are at the interface, which is the case for systems such as adsorbed

monolayers, micelles, and microemulsions,^{348–354} the bulk signal masks the much weaker interface signal. Resonant SHG and Electronic Sum Frequency Generation (ESFG) are ideal techniques for studying surface electronic spectra because, as a second-order nonlinear optical processes, they are dipole forbidden in bulk media. In the SHG technique, a laser beam of frequency ω and intensity $I(\omega)$ (and a specific polarization direction) is focused on the interface. The intensity $I(2\omega)$ of the detected output beam with a frequency 2ω (and a specific polarization direction) is proportional to $I^2(\omega)$ and to the solute surface density squared, and it depends on the squares of the nonzero elements of the second-order susceptibility tensor of the medium $|\chi^{(2)}|^2$ (as well as on the orientation of the incident beam with respect to the surface normal). Each of these elements depends on the solute's molecular hyperpolarizability, and it is resonantly enhanced when $2\omega = \Delta E/\hbar$, giving rise to an effective electronic excitation spectrum. Because a nonresonant term also contributes to the signal, the peak of the *observed* SHG spectrum does not necessarily match the electronic transition energy, so it must be removed by a fitting procedure.³⁵⁵

SHG has been used mainly to measure solute surface concentration, molecular orientations, and relaxation, as mentioned earlier. The application of SHG to electronic spectra at liquid interfaces has been mainly limited to measuring the peak spectrum for insight into the polarity of the interface region.^{23,355–361} By comparing the peak position of the SHG spectrum at the interface with the peak UV absorption spectra of the same dye molecule in the bulk of different solvents, one can place the interface polarity on an established polarity scale. For example, the gas phase intramolecular $\pi \rightarrow \pi^*$ charge transfer band of *N,N'*-diethyl-*p*-nitroaniline (DEPNA) is centered at 329 nm.³⁶² It is redshifted to 429 nm in bulk water³⁵⁵ but to only 359 nm in the nonpolar bulk hexane.³⁴⁶ The positive solvatochromic shift of DEPNA is mainly due to the large increase in the electric dipole moment on excitation (from 5.1 D to 12.9 D). At the air/water interface, the SHG peak is at the intermediate value of 373 nm, which is similar to the peak position in bulk carbon tetrachloride (375 nm) and butyl ether (372 nm).³⁴⁶ This indicates that the water/air interface has a polarity similar to that of these two liquids (at least as it concerns the interaction with DEPNA). A similar polarity of the air/water interface was obtained³⁵⁶ using the $E_T(30)$ polarity indicator (which exhibits negative solvatochromism).

By applying this approach to adsorbed dyes at liquid/liquid interfaces, Eisenthal and coworkers noticed that the polarity of several liquid/liquid interfaces (between water and 1,2-dichloroethane, chlorobenzene, or heptane) is close to the arithmetic average of the polarities of the two bulk phases.³⁵⁶ Because it is known that most of the contribution to solvation energy comes from the first solvent–solute coordination shell, the simple arithmetic rule indicates that DEPNA and the $E_T(30)$ indicator molecules have a mixed solvation environment at the water/liquid interface.

The idea of assigning a specific polarity value to a liquid interface region on the basis of a solvatochromic shift of an adsorbed dye molecule involves several assumptions. Although these assumptions have been found to be violated sometimes, they provide valuable new insights into the structure of and molecular interactions at interfaces. The assumptions typically made include the following:

1. *Dependence of the perceived polarity on the solute probe.* Different probe molecules may interact differently with the interfacial solvent molecules, thus “reporting” different solvation environments. For example, the DEPNA polarity indicator suggests that the air/water interface is less polar than bulk 1,2-dichloroethane (DCE),³⁵⁶ while the SHG spectrum of the doubly charged eosin B dye at the air/water interface and in bulk DCE³⁵⁸ gives the opposite result. Here, despite the loss of some hydration at the interface, the strong field arising from the two charges in eosin B enables it to form a local hydration shell that is more stable than in bulk DCE.

For another example at the liquid/liquid interface, Steel and Walker³⁵⁹ used two different solvatochromic probe molecules, *para*-nitrophenol (PNP) and 2,6-dimethyl-*para*-nitrophenol (dmPNP), to study the polarity of the water–cyclohexane interface. These probes give spectral shifts as a function of bulk solvent polarity that are very similar because both solutes are mainly sensitive to the nonspecific solvent dipolar interactions. However, when these two dye molecules are adsorbed at the water/cyclohexane interface, they experience quite different polarities. The more polar solute (PNP) has a maximum SHG peak that is close to that of bulk water, and thus it reports a high-polarity environment. In contrast, the less polar solute (dmPNP) reports a much lower interface polarity, having a maximum SHG peak close to that of bulk cyclohexane. Clearly, the more polar solute is adsorbed on the water side of the interface, keeping most of its hydration shell, and thus reports a higher polarity than does the nonpolar solute. Other examples of the surface polarity dependence on probe molecules are discussed in Ref. 363.

2. *Dependence on probe location and orientation.* From our discussion of the neat interface we now know that this region is very narrow, and the SHG peak spectrum will likely depend strongly on the solute location and orientation. This was proved by Steel and Walker who designed a series of surfactant solvatochromic probes they call “molecular rulers.”³⁶⁴ Each of these surfactant molecules consists of an anionic hydrophilic sulphate group (which is restricted to the aqueous phase), attached to a hydrophobic solvatochromic probe moiety by a variable length alkyl spacer. The probe is based on *para*-nitroanisole (PNA), whose bulk solution excitation maximum shifts monotonically with solvent polarity.³⁴³ When these surfactant molecules adsorb at the interface, the anionic end is in the aqueous phase, and the probe moiety resides at variable positions relative to the interface,

depending on the length of the alkyl spacer. The SHG spectra of these surfactants were measured at different water/liquid alkane interfaces.^{23,360,361} As the length of the alkyl spacer changes, the polarity “reported” by the PNA probe varies from the polarity of bulk water to that of bulk alkane. This is direct evidence that the interface is sharp – the width is no greater than the size of a C₆ “ruler”, that is, about 1 nm.

3. *Solute association and aggregation may affect the spectra significantly.* An example of this is the work of Teramae and coworkers who found that the SHG of rhodamine dyes adsorbed at the heptane/water interface exhibit spectral shifts that vary with bulk concentration³⁶⁵ due to association and structural rearrangements at the interface.
4. *Electronic structure is affected by the transfer of the solute probe to the interface.* A change in the solvent environment may affect the solute electronic structure^{366,367} and change the reported polarity. If the ground state solute polarizability is especially large, for instance, a positive solvatochromism may become negative with an increase in solvent polarity.^{332,368} As an example, Nagatani et al. have measured the SHG spectra of the free base and zinc(II) complex of cationic *meso*-tetrakis(*N*-methyl-4-pyridyl)porphyrins, H₂TMPyP⁴⁺, and ZnTMPyP⁴⁺ at the water/DCE interface, and compared them to the UV–vis spectra of these two species in the bulk of the two liquids.³⁶⁹ Although the molecular hyperpolarizability of the symmetrically substituted porphyrins is very small,³⁷⁰ the adsorbed species give rise to intense SH signals, indicating that its electronic structure at the interface is modified relative to the bulk structure.

While the resonant SHG is a powerful and sensitive technique for studying the structure of a neat interface using a solute probe, the signal-to-noise ratio of published data is of relatively poor quality. More importantly, the $|\chi^{(2)}|^2$ spectra cannot be compared directly with UV absorption spectra, and thus line shape information is not readily available, although qualitative correlations between SHG spectral width and the heterogeneity of the system can be made.^{23,360,361} Recently, Tahara and coworkers used heterodyne-detected electronic sum frequency generation (HD-ESFG) spectroscopy to measure the imaginary $\chi^{(2)}$ spectra, which, for the first time, can be compared with the bulk absorption line shape.³⁷¹ The effective polarity of the air/water interface, which was determined by the peak position, depended on the type of dye molecule used. Interestingly, the $\text{Im}[\chi^{(2)}]$ spectra at the air/water interface showed substantially broader bandwidths than do the UV absorption spectra taken in equally polar bulk solvents or even in bulk water. This suggests that the solvation environment at the air/water interface is more heterogeneous than that in bulk solvents, a point that will be further discussed below.

Computer Simulations of Electronic Transitions at Interfaces

A limitation of all the experimental methods used to learn about the interface structure from the behavior of adsorbed solute molecules is that the solute perturbs the interface to some degree. Computer simulations that reproduce the experimental data and provide molecular insight help provide a link between the neat and the perturbed structures. For example, simulations that reproduce the spectral shift of an adsorbed solute at a liquid/liquid interface can reveal the relative contribution of each solvent and provide an explanation of the average polarity rule mentioned earlier.^{372,373}

The methodology for computing electronic spectra discussed earlier has been used extensively to calculate absorption and emission spectra in bulk liquids. Exactly the same procedures can be used at liquid interfaces. We report here a few results that have provided complementary insight to the experiments. A more detailed review of this topic is provided in Ref. 363.

The key to the simulations involves developing accurate potential energy functions for describing the interaction of the two solute electronic states with the solvent(s). One simple approach is to use *ab initio* quantum calculations to determine the gas phase solute charge distribution in both the ground and excited states. These distributions are then adjusted, if necessary, to reproduce the ground state solute dipole moment and the peak position of the absorption spectra in the bulk. The Lennard-Jones parameters in the ground and excited states are typically set to be equal, but they can be adjusted if a significant change in atomic polarizability between the two electronic states exists. Alternatively, dynamic atomic polarizabilities in a many-body description of the potentials can be used. This is warranted if the experimental value of the solute's dipole moment in the bulk phase differs significantly from that of the gas phase.

The approaches described in the previous paragraph were used to compute the electronic absorption spectra of DEPNA (*N,N'*-diethyl-*p*-nitroaniline) at the water liquid/vapor and water/DCE interfaces, as well as in the bulk of these solvents.³⁷³ The same solute's potential energy functions were used in the calculation of the electronic spectra in all the systems. The excited state dipole moment of DEPNA was chosen so that the peak position of its spectrum in bulk water agrees with the experimental value of 429 nm. The half-width at half-height of the bulk spectrum was 34 nm, in good agreement with the experimental value of 37 nm,³⁵⁵ suggesting that the pure inhomogeneous broadening assumption made and the potential energy functions used are acceptable. The calculated peak position of the spectrum at the water liquid/vapor interface is 382 nm. Compared with the experimental value of 373 ± 4 nm,³⁵⁵ this is good agreement considering the crude model used for the excited state charge distribution. The calculated peak position at the water/DCE interface using a nonpolarizable model is 405 nm, compared with the experimental value of 415 ± 15 nm. While the calculations correctly suggest that this interface is more polar than the water liquid/vapor interface, its polarity is underestimated. The

problem is that the nonpolarizable DCE model used underestimates the ability of the highly polarizable DCE molecules to stabilize the large excited state dipole (17D), and indeed, the calculated peak spectrum in bulk DCE (370 nm) is significantly different from the experimental value of 398 nm. Switching to a polarizable DCE potential (using the method discussed in Eqs. [5] and [6]) improves the results: the peak position in bulk DCE is at 385 nm and 417 nm at the water/DCE interface. These simulations help explain why the peak of the interfacial spectrum is near the average of the two bulk phases: Due to the depletion of the hydration shell at the interface, the water contribution, which accounts for most of the spectral shift, decreases by about 50% relative to the bulk. The roughness of the water/DCE interface is also an important factor, because forcing the interface to remain flat by removing capillary fluctuations makes the interface much less polar.³⁷³

The role of many-body polarizable potentials in MD-based predictions of electronic spectra at the water liquid/vapor interface was examined by Benjamin³⁷⁴ for a model dipolar solute. The peak absorption spectrum was found to be more sensitive to the solvent polarizability than to the solute polarizability. The contribution of many-body polarizabilities was found to be more pronounced as the excited state dipole was increased, and more in the bulk than at the interface.

In addition to the intrinsic polarity of the bulk liquid(s), the solute location, and the solute structure, electronic spectral shifts may depend on some liquid surface structural features. In a study to demonstrate this,³⁷² a diatomic solute with charges and Lennard-Jones parameters designed to mimic approximately DEPNA was restricted to a narrow window at two different interface locations between water and four organic liquids representing various polarities and molecular structures: 1-octanol, DCE, *n*-nonane, and carbon tetrachloride. The electronic transition involves a change in the solute charge distribution that corresponds approximately to the experimental dipole moment jump in DEPNA. The spectral shifts relative to the gas phase are given in Figure 8. They clearly demonstrate that the effective surface polarity depends on the molecular structure of the interface (in addition to the polarity of the bulk liquids and the solute's location). For example, the water/ CCl_4 interface is more polar than is the water/*n*-nonane interface, despite (in these model calculations) the two liquids being purely nonpolar and nonpolarizable (as reflected by the values $\Delta\omega = 0$ in the bulk of these two liquids). An increased roughness of the interface between water and the nearly spherical CCl_4 molecules exist relative to the case where water is next to the long-chain hydrocarbon molecules. This roughening allows for better access of the water molecules to the solute molecule. Note also that despite the bulk octanol giving rise to a larger shift than does bulk DCE, the opposite is true when the probe is at the Gibbs surface, reflecting the greater roughness of the water/DCE interface.

The 1-octanol/water interface polarity was studied experimentally by Walker and coworkers using the molecular ruler idea discussed earlier.²³

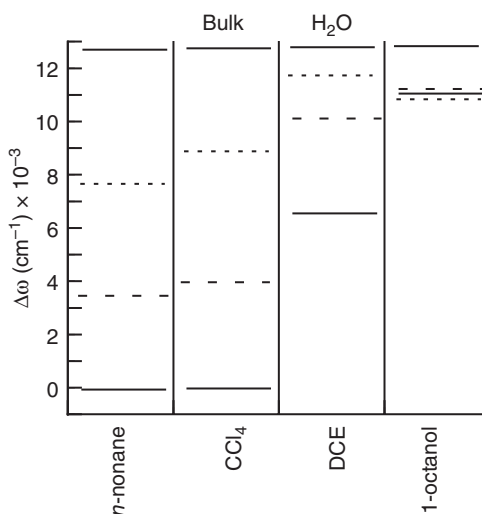


Figure 8 The electronic spectral shift relative to the gas phase of a model chromophore located in the bulk of several liquids (solid lines), at the Gibbs surface (dotted lines), and on the organic side of the Gibbs surface (dashed line). (Data taken from Ref. 372.)

Results suggest that at the water/octanol interface, a region exists whose polarity is *less* than that of bulk 1-octanol (and of bulk water). This finding was interpreted (and supported by simulations³⁷⁵) by considering the orientational preference of the long-chain 1-octanol molecules at the interface: The OH groups point toward the aqueous phase to form a monolayer, thus creating a purely hydrocarbon region, consisting of alcohol tails, extending a few Å away from the OH layer.

The above computational techniques can be used to study electronic transitions and the effective polarity of other interfaces, such as that between water and self-assembled monolayers, in micelles, and at liquid/solid interfaces. The interested reader can consult Ref. 363.

In closing this discussion of using electronic spectra to assess the polarity of the surface region, it should be mentioned that a cruder but sometimes useful approach one could take is to assign a dielectric constant to the surface region. While the static dielectric constant ϵ (and more generally, the frequency-dependent complex dielectric function $\epsilon(\omega)$) of a bulk liquid is a well-defined quantity that is experimentally and computationally accessible,^{79,376,377} it is not clear how to generalize this for application to the inhomogeneous region. This problem reflects the difficulties associated with using a direct experimental probe to examine the buried interface, and of applying the statistical mechanical theory of the dielectric response to an inhomogeneous region. The simplest, albeit inadequate, solution that has been used extensively^{288,363,378–381} is to assume the dielectric constant to be equal to the bulk value of one phase up to a mathematically defined sharp interface, at

which point it jumps to the constant bulk value of the second phase. A solution of the electrostatic boundary problem can be done in terms of image charges, and the genesis of the interface effect is the result of interactions between the solute molecules and these image charges. Most continuum electrostatic treatments of interfaces use this model, as mentioned earlier in our discussion of ion solvation. Its application to electronic spectra has been reviewed.³⁶³ A continuum description becomes increasingly inaccurate as distances from the interface become comparable to the size of a solute molecule. Another crude concept used in simple continuum models of interfaces for calculating adsorption free energy and electronic spectra involves the use of an “effective” interfacial dielectric constant. For example, the reduced orientational freedom of interfacial water molecules and their reduced density result in a smaller effective dielectric constant than in the bulk. This is consistent with assigning the water liquid/vapor a polarity value similar to that of CCl_4 . Finally, we mention that a molecular theory of a local dielectric constant, which reproduces interfacial electric fields, can be developed with the aid of molecular dynamics simulation as described by Shiratori and Morita.³⁸²

Our discussion thus far has been limited to the spectral peak shift. However, much information about solvent–solute interactions and the structural heterogeneity of the interface region can be derived from the electronic adsorption bandwidth.^{92,324,325,328–330,335,383} This information is also available from simulations, but as mentioned earlier, this topic has been only briefly investigated due to the lack of experimental data. One problem with the experimental data is that the electronic sum frequency spectra bandwidth cannot be compared directly with bulk absorption spectra. Another issue is that because spectral widths depend on the polarity of the medium,³²⁴ one must correct for this effect when using these linewidths to compare the degree of solvent inhomogeneity in *different* media.

The imaginary part of the second-order nonlinear susceptibility ($\text{Im}[\chi^{(2)}]$) of several coumarin dyes at the water–air interface has been measured using heterodyne-detected electronic sum frequency generation (HD-ESFG) spectroscopy.³⁷¹ The width of these spectra was found to be broader than the width of the $\text{Im}[\chi^{(1)}]$ derived from the UV spectra of the same chromophore in bulk solvents of similar polarity. This was attributed to the solute molecule sampling a wider distribution of solvent configurations at the interface than in the bulk. However, while the heterogeneity of the local solvation environment at the interface (e.g., due to orientational anisotropy) is an important factor, the contribution of molecules from across the whole interface region is as, or even more, important, as recent molecular dynamics simulations have demonstrated.^{384,385} To better address questions about electronic transition spectral widths, it will be important to develop accurate computational approaches to calculate $\chi^{(2)}$ directly.³⁸⁶

We note in closing that spectral line shape can also be determined within a continuum model description by taking into account the relationship

between the Gaussian spectral width and the free energy of the relevant charge distribution.^{324,381}

SOLUTES AT INTERFACES: DYNAMICS

Understanding the dynamical behavior of solute molecules at interfaces, together with the structure, thermodynamics, and spectroscopy discussed above, is a prerequisite for understanding their reactivity. Here we are concerned with the pathways by which solute molecules exchange energy with the solvent environment. Specifically, we describe three related phenomena: (i) solute vibrational energy and phase relaxation; (ii) rotational energy and reorientational relaxation, and (iii) solvation dynamics. These three phenomena are critical for understanding chemical reactivity in bulk liquids and are likely also to be important for understanding chemical reactivity at liquid interfaces. Unlike the materials covered in previous sections, little has been done in this area experimentally, and most of our current knowledge has been obtained from computational work. We now focus on computational methodology, the insight gained from it, and make comparisons with the much more established body of work in bulk liquids.

Solute Vibrational Relaxation at Liquid Interfaces

The rate and mechanism of vibrational energy and phase relaxation in condensed media are both determined by the structure and the nature of the solute–solvent interactions. Vibrational relaxation is of fundamental importance for understanding chemical reaction dynamics. Although many experimental and theoretical studies have focused on the relaxation of solute molecules in bulk liquids,^{209,387–413} far less has been done at liquid surfaces.^{403,414–421}

No direct measurements of the vibrational lifetime of solute molecules at liquid/vapor and liquid/liquid interfaces have been reported to date. However, vibrational energy relaxation times of N_3^- , NCO^- , and NCS^- inside the water pools of reverse micelles were measured and found to be about three times longer than in bulk water.⁴¹⁷ There are also several studies using time-resolved SFG measurements at liquid interfaces,^{422,423} which can follow vibrational spectral evolution, examining neat water at liquid/vapor and liquid/solid interfaces.^{195,196,423}

Given our current knowledge about the neat liquid interface structure and dynamics, the basic question regarding vibrational relaxation at liquid interfaces is: how do these structures and dynamics affect the relaxation rate? Are the same factors responsible for relaxation in bulk liquids applicable to relaxation at liquid interfaces, or, are there unique surface effects that also need to be taken into account?

The computational methods that have been developed for studying vibrational energy relaxation rate in bulk liquids can often be used with minor adjustments for studying vibrational relaxation at the interface. A typical system under study usually includes one solute molecule adsorbed at a liquid/vapor interface or at the interface between two immiscible liquids. To improve statistical accuracy and to evaluate the relaxation rate as a function of distance along the interface normal, one may use the windowing method discussed above to constrain the solute center of mass location to a slab of some narrow width. It is important that whatever method is used to study this process at the interface, the same should be used when calculating the relaxation in the bulk of the relevant liquid(s). This provides an accurate benchmark for assessing surface effects when one uses the same system potential energy functions the same way.

To focus on the question of surface effects on vibrational energy relaxation rate, without the complications of intramolecular energy flow, Benjamin and coworkers studied the vibrational relaxation of a diatomic solute molecule (single vibrational mode) at various liquid/vapor and liquid/liquid interfaces.⁴²⁴ The solute is modeled using the Morse potential:

$$V(R) = D_e [e^{-\alpha(R-R_{eq})} - 1]^2 \quad [40]$$

which describes an anharmonic oscillator. The parameters D_e and R_{eq} are typically taken to match the experimental dissociation energy and equilibrium bond length, respectively, and the parameter α is selected to reproduce the gas phase vibrational frequency ω_0 .

The computational approach employs *nonequilibrium* classical trajectories to determine the rate. The solute is prepared with an initial vibrational energy $E_0 = \frac{p_R^2(0)}{2\mu} + V(R_0)$, where $p_R(0)$ is the initial momentum along the diatomic bond, R_0 is the initial bond length, and μ is the diatomic reduced mass. E_0 is significantly larger than the classical equilibrium value of kT per vibrational mode. All other solute and solvent degrees of freedom are selected from a thermal distribution at the temperature T . The trajectory is run in the NVE ensemble for a period of time long enough for the energy to relax to the equilibrium value of $E_\infty = kT$. A few hundred trajectories with a distribution of initial conditions are run to determine the normalized nonequilibrium correlation function:²¹²

$$S(t) = \frac{\overline{E}_t - \overline{E}_\infty}{\overline{E}_0 - \overline{E}_\infty} \quad [41]$$

where \overline{E}_t is the average vibrational energy of the solute at time t . In some cases, $S(t)$ is found to be a simple exponential $S(t) = e^{-t/\tau}$, describing a relaxation with a lifetime τ . Otherwise, the average lifetime may be calculated from $S(t)$ using:

$$\tau_{NE} = \int_0^\infty S(t) dt \quad [42]$$

Independently, the vibrational lifetime can be estimated by using classical equilibrium MD to approximate the quantum first-order perturbation theory expression for the vibrational relaxation rate (inverse of the lifetime). The quantum relaxation rate of a vibrational mode coupled to a bath is proportional to the Fourier transform of a force along the vibrational coordinate correlation function.³⁸⁷ The idea is to approximate this correlation function using classical equilibrium MD trajectories.^{395,397,425–428}

In the case of a diatomic solute, if \mathbf{F}_A and \mathbf{F}_B are the total forces on the two atoms (calculated while the bond length is kept rigid), the force along the vibrational coordinate is given by⁴²⁹ $F = \mu(\mathbf{F}_A/m_A - \mathbf{F}_B/m_B) \cdot \mathbf{n}_{AB}$, where \mathbf{n}_{AB} is a unit vector in the direction of the diatomic bond and the Fourier transform is

$$\zeta(\omega) = \int_{-\infty}^{\infty} \langle \delta F(t) \delta F(0) \rangle \cos(\omega t) dt \quad [43]$$

where $\delta F = F - \langle F \rangle$ and $\langle \dots \rangle$ denotes an equilibrium ensemble average. The lifetime is then given by the Landau–Teller formula:^{387,430,431}

$$\tau_{LT} = \mu kT / \zeta(\omega_{eq}) \quad [44]$$

where ω_{eq} is the equilibrium oscillator frequency (typically different from the gas phase value ω_0). The Landau–Teller result is a reasonable approximation for low-frequency vibrations at high temperatures. An approximate quantum correction is obtained by multiplying Eq. [43] by the correction factor $\beta \hbar \omega / (1 - e^{-\beta \hbar \omega})$. This correction gives the exact quantum results for a harmonic oscillator coupled to a harmonic bath.^{432,433}

The above nonequilibrium and equilibrium approaches have been used to study the vibrational relaxation of ionic and nonionic solutes at the liquid/vapor interface of water,^{434,435} as well as at the liquid/vapor interface of the weakly polar solvent acetonitrile (CH_3CN),⁴³⁶ and at different locations at the water/ CCl_4 liquid/liquid interface.⁴³⁷ The bulk relaxation rates were found generally to be in good agreement with experimental data, giving some support for the methodology selected and the potential energy surfaces used. Fair agreement was found between the nonequilibrium trajectory calculations of the lifetime and the Landau–Teller results (especially for the low-frequency oscillators). These latter results were used to gain insight into the molecular factors influencing the rate, because in the Landau–Teller model the force correlation function can be split into electrostatic and a nonelectrostatic interaction contributions, as well as the contributions from the different solvents (in the case of the liquid/liquid interface).⁴³⁷

Lifetimes at the liquid/vapor interface for several diatomic solutes compared with the same calculations carried out in the bulk are summarized in Table 1. We note that the vibrational lifetime is always greater at the liquid/vapor interface than in the bulk. However, while for neutral solutes (polar or nonpolar) the surface effect is large, $\tau_{\text{surf}}/\tau_{\text{bulk}} \approx 3.1\text{--}3.5$, for the

Table 1 Calculated Vibrational Lifetime of Different Solute Molecules at the Liquid/Vapor Interface of Several Solvents at 298 K^{434,436}

Solute	Solvent	τ_{bulk} (ps)	τ_{surf} (ps)	τ_{surf} (ps)/ τ_{bulk} (ps)	$g_{\text{max}}^{\text{bulk}}/g_{\text{max}}^{\text{surf}}$
I ₂ ⁻	H ₂ O	0.60	0.90	1.5	1.6
I ₂	H ₂ O	5.4	16.6	3.1	3.0
ClO	H ₂ O	7.9	28.2	3.5	3.2
ClO ⁻	H ₂ O	0.64	0.69	1.1	1.2
ClO	CH ₃ CN	179	555	3.1	2.8
ClO ⁻	CH ₃ CN	13.9	14.3	1.0	1.0

ionic solutes the surface effect is much smaller. For I₂⁻ in water, for example, $\tau_{\text{surf}}/\tau_{\text{bulk}} \approx 1.5$, and for ClO⁻ in water and in acetonitrile, $\tau_{\text{surf}}/\tau_{\text{bulk}} \approx 1.1$. Table 1 also shows remarkable correlations between the surface effect on the lifetime and on the peak value of the solvent–solute radial distribution function: $\tau_{\text{surface}}/\tau_{\text{bulk}} \approx \max(g_{\text{bulk}})/\max(g_{\text{surface}})$. This latter correlation and our discussion of molecular structure of interfacial solvation suggests a simple explanation for the surface effect on vibrational lifetime.

A key concept to consider in this regard is that vibrational relaxation is dominated by short-range repulsive forces, despite the fact that most of the contribution to the solvation energy is electrostatic for ionic solutes. The vibrational relaxation is determined by the magnitude of the *fluctuations* in the instantaneous force along the oscillator coordinate. Fluctuations in the rapidly varying repulsive interactions are much larger than those produced by the slowly varying electrostatic interactions.^{394,395} The strong attractive electrostatic forces do have an important role: they place the solvent–solute equilibrium intermolecular distance within the rapidly varying repulsive region of the Lennard-Jones potential. We noted earlier that ionic solutes are better able to preserve their solvation shell than neutral solutes as they are moved from the bulk to the interface, and this is reflected in the ratio of the peak values of the radial distribution functions shown in Table 1. Retaining a solvation shell helps preserve the contribution of the short-range repulsive forces as an ionic solute is transferred to the surface, but less so when a nonionic solute is transferred. The degree to which the short-range repulsive forces are preserved is directly proportional to the peak value of $g(r)$, thus explaining the correlation indicated in the table. To say it differently, the reduced local density at the liquid/vapor interface decreases the vibrational friction and increases the lifetime, but an ionic solute is able to preserve somewhat the bulk local solvent density and thus mute the surface effect on the lifetime. Recall that the ability of the ionic solute to preserve its hydration shell increases as its size is reduced. This explains the difference in behavior between I₂⁻ and ClO⁻. The increase in vibrational lifetime when nonionic solutes are transferred from the bulk to the liquid/vapor interface was also observed in several triatomic molecules.^{435,438}

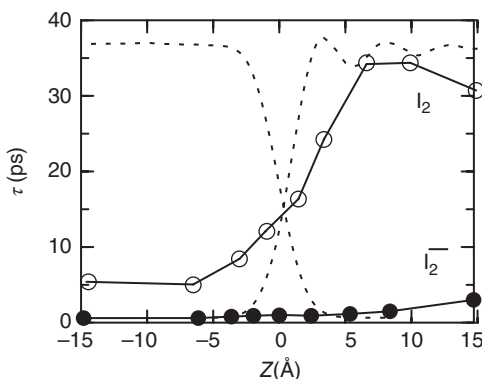


Figure 9 The vibrational lifetime of I_2^- (solid circles) and I_2 (open circles) at different locations across the water/ CCl_4 interface. The density profiles of water (on the left) and CCl_4 (on the right) are shown in dotted lines. (Figures adapted with permission from Ref. 437. Copyright 2004 American Institute of Physics.)

We next consider vibrational relaxation at the interface between water and an immiscible liquid. Though total density remains relatively constant on transferring the solute from bulk water across the interface, the change in the hydration shell structure produces a change in the vibrational lifetime that follows the same principle discussed above, namely, that an ionic solute is able to keep its hydration shell. This principle manifests itself in the increase in surface roughness on ion transfer across the liquid/liquid interface, as noted earlier.

Consider the example in Figure 9 of vibrational lifetime *profile* of I_2^- and I_2 across the water/ CCl_4 interface, calculated when the solutes are in parallel slabs of 3 Å width.⁴³⁷ The vibrational lifetimes of these solute molecules in the two bulk liquids are in reasonable agreement with experiments and are also in good agreement with the simple Landau Teller model. The LT model attributes the faster relaxation in bulk water than in bulk CCl_4 to its greater density of phonon states in the region of the solute vibrational frequency.⁴³⁷ In addition, the electrostatic forces pull the water molecules tighter around the ionic solute, increasing the Lennard-Jones component of the friction.

As I_2 is moved from bulk water to bulk CCl_4 , the relaxation time increases monotonically and uniformly across the interface from a value of 5 ps in bulk water to around 30 ps in bulk CCl_4 . The profile approximately tracks the change in the density profile of water. Contrarily, as the I_2^- crosses the interface, its relaxation time remains close to the value in bulk water, reaching the value expected in bulk CCl_4 only when it is deep into the organic side of the interface.

Here is the explanation for this behavior: as the nonionic I_2 is transferred from bulk water to bulk CCl_4 , the number of water molecules in the solute's hydration shell (representing the main contribution to the fluctuating force on the I–I bond) decreases rapidly and monotonically. This induces an

increase in the I_2 vibrational lifetime. In contrast, as the ionic solute crosses the interface, the partly retained hydration shell sustains a significant portion of the fluctuating force, and only a weak variation of the vibrational lifetime across the interface is observed. This latter effect can be shown by calculating directly the contributions of the two solvents to the total friction. As was the case at the liquid/vapor interface of water, a high degree of correlation exists between the height of the first peak of the water-solute radial distribution function and the vibrational relaxation rate.⁴³⁷

The normal dynamic capillary roughness of a neat liquid/liquid interface is magnified when an ionic solute (especially a small one) crosses the interface. The results in Table 1 suggest a correlation between the solute's vibrational lifetime and the interface roughness. This can be demonstrated more directly by forcing the liquid/liquid interface to remain flat, a technique often used to investigate the role of surface roughness. This is accomplished by adding to the system Hamiltonian a small external potential that is coupled to surface fluctuations and keeps the interface molecularly sharp and flat. The results, described in detail in the original paper,⁴³⁷ show that removing capillary fluctuations has no effect on the neutral solute vibrational relaxation while the relaxation time of the ionic solute rises significantly as it crosses the flat interface.

Solute Rotational Relaxation at Liquid Interfaces

Solute rotational energy and orientation relaxation have been heavily studied in bulk liquids experimentally using a variety of techniques and also theoretically mainly with continuum models and MD.^{219–221,439–468} In contrast, time-resolved studies at liquid interfaces are much more difficult to do, so they have been limited to several time-resolved SHG and SFG measurements addressing the reorientation dynamics of dye molecules at the water liquid/vapor interface.^{223,469–475} A few theoretical studies using molecular dynamics simulations have appeared.^{228,476–479} They have been motivated by some conflicting reports about the ability of the interface region to enhance⁴⁷² or to slow down^{469–471,473} the reorientation dynamics of adsorbed solute molecules.

The many studies in bulk liquids have clarified contributing factors that influence rotational dynamics in condensed media. A natural question is: how do these factors play out at liquid interfaces? In particular, liquid density and polarity have been identified as two of the most important factors affecting rotational energy and reorientation relaxations in the bulk, and, as discussed earlier in this chapter, both are modified significantly at liquid interfaces.

The reduced density at a liquid/vapor interface is expected to lower the collision frequency and to reduce the rate of rotational energy relaxation. At the same time, fewer collisions enable faster scrambling of molecular orientations and thus are expected to increase the rate of orientational relaxation (as long as

the density is not too low²¹⁹). These contributing influences can be quantified using the concept of mechanical (or hydrodynamic) friction.²²¹

In polar liquids, a polar solute experiences an additional friction, called the dielectric friction, produced by a lag in the electrostatic forces as the solute dipole rotates away from its equilibrium orientation.^{221,440,442,443,480} The reduced polarity at the liquid–vapor and water–organic liquid interfaces^{355,363} is thus expected to slow energy relaxation and speed up reorientation. However, surface roughness, capillary fluctuations, and the ability of an ionic solute to keep its hydration shell can complicate this picture.

The reorientation dynamics can be studied theoretically by computing the equilibrium orientational correlation function,²²⁰ defined as:

$$C_l(t) = \langle P_l[\mathbf{d}(t) \cdot \mathbf{d}(0)] \rangle \quad [45]$$

where $\mathbf{d}(t)$ is a unit vector fixed in the molecular frame of reference (or simply along the bond in the case of the diatomic solute), and P_l is the l th order Legendre polynomial. For example, $P_1(x) = x$, so $C_1(t) = \langle \cos \theta(t) \rangle$. The average orientational relaxation time is taken as the integral:

$$\tau_l = \int_0^\infty C_l(t) dt \quad [46]$$

In bulk isotropic media, experiments such as IR and NMR spectroscopy and fluorescence anisotropy decay can give information about these correlation functions or their moments.^{220,221} At an interface with a cylindrical symmetry, SHG and SFG spectroscopies give information about out-of-plane and in-plane reorientation, and they involve more complicated time correlation functions.^{196,223,226,481} Nonetheless, the simple $C_l(t)$ are still useful for a direct comparison between bulk and surface reorientation.

At an early time, prior to the “first” collision between the solute and the solvent molecules, the orientational correlation function has a typical Gaussian time-dependency, reflecting a period of free inertial rotation:²¹⁹

$$C_l(t) \approx e^{-(kT/2I)l(l+1)t^2}, \quad t < \tau_0 \quad [47]$$

where τ_0 is the time it takes the solute to complete one rotation. At longer times, if the rotation is highly hindered, it can be viewed as a succession of very small angle jumps around a randomly oriented axis, and the dynamics follow a simple diffusion model giving:²¹⁹

$$C_l(t) = \exp[-l(l+1)D_r t] \quad [48]$$

Whether the actual dynamics follow these two expressions can be checked by MD simulations to gain insight into the solute reorientational mechanism.

To investigate rotational energy relaxation, one can compute the rotational energy equilibrium correlation function and the corresponding energy relaxation time τ_E :

$$C_E(t) = \frac{\langle \delta E(t + \tau) \delta E(\tau) \rangle}{\langle \delta E(\tau) \delta E(\tau) \rangle}, \quad \delta E = E - \langle E \rangle \quad [49]$$

$$\tau_E = \int_0^\infty C_E(t) dt \quad [50]$$

For a diatomic solute, the rotational energy is $E = J^2/2I$, where I is the solute's moment of inertia and J its angular momentum. $\langle E \rangle = RT$ is the classical equilibrium average of the diatomic solute rotational energy at the temperature T .

Rotational relaxation can also be investigated by nonequilibrium simulations. The solute molecule is subjected to an instantaneous jump in its angular momentum, and the energy and orientations dynamics are followed. This is repeated for an ensemble of initial solute positions and velocities, from which time-dependent averages are computed.

To discern what controls rotational dynamics at liquid interfaces, molecular dynamics simulations were performed on a model diatomic solute at different locations in both the water liquid/vapor interface⁴⁷⁸ and the water/CCl₄ interface.⁴⁷⁹ The solute was modeled as two identical atoms separated by a rigid bond of length 4 Å (using the SHAKE algorithm⁴⁸²). The assigned mass of each atom is 35 amu, giving the value $\tau_0 = (2\pi/9)(I/kT)^{1/2} = 1.05$ ps for the time it takes the molecule to complete one rotation in the gas phase. Various solute electric dipole moments were considered by placing partial charges $q_s, -q_s$ onto the two atoms, with $q_s = 0, 0.1, 0.2, 0.3, 0.4, 0.6, 0.8$ (atomic units). The resulting dipole moment, $\mu(D) = 19.212q_s$, spans approximately the range of dipoles encountered in experimental studies of rotational dynamics in bulk liquids and at interfaces. The solute molecule center of mass was typically constrained to 3–4 Å-wide slabs centered at different surface locations.

The top panel of Figure 10 shows the reorientational relaxation time τ_2 as a function of the solute's electric dipole moment, when the solute's center of mass is constrained to a slab of width 4 Å centered at the Gibbs surface (labeled G), 3.5 Å “above” the Gibbs surface (S), and in bulk water (B). As expected, in every location the relaxation time increases with the increase of the solute dipole moment, reflecting the increase in the dielectric friction. For relatively small solute dipole moments ($\mu < 6D$), the friction is dominated by the “mechanical” density-dependent contribution, and the relaxation in the higher density bulk region is much slower than the relaxation at the interface. However, as the dipole moment is increased, the bulk and the surface reorientation relaxation times become similar. This behavior, which mirrors that of the

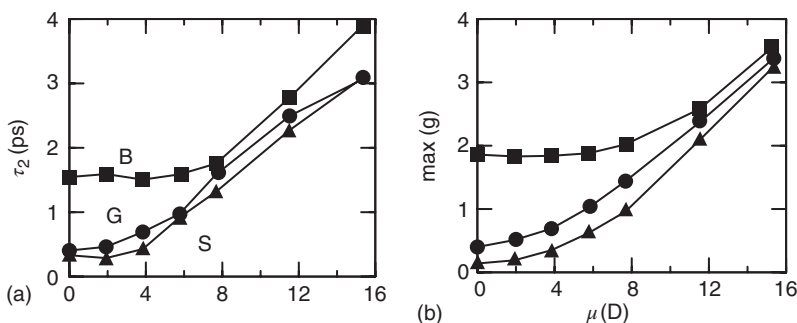


Figure 10 Dipolar solute equilibrium reorientation time at the water liquid/vapor interface. (a) The reorientation time τ_2 as a function of the solute's dipole moment. The solute is located in the bulk (B, squares), at the Gibbs surface region (G, circles) and 3.5 Å "above" the Gibbs surface (S, triangles). (b) the peak value of $g(r)$ versus the dipole moment for all solute molecules studied. Squares, circles, and triangles correspond to regions B, G, and S, respectively. (Reprinted with permission from Ref. 478. Copyright 2007 American Institute of Physics.)

vibrational relaxation discussed in the previous section, is due to the solute's ability to keep the hydration shell to a degree that increases with the increase in its dipole moment. This keeps the surface rotational friction similar to that in the bulk. The correlation between the relaxation time and the peak value of the solute radial distribution function, shown in the bottom panel, is further evidence for the role played by the first hydration shell, much like what is observed for the vibrational relaxation.

The energy relaxation time, Eq. [50], as a function of the magnitude of the solute's dipole and its location exhibits an opposite trend.⁴⁷⁸ The increased collision rate (which slows down reorientation) enhances the rotational energy transfer to the solvent molecules. Thus, for a solute with a small dipole, the energy relaxation at the interface is much slower than in the bulk. However, the difference between the bulk and surface energy relaxation rates decreases as the dipole is increased because preserving the solute hydration shell makes the interfacial friction similar to that of the bulk, despite the fact that the average solvent density just outside the solute hydration shell is smaller than in the bulk.

Nonequilibrium energy relaxation rates, calculated using nonequilibrium MD, are somewhat slower than the equilibrium rates in the case of a nonpolar solute but are almost the same for polar solutes.⁴⁷⁸ However, the trends in relaxation times as a function of solute dipole and location are essentially the same as the equilibrium trends discussed above. The difference between equilibrium and nonequilibrium rotational relaxation reflects, in part, the difference between the equilibrium structure of the solute-solvent complex.^{468,483} The insight gained from studying a simple diatomic solute has been useful for understanding the rotational behavior of large dye molecules.⁴⁸⁴

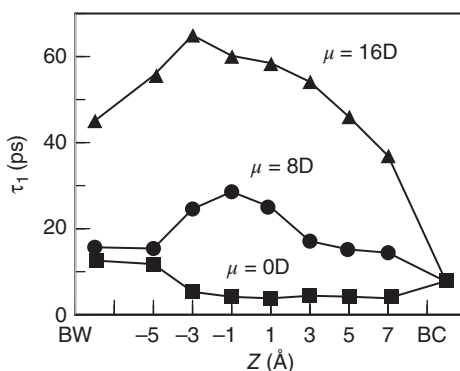


Figure 11 Dipolar solute equilibrium reorientation time τ_1 as a function of the solute's center of mass location along the water/ CCl_4 interface normal. The solute dipole in Debye is indicated. BW and BC refer to bulk water and bulk CCl_4 , respectively. (Reprinted with permission from Ref. 479. Copyright 2008 American Chemical Society.)

Let us now consider the reorientation dynamics at the liquid/liquid interface. The most significant contrast with the liquid/vapor interface is that there is no longer a low-density region (although the bulk viscosity of the two solvents may be quite different). Instead, a large variation in solvent polarity may introduce a marked difference in the dielectric friction for a highly polar solute.

A systematic study of the rotational relaxation, of the diatomic solute described above, at the water/ CCl_4 interface has been carried out.⁴⁷⁹ The solute molecules' equilibrium reorientation correlation functions, Eq. [45], were evaluated at different interface locations and in the bulk of the two solvents. Some of the results for the reorientation time τ_1 are reproduced in Figure 11.

The reorientation of the nonpolar solute ($\mu = 0$, squares) in bulk water is slightly slower than in bulk CCl_4 , reflecting the somewhat greater viscosity of water. Because CCl_4 is nonpolar, increasing the solute dipole has no effect on the reorientation time in that medium. In contrast, the reorientation time in bulk water increases as the solute dipole is increased, due to the greater dielectric friction.^{221,440,442,443,445,480,485–487}

As the solute is moved from the bulk across the interface, the reorientational behavior depends on the solute dipole in a surprising way. Contrary to the expectation that the surface reorientation time would lie between the two bulk phase values, Figure 11 shows that the reorientation at the interface is slightly faster than in either of the two bulk phases for a nonpolar solute but is significantly slower than either of the bulk phases in the case of a polar solute.

Lower effective viscosity at a liquid/liquid interface has been correlated experimentally with spherical molecular shapes⁴⁶ and theoretically with high surface tension.⁷⁴ A local dip in density is also a feature of liquids that partially wet hydrophobic surfaces.⁴⁸⁸ These observations may explain the reduced effective viscosity experienced by the nonpolar solute at the water/ CCl_4 interface, but, this remains an open issue, as the X-ray reflectivity measurements

of the water/liquid hydrocarbon interface, discussed earlier, failed to detect a lower density region.¹⁴⁶

The longer reorientation time of a polar solute at some surface locations compared to being in bulk water suggests the existence of a higher local dielectric friction despite the lower polarity at the interface. A similar effect was observed in the MD simulation of an actual dye molecule. It was found that *N,N'*-diethyl-*p*-nitroaniline rotates *slower* at the water/DCE interface than in either of the two bulk liquids.³⁷³ A possible explanation for this invokes a coupling between dielectric and hydrodynamic friction and a concept we are already familiar with: the strong electrostatic interactions enable the solute to retain a significant fraction of its hydration shell, depending on the magnitude of its dipole. This gives rise to a solute-water hydration complex that is quite stable at the interface. Its larger volume results in a significantly larger hydrodynamic friction and slower rotation.⁴⁵⁵ When the solute is moved deeper into the organic side of the interface or when the magnitude of the dipole is reduced, the hydration complex breaks down, and its rotation speeds up.

Finally, we note that the behavior of different correlation functions $C_l(t)$ (Eq. [48]) with $l = 1-5$ shows diffusional behavior for the largest dipole solute (16D) at both the water liquid/vapor interface and at the water/ CCl_4 interface. Breakdown of this relationship is observed when the solute hydration shell is diminished, for example, in bulk CCl_4 and for the nonpolar solute at both interfaces. In these cases, the dynamics can no longer be viewed as being small successive angular jumps around a randomly oriented axis. Instead, individual trajectories show sudden and large free rotation segments around a fixed axis. This has also been observed for the rotation of large dye molecules at the water liquid/vapor interface.⁴⁷⁷

Solvation Dynamics

Given a solute in equilibrium with solvent molecules, a sudden change in the solute's electronic structure due to an absorption of electromagnetic radiation or an electron transfer will generally create a nonequilibrium state. The solvent electronic and nuclear degrees of freedom will respond to reestablish equilibrium. These solvent dynamics can be monitored experimentally. Assuming an instantaneous response of the solvent electronic degrees of freedom, the slower solvent response involves translation, rotation, and vibration of the solvent molecules, which can be followed by classical molecular dynamics. Because experimental and theoretical studies of solvation dynamics can reveal important phenomena needed to understand solvent dynamics and solute-solvent interactions, they have been reviewed extensively.^{377,390,489-492} Solvation dynamics studies at liquid surfaces have also been reviewed.^{27,363} Here we give only a brief summary focusing on the unique surface effects, which, we will see, are similar to the effects discussed above regarding vibrational and rotational relaxation.

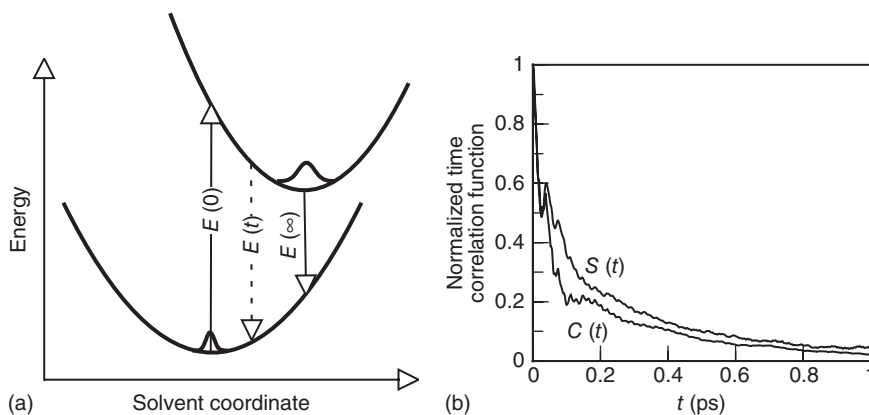


Figure 12 (a) A schematic representation of the energy changes involved in a time-resolved fluorescence experiment. (b) The equilibrium $C(t)$ and nonequilibrium $S(t)$ solvation dynamics correlation functions corresponding to the creation of a 12D dipole in bulk water. (Adapted with permission from Ref. 537.)

Consider two solute electronic states, $|a\rangle$ and $|b\rangle$. At time $t = 0$, the solvent is at equilibrium with state $|a\rangle$. Let $\Delta E(0)$ denote the average energy difference between these two states, including the interaction energy with the solvent, immediately following the transition $|a\rangle \rightarrow |b\rangle$. As the solvent equilibrates to the state $|b\rangle$, the energy difference evolves in time, reaching the value $\Delta E(\infty)$ when equilibrium is reached. The dynamical response of the solvent(s) can be followed using the nonequilibrium time correlation function:

$$S(t) = \frac{\Delta E(t) - \Delta E(\infty)}{\Delta E(0) - \Delta E(\infty)} \quad [51]$$

In Time Resolved Fluorescence (TRF) experiments, depicted schematically in Figure 12, the emission spectrum line shape changes from a peak value of $\Delta E(0)$ to the final $\Delta E(\infty)$ peak of the equilibrium emission spectrum as the solvent responds to the new solute electronic state.^{493,494} Experimental results in bulk liquids show that the nonequilibrium correlation functions initially exhibit a very fast (less than 50 fs⁴⁹⁵) inertial component, which may account for 60–80% of the total relaxation in water. This is followed by a multiexponential relaxation on the subpicosecond to picosecond timescale,⁴⁹⁶ corresponding to reorientation and translation of solvent molecules, or, to particular intramolecular solvent modes^{493,497} around the solute. Slower dynamics are found in more viscous liquids.⁴⁹⁸

While TRF and other techniques have been used extensively to probe solvent dynamics in bulk liquids^{377,390,489,490,499} and in micelles and reverse micelles and other complex environments,^{377,498,500–509} it is not surface specific and cannot generally be used to study solvent dynamics at liquid

interfaces, unless the solute is adsorbed strongly at the interface with little bulk concentration. (Exceptions include using TRF in total reflection geometry.^{510–512}) Solvation dynamics at liquid interfaces has been mainly studied using Time-Resolved Resonance Second Harmonic Generation (TRSHG)^{513–517} and recently using Time-Resolved Sum Frequency Generation (TRSFG) spectroscopy.⁵¹⁸ In TRSHG, an optical pump pulse excites the solute molecules to an electronic excited state. A time-delayed probe pulse with a frequency ω generates a second harmonic pulse with frequency 2ω from only the interfacial molecules. As the solvent molecules reorganize around the excited molecule, the resonant SH signal changes with the delay time, allowing for the construction of the $S(t)$ correlation function.^{513,514} The solvation dynamics of coumarin 314 (C314) adsorbed at the air–water interface was measured using TRSHG⁵¹³ and found to be similar to that in bulk water (0.8 ps). Experiments with polarized pump pulses in the direction parallel and perpendicular to the interface showed that the solvation dynamics depend on the solute orientation, being faster when the pump pulse is parallel to the interface.⁵¹⁴ The solvation dynamics of C314 adsorbed at the air–water interface in the presence of neutral, anionic, and cationic surfactants show that electric field of the dye and interactions with specific hydrophilic groups can slow down interfacial water dynamics.^{515,516,519,520}

Solvation dynamics has been studied computationally by nonequilibrium MD as well as equilibrium classical MD techniques. Let H_a and H_b denote the total Hamiltonian of the system when the solute is in the $|a\rangle$ and $|b\rangle$ electronic states, respectively. Following a sudden transition, the initial equilibrium distribution with respect to H_a evolves under the Hamiltonian H_b . Clearly, the time-dependent energy gap needed to compute $S(t)$ is $\Delta E(t) = H_b(\mathbf{r}) - H_a(\mathbf{r})$, where \mathbf{r} is the instantaneous system atomic positions. A set of initial conditions selected from the $|a\rangle$ state equilibrium distribution is propagated under the Hamiltonian H_b , and the energy gap at each time step is averaged over all the independent trajectories. If H_b contains polarizable terms, they must be equilibrated before the energy gap is calculated. Because the energy gap is calculated as a difference between two different potential energy functions at the same nuclear configuration, in general one must compute both at each step. In practice, however, because the sudden change in the electronic state involves a jump in the value of a few parameters like the solute dipole moment, $H_b(\mathbf{r}) - H_a(\mathbf{r})$ is a simple expression that in many cases is already evaluated during the normal simulations with the Hamiltonian H_b .

The equilibrium calculation of solvation dynamics involves computing the equilibrium time correlation function:

$$C_v(t) = \frac{\langle \delta E(t) \delta E(0) \rangle_v}{\langle \delta E(0) \delta E(0) \rangle_v}, \quad \delta E(t) = \Delta E(t) - \langle \Delta E(t) \rangle_v \quad [52]$$

where $\langle \rangle_v$ means the equilibrium ensemble averages with the dynamics governed by the Hamiltonian H_v ($v = |a\rangle$ or $|b\rangle$) and $\Delta E(t) = H_b(\mathbf{r}) - H_a(\mathbf{r})$.

If one invokes the linear response approximation, then^{336,521}

$$S(t) = C_a(t) = C_b(t) \quad [53]$$

While in many cases solvent dynamics follow the linear response approximation, even for large perturbations away from equilibrium, it is expected to fail when the equilibrium fluctuations do not sample important regions of phase space in which the nonequilibrium dynamics takes place.^{468,483,522–526} Thus, calculations of both $S(t)$ and $C_v(t)$ are useful for elucidating the mechanism of solvent dynamics. Figure 12 shows as an example the computed $S(t)$ and $C(t)$ for a sudden creation of a 12D dipole in bulk water (see below for more details about these calculations).

Approximate analytical theories of solvation dynamics are typically based on the linear response approximation and additional statistical mechanics or continuum electrostatic approximations to $C_v(t)$. The continuum electrostatic approximation requires the frequency-dependent solvent dielectric response $\epsilon(\omega)$.³⁹⁰ For example, the Debye model, for which $\epsilon(\omega) = \epsilon_\infty + (\epsilon_0 - \epsilon_\infty)/(1 + i\tau_D\omega)$, predicts that the solvation dynamics will follow a single exponential relaxation:

$$S(t) = e^{-t/\tau_L}, \tau_L = \epsilon_\infty \tau_D / \epsilon_0 \quad [54]$$

where τ_L is called the longitudinal relaxation time, τ_D is the Debye relaxation time, and ϵ_0 and ϵ_∞ are the static and infinite-frequency dielectric constants of the liquid. This simple Debye model can be improved by selecting a more complicated expression for $\epsilon(\omega)$ (e.g., as a sum of Debye-like terms for different molecular motions⁴⁹³). Other approximations take into account the finite size of the liquid molecules.^{527–530}

Extensive theory and computer simulation work has been able to clarify the molecular mechanisms of solvation dynamics in bulk liquids over the past three decades.^{390,491} One of the most important conclusions from this body of work is that most of the contribution to polar solvation dynamics comes from the solute's first solvation shell.⁵³¹ This conclusion and the earlier discussion about the prominent role the solute hydration shell plays in understanding vibrational and rotational dynamics at liquid interfaces suggest that surface effects on solvation dynamics will be muted as the solute's polarity is increased. An experimental validation of this are the similar solvation dynamics of C314 at the water liquid/vapor interface and in bulk water, mentioned above, where the highly polar excited state ($\mu = 12$ D) implicates an interfacial hydration structure similar to the bulk.

The first simulations of solvation dynamics at liquid interfaces involved the hypothetical sudden “charging” of an ion.^{228,532} The dynamical response at the water liquid/vapor interface and in the bulk are almost identical. Each $S(t)$ shows a very rapid initial relaxation, corresponding to inertial solvent motion,^{495,521,533} followed by a nearly exponential decay. The major factor

explaining the similar bulk and surface response is the ability of the ion to keep its hydration shell almost intact.²²⁸ Interestingly, this suggests that a dielectric continuum model parameterized to fit the bulk relaxation will fail to account for the surface dynamics. Twelve years passed until the next simulation of solvation dynamics at the water liquid/vapor interface was done by Pantano and Laria.⁴⁷⁷ They found the solvation dynamics of C314 to be only slightly slower at the interface (0.79 ps) than in the bulk (0.56 ps), agreeing with experiment. These results are consistent with having an interfacial hydration structure similar to the one in the bulk. The initial fast inertial drop accounted for 50% of the overall relaxation in the bulk compared with 35% at the interface. The linear response approximation was found to be valid, as the equilibrium time correlation function was in excellent agreement with the nonequilibrium one.

In addition to the important role played by the structure of the polar (and ionic) solute's hydration shell, a new factor comes into play at the liquid/liquid interface: the relatively slow solvent translational motion associated with capillary fluctuations and the related larger structural deformation of the interface. These slow dynamics were demonstrated in the first study of solvation dynamics at a model liquid/liquid interface, where a diatomic nonpolar solvent is in contact with a diatomic polar solvent.⁵³⁴ The electronic transitions studied were a charge separation ($A-D \rightarrow A^+ - D^-$) and the reverse, a charge recombination process, taking place between donor-acceptor pairs. The dynamics at the interface were significantly slower than those in the bulk, especially for the charge separation process when the $A-D$ vector is perpendicular to the interface. This retardation arises from the sudden creation of a large dipole that requires large structural reorganization to reach equilibrium, while a significant portion of configuration space is occupied by nonpolar solvent molecules. A significant deviation from the linear response results, but only for the charge separation process, because the equilibrium fluctuations in the final state sample very different structures from those that are required to reach equilibrium beginning from a neutral AD pair.

When two liquids with very different bulk Debye relaxation times are in contact, a very sharp liquid/liquid interface leads to a large dependence of the solvation dynamics on the solute's location. This is similar to the solvatochromic shift dependence of an adsorbed solute on its location as discussed earlier. This position dependence was demonstrated by following charge creation at different locations in the water/octanol interface.⁵³⁵ The relaxation time changed by two orders of magnitude when its position was varied by a few Å relative to the interface. Because the dynamics depends on different solvents, the interface behavior is typically characterized by a multiexponential relaxation (following an inertial component). This solvent dependence and dependence on surface location were illustrated by a systematic study of dynamics behavior following a change in the permanent dipole of a dipolar solute at four liquid/liquid interfaces consisting of solvents with different polarities and molecular structures.⁵³⁶ As above, a slow component was found not to

Table 2 Calculated Solvation Dynamics from Equilibrium and Nonequilibrium Simulations Following Two Types of Electronic Transitions⁵³⁷

Electronic Transition $\mu_a \rightarrow \mu_b$	Bulk H ₂ O	Liquid/Vapor H ₂ O, Gibbs Surface	Vapor Side of the Gibbs Surface	Gibbs Surface H ₂ O/CCl ₄	Organic Side of the Gibbs Surface
12D \rightarrow 0D (nonequilibrium)	0.05	0.07	0.04	0.09	0.04
12D \rightarrow 0D (equilibrium)	0.06	0.13	0.16	0.1	0.16
0D \rightarrow 12D (nonequilibrium)	0.2	0.6	1.4	0.6	5.9
0D \rightarrow 12D (equilibrium)	0.07	0.11	0.15	0.10	0.30

be present in the bulk of either liquid, corresponding to the relatively slow diffusion of finger-like water structures at the interface. In this case, marked deviations from a linear response were observed.

The model used in the previous two sections shows how charged groups maintain their hydration shell at aqueous interfaces and how that was used to understand rotational and vibrational relaxation. The same model can be used for solvation dynamics.⁵³⁷ We compute the solvation dynamics following the transition ($\mu = 0$) \rightarrow ($\mu = 12D$) and the reverse transition ($\mu = 12D$) \rightarrow ($\mu = 0$) of a diatomic solute held at different locations in the water liquid/vapor interface and in the water/CCl₄ interface. The equilibrium and nonequilibrium correlation functions both approximate a biexponential relaxation. Table 2 summarizes the average relaxation times in picoseconds.

The nonequilibrium solvation dynamics following the ($\mu = 12D$) \rightarrow ($\mu = 0$) transition are essentially independent of the solute's location. The very rapid subpicosecond relaxation is complete within a few hundred femtoseconds. The linear response approximation is satisfied in all locations except on the vapor side of the water liquid/vapor interface and on the organic side of the water/CCl₄ interface. The main reason for the deviation from linear response is the different contribution of the inertial component to the total relaxation, as the equilibrium relaxation is determined from the solvent fluctuations around the neutral solute.

Much more interesting and revealing is the reverse process: ($\mu = 0$) \rightarrow ($\mu = 12D$). The nonequilibrium solvation dynamics becomes much slower and sensitive to the location. The nonequilibrium relaxation in bulk water and at the water liquid/vapor interface gives $\tau(\text{bulk}) < \tau(\text{Gibbs}) < \tau(\text{above Gibbs})$. As previously discussed, the structure of the hydration shell around the large dipole at the interface is similar to that in the bulk. This structure is created from a very different solvent configuration when the solute suddenly acquires a 12D

dipole; this takes longer to form at the interface than in the bulk. In contrast, the equilibrium correlation function is computed from the energy fluctuations in the final $\mu = 12\text{D}$ state, and those fluctuations are similar in the three locations.

The nonequilibrium dynamics on the organic side of the water/ CCl_4 Gibbs surface are much slower than in all other locations. This is because the final equilibrium state requires significant perturbation to the water structure. This also explains why in this case a breakdown of linear response is observed.

Finally, it is interesting to note that the results at the Gibbs surface of the water/ CCl_4 interface are almost identical to those at the Gibbs surface of the water liquid/vapor interface for both transitions. This is consistent with previous simulations, showing that the polarity of these systems is very similar.⁵³⁶

SUMMARY

Because of the close connection between the three phenomena discussed in this section, it is useful to summarize here the main results. When comparing the bulk and the surface vibrational, rotational, and solvation dynamics of adsorbed solute molecules, two controlling structural motifs emerge: (i) the interface is a narrow, rough region broadened by density fluctuations (nanoscale capillaries) that may couple to solute modes; (ii) a charged solute at the interface tends to have a hydration shell that is similar in structure to the one in bulk water, the similarity of which depends on the solute size and charge. These two factors also provide a foundational understanding of surface effects on solute thermodynamics and spectroscopy. However, while they have been the subject of several largely consistent experimental and computational studies, many of the dynamical results presented in the last three sections await experimental confirmation. In particular, it would be interesting to confirm that the surface effect on vibrational lifetime is sensitive to the polarity of the solute and that the solvation dynamics following the creation of a large dipole on the organic side of the interface between water and a nonpolar liquid can be used to probe slow surface density fluctuations. Such experiments can add significantly to our understanding of the structure and dynamics of the interface. Extending the computations to larger dye molecules with anticipated large nonlinear responses would be useful in the search for systems that could be studied experimentally.

The tendency of solute molecules to keep their hydration shell, the roughness of the liquid surface and its dynamic fluctuations are not only important for understanding solute spectroscopy, thermodynamic, and relaxation phenomena, but also, as we show below, they play a major role in elucidating the surface effect on chemical reactivity.

REACTIVITY AT LIQUID INTERFACES

Introduction

Theoretical^{538–541} and experimental²²¹ studies of chemical reaction dynamics and thermodynamics in bulk liquids have demonstrated in recent years that one must take into account the molecular structure of the liquid to fully understand solvation and reactivity. The solvent is not to be viewed as simply a static medium but as playing an active role at the microscopic level. Our discussion thus far underscores the unique molecular character of the interface region: asymmetry in the intermolecular interactions, nonrandom molecular orientation, modifications in the hydrogen-bonding network, and other such structural features. We expect these unique molecular structure and dynamics to influence the rate and equilibrium of interfacial chemical reactions. One can also approach solvent effects on interfacial reactions at a continuum macroscopic level where the interface region is characterized by gradually changing properties such as density, viscosity, dielectric response, and other properties that are known to influence reactivity.

Computational studies of neat liquid surfaces are becoming a mature area of study, but investigation of chemical reaction thermodynamics and dynamics is much more limited. This is due, in part, to the scarcity of molecular-level experimental data. While some computational work focused on reactions that were also studied experimentally, most of the published computational work relied on simple model reactions to address these two important general questions:

- (a) How does the interface region affect the rate and the equilibrium of different types of reactions?
- (b) Can solvent effects on reactions at interfaces be understood by simply scaling bulk effects, or should it be treated in a unique manner?

Methods used to study reactivity in bulk liquids are relatively well developed and generally can be used without major modification to study reactions at interfaces. The computational approach typically involves these steps:^{538–541}

1. Define a reaction coordinate $X(r)$, which in general is a function of some (or even many) of the atomic positions in the systems. Examples include a torsional angle in a molecule for a conformational transition, a bond distance for a simple dissociation reaction, or, a function of many solvent atomic positions in the case of an electron transfer reaction. Keep in mind that in many cases the simple classical force fields described earlier in this chapter are inadequate for describing the proper dynamics of the system along the coordinate X . A quantum description at some level is likely needed

to account for the change in the electronic structure that is typically involved in a reaction.

2. Perform *equilibrium free energy calculations to determine the free energy profile $A(x)$ along the coordinate X* . This follows the methodology discussed earlier. The direct sampling of X , from which $A(x) = -\beta^{-1} \ln \langle \delta[X(\mathbf{r}) - x] \rangle$ can be determined, is rarely successful because a large free energy barrier can prevent efficient (or any!) sampling of phase space. Umbrella sampling with a biasing potential is therefore a standard “trick” to use. Knowledge of the free energy profile provides the activation free energy and thus an estimate of the rate constant from transition state theory (TST). The free energy difference between the reactants and products with proper accounts for the thermodynamic standard state allows for a computation of the equilibrium constant.
3. Perform *nonequilibrium trajectory calculations to explore possible dynamical contributions to the rate, energy flow, and mechanism*. The actual chemical reaction rate constant differs from the TST value because not every trajectory reaching the transition state will end up as products; the transmission coefficient gives the fraction of successful trajectories. Methods to calculate it^{538–541} can be used with no modification at liquid interfaces, an example of which will be discussed below. Besides determining the transmission coefficient, reactive trajectories, connecting reactants, and products provide information about the reaction mechanism and energy flow in the system.^{541–543}

Computational studies of chemical reactions dynamics at liquid/vapor and liquid/liquid interfaces to date include the following types of reactions: isomerization, photodissociation, acid dissociation, electron transfer, proton transfer, ion transfer, and nucleophilic substitution. These studies have been motivated by experimental observations and fundamental scientific interest in understanding how the unique surface properties affect chemical reactivity. Some of these studies have been reviewed.^{544,545} Here we present two examples selected to demonstrate the computational steps described above and their relation to the concepts developed in earlier sections. The focus is on contrasting the surface reactivity with that in the bulk and on examining surface effects in light of the knowledge about the structure and dynamics of neat interface and interfacial solvation, discussed earlier in the chapter.

Electron Transfer Reactions at Liquid/Liquid Interfaces

Electron transfer (ET) at the interface between two immiscible electrolyte solutions (IES) is important in electrochemistry,^{12,48,546,547} solar energy conversion, “artificial photosynthesis,”^{548,549} phase transfer catalysis, and is relevant to biological processes at membrane interfaces and in DNA environments so it is especially important to understand.⁵⁵⁰ The experimental study of ET reactions

at IES interfaces has a long history.¹² Until recently, measurements of those electron transfer rates involved mainly conventional electrochemical methods, where the interface is under external potential control and a steady state current versus voltage is measured.^{12,551} These measurements suffer from drawbacks, including an inability to distinguish clearly between electron and ion transfer, a narrow potential window, distortion due to the charging current, and the large resistivity of the organic phase. These drawbacks limit the number of experimental systems that can be studied, and thus very few reliable rate constants have been reported at interfaces.

There has been a recent surge in experimental activity due to the availability of new methods in which those drawbacks can be minimized or controlled. These methods include scanning electrochemical microscopy (SECM),^{552–560} thin-layer cyclic voltammetry,^{561,562} and spectroelectrochemical methods (some taking advantage of recent advances in nonlinear optics).^{563–578} In the SECM technique, one has the ability to widen the potential window and that increases significantly the range of the driving force (ΔG_{rxn}) for the ET reactions studied at the liquid/liquid interface. Because of that it has enabled the observation of the Marcus-inverted region (see below) and provided a reliable determination of the reorganization free energy.^{560,579–581}

Spectroelectrochemical methods have been used in recent years to study fast-photoinduced electron transfer at the liquid/liquid interface.^{566–570,582} Of particular importance is extending the idea of employing solvent (typically *N,N*-dimethylaniline or DMA) as an electron donor to the liquid/liquid interface.^{571,583–585} The advantage of this approach is that complications due to ion transfer across the interface and to diffusion are obviated. Several studies of ET between coumarin dyes and electron-donating solvents in micelles, reverse micelles, at the surface of proteins, and in nanocavities have demonstrated ultrafast electron transfer that is faster than solvation due to the close proximity of the redox pair. These experiments provided additional evidence for the existence of the Marcus-inverted region at liquid interfacial systems.^{572–578,586}

The basic theory of ET in bulk liquid and at liquid/metal interfaces is well-developed^{587–590} but applications of that theory to ET at IES were slow to be adopted due to insufficient knowledge about the molecular structure of the liquid/liquid interface and due to experimental difficulties. ET rate constants under steady state conditions are typically obtained from current/voltage measurements. A potential difference V is established across the interface, and the current I is measured. If the basic theory of electron transfer at the solution/metal interface⁵⁹¹ is applicable to the liquid/liquid interface, one then expects the following Butler–Volmer relation between the voltage and the current:

$$I = I_0 \left(e^{(1-\alpha)nF(V-V_{eq})/RT} - e^{anF(V-V_{eq})/RT} \right) \quad [55]$$

where T is the temperature, R is the gas constant, F is the Faraday constant, n is the number of electrons in the balanced half-reaction at the anode or the cathode, V_{eq} is determined from the Nernst equation ($V_{\text{eq}} = V_0 + \frac{RT}{nF} \ln \frac{a_{\text{O}}^s}{a_{\text{R}}^s}$, where V_0 is the standard potential and a_{O}^s , a_{R}^s are the activities of the oxidized and reduced agents at the interface), α is a constant called the transfer coefficient (see below), and I_0 is the so-called exchange current. The exchange current is the current that flows at equilibrium ($V = V_{\text{eq}}$) at the cathode (or the anode, they must be equal in magnitude and opposite in sign), and it is directly related to the heterogeneous rate constant k : $I_0 = nF[\text{O}]^{1-\alpha}[\text{R}]^{\alpha}k$, where $[\text{O}]$ and $[\text{R}]$ are the equilibrium concentrations. The key point is that the Butler–Volmer relation can be derived from the Marcus theory of electron transfer. This derivation⁵⁸⁷ shows that the transfer coefficient is given by $\alpha = 1/2 + \Delta G/2\lambda$, where ΔG is the reaction free energy, and λ is the reorganization free energy (see below).

Current voltage measurements of ET at IES sometimes conform to the Butler–Volmer equation and sometimes not.^{561,562} This is not surprising because some of the assumptions on which this equation is based may fail at the liquid/liquid interface. These assumptions include: (1) The potential drop across the interface is close to that imposed on the electrodes, or if not, a correction is included to properly account for the potential carried by the diffuse layers of ions at the interface; (2) The current is due to ET alone, and if not, a correction due to ion transfer must be included; (3) Marcus theory is valid.

The basic assumption of Marcus theory is that the solvent free energy functions controlling ET are paraboli with equal curvatures (linear response). On the basis of this, making an assumption about the structure of the interface, and using a continuum electrostatic expression for the activation free energy,^{546,592,593} Marcus derived expressions for the bimolecular rate constant of an ET at IES.^{594,595} To date, the computational work in this area has focused on testing the assumptions underlying the above theory. We briefly summarize Marcus theory to present the computational work.

Marcus Theory of ET at IES Interfaces

We consider the ET reaction $\text{DA} \rightarrow \text{D}^+\text{A}^-$ between an electron donor (D) and an electron acceptor (A) that are adsorbed at the interface between two immiscible liquids. For simplicity, we ignore the contribution of the vibrational modes of D and A because the contribution of these modes to the activation free energy is not expected to be modified significantly by the interface. At a given distance R between the reactants, the probability of an electron transfer depends on the overlap of the reactants' wave functions (electronic coupling) and on the probability that a solvent fluctuation will equalize the energy of the two diabatic states $|\text{DA}\rangle$ and $|\text{D}^+\text{A}^-\rangle$. For weak coupling, the rate constant for the electron transfer reaction is given by:^{593–595}

$$k_r = \kappa \nu V_r e^{-\beta \Delta G^\ddagger} \quad [56]$$

where κ is the Landau–Zener factor between the two diabatic electronic states,⁵⁹⁶ and ν is a “collision” frequency, which is determined from the equilibrium solvent fluctuations in the reactant state. V_r is the reaction volume, which accounts for all of the possible configurations of the reactant pair per unit area of the interface. For example, if one assumes that the two reactants are spherical (radii a_1 and a_2) and are restricted to being on opposite sides of a flat interface, then: $V_r = 2\pi(a_1 + a_2)(\delta R)^3$ and δR is a length scale for the distance-dependent electronic coupling between the two diabatic states.⁵⁹³

The activation energy ΔG^\ddagger is given by^{593–595}

$$\Delta G^\ddagger = W_r + \frac{(\lambda + \Delta G + W_p - W_r)^2}{4\lambda} \quad [57]$$

where ΔG is the reaction free energy, W_r is the reversible work required to bring the reactants from the bulk of each phase to the interface, $-W_p$ is the reversible work required to separate the products, and λ is the reorganization free energy. ΔG is controlled externally by varying the voltage across the interface. W_r and W_p may be estimated from experimental adsorption isotherms, or they can be calculated using continuum electrostatic models or by the MD or MC methods described earlier.

The key quantity, the reorganization free energy λ , is defined as the reversible work needed to change the equilibrium solvent configuration around the reactants to be that around the products at a fixed electronic state. It was first calculated analytically by Kharkats⁵⁹⁷ for the case of two reactants located at various positions along the line normal to the interface (modeled as a mathematically ideal plane separating the two bulk phases). Marcus generalized the calculations to include any orientation of the reactants relative to the interface normal.⁵⁹³ Kharkats and Benjamin⁵⁹⁸ investigated the case where the reactants may cross the interface, accounting for a mixed solvation shell at the interface. They show that the reorganization free energy is affected markedly by the possibility of the ions crossing the interface, and that this will have a significant effect on the rate.

To test this theory, Marcus estimated λ by using the rate constant of the half reaction at the solution/metal interface. This estimate and other assumptions gave reasonable agreement with the experimental rate constant for the reaction between the $\text{Fe}(\text{CN})_6^{4-/3-}$ couple in water and for the $\text{Lu}(\text{PC})_2^{+/2+}$ (hexacyanoferrate-lutetium biphthalocyanine) couple in DCE.^{593,594}

Microscopic Models

Marcus’s model assumes the validity of a linear response approximation and that a continuum electrostatic description of the interface is suitable for the purpose of calculating the activation free energy. Furthermore, to obtain expressions for the rate constant, the interface is assumed to be either a mathematically sharp plane or a broad homogeneous phase. Unfortunately, an insufficient

number of experimental data exist to test these assumptions. Thus, the main focus of using atomistic approaches to interfacial ET has been to gain insight into how important the molecular structure of the interface actually is for influencing the ET rate.

Key to the microscopic description of ET used in several MD simulations is a definition of the reaction coordinate. Because solvent fluctuations control the probability of electron transfer, this coordinate must be a function of solvent configuration. A useful one-dimensional definition, used extensively in simulations, is the energy gap when the system is in either of the two electronic states.^{599–602}

$$X(\mathbf{r}) = U_P(\mathbf{r}) - U_R(\mathbf{r}) \quad [58]$$

where U_R and U_P are the potential energies of the reactant state $\psi_R = |DA\rangle$ and the product state $\psi_P = |D^+A^- \rangle$, respectively, and \mathbf{r} represents the positions of all the atoms. It can be shown that this coordinate is equivalent (in some sense) to the solvent polarization coordinate used by Marcus to derive the continuum electrostatic expressions for the reorganization free energy.^{603,604} The probability $P(x)$ that $X(\mathbf{r})$ is equal to some value x is:

$$P_\nu(x) = \langle \delta[X(\mathbf{r}) - x] \rangle_\nu \quad [59]$$

where the ensemble average is over the reactant ($\nu = R$) or the product ($\nu = P$) state. The solvent free energy associated with solvent fluctuations in the state ν is given by

$$G_\nu(x) = -\beta^{-1} \ln P_\nu(x) \quad [60]$$

When the system is in the state ν , most fluctuations in the solvent coordinate are near the vicinity of its equilibrium value $x_\nu = \langle X(\mathbf{r}) \rangle_\nu$, so direct sampling of Eq. [59] will only provide the free energy for small fluctuations around the equilibrium. However, the reorganization free energy is the difference:

$$\lambda_R = G_R(x_P) - G_R(x_R) = -\beta^{-1} \ln \frac{P_R(x_P)}{P_R(x_R)} \quad [61]$$

with an equivalent expression for the product state. Because x_R and x_P are typically very different, an umbrella sampling procedure is required. One approach developed by King and Warshel⁶⁰⁰ is to simply consider a set of intermediate virtual electronic states, ν_m , $m = 1, 2, \dots$, and calculate the free energy function for each individual state. These functions are then “stitched” together to reconstruct the desired full functions G_R and G_P . If the different virtual electronic states correspond to a transfer of a fixed fraction of an electron, this procedure is equivalent to adding a biasing potential that is linear in the coordinate x .^{600,605}

At the transition state, $x = x^\#$, the energy of the two states is the same. This nonequilibrium state can be obtained from the intersection $G_R(x^\#) = G_P(x^\#)$.

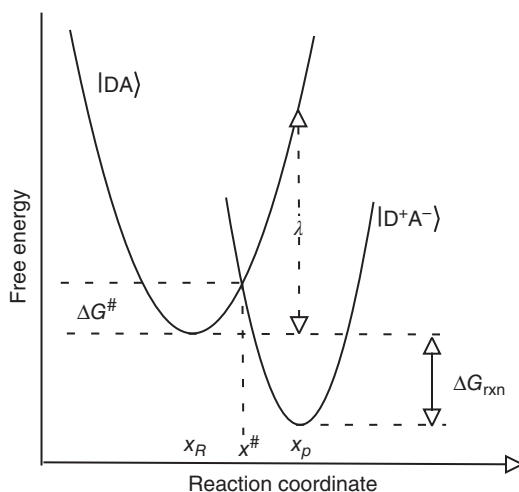


Figure 13 A schematic representation of the free energy functions involved in the thermally activated electron transfer reaction $DA \rightarrow D^+A^-$. See text for details.

Then, the activation free energy for the forward ET reaction is $\Delta G^\ddagger = G_R(x^\ddagger) - G_R(x_R)$. Figure 13 depicts the quantities discussed above.

Equation [57] for the activation free energy is based on the assumption that the solvent free energies $G_R(x)$ and $G_P(x)$ are paraboli with identical curvatures k :

$$G_R(x) = \frac{1}{2}k(x - x_R)^2; G_P(x) = \frac{1}{2}k(x - x_P)^2 + \Delta G \quad [62]$$

where ΔG is the reaction free energy. The parabolic assumption can be checked by an MD umbrella calculation of the full solvent free energy. This was done for ET reactions in bulk water,^{600,601} at the interface between two simple liquids,⁶⁰⁶ and at the water/self-assembled monolayer interface.⁶⁰⁷ Note that the solvent force constants k_v can be calculated directly from the fluctuations in the solvent coordinate in the two equilibrium states,⁶⁰² $k_v = 1/\beta\langle(x - x_v)^2\rangle_v$. If $k_R = k_P$, the assumption of a parabolic free energy can then be used to compute the activation free energy on the basis of simulations in the initial and final states alone. If the force constants are different, it is still possible to find the activation free energy approximately by an extrapolation procedure developed by Voth and coworkers.^{96,608}

The solvent free energies for an ET reaction between two charge transfer centers adsorbed at the water/1,2-dichloroethane interface were investigated by MD simulations.⁶⁰⁹ The charge centers were modeled as Lennard-Jones spheres with the parameters $\sigma = 5 \text{ \AA}$ and $\epsilon = 0.1 \text{ kcal/mol}$. In bulk water, the free energy curves calculated from the molecular dynamics simulations are approximately well described by paraboli. While the curvature of the free

energy function for the ion pair state D^+A^- (the constant k in Eq. [62]) is smaller than that for the neutral pair (DA state), the activation free energy predicted by the molecular dynamics results is almost identical to the one predicted by the quadratic approximation for the case of zero reaction free energy ($\Delta G = 0$), a region where most ET rate measurements are carried out. At the water/1,2-dichloroethane interface, the deviation between the molecular dynamics calculations and the linear response theory is even smaller. The reorganization free energy calculated from the continuum dielectric model⁵⁹³ using the MD-derived static dielectric constants of water ($\epsilon_0 = 82.5$) and DCE ($\epsilon_0 = 10$) and other geometrical parameters is $\lambda = 74$ kcal/mol compared to the MD value of 80 kcal/mol.⁶⁰⁹ This agreement, however, is due to an error cancellation: the water contribution to the electrostatic potential at the location of the charge transfer centers is underestimated by the continuum model (due to the neglect of the specific hydration structure), while the DCE potential is overestimated.^{532,610}

Other assumptions made in deriving the ET rate constant, such as the interface being flat and the inability of the ions to penetrate the interface, have also been investigated by molecular dynamics simulations. As discussed earlier in this chapter, the roughness of the interface and the ability of ions to cross the interface and be partially solvated by both liquids are features of the real system that simple continuum models cannot account for.

Finally, we note that fast electron transfer reactions in a polar environment may be strongly controlled by the rate at which solvent dipoles are able to reorient in response to the electron transfer. Thus solvent dynamics at the interface may be tightly coupled with the electron transfer. This is the case for photoinduced electron transfer reactions in which one of the reactants is photoexcited prior to the ET act itself. For example, Eisenthal and coworkers used SHG⁵⁷¹ (and more recently SFG⁶¹¹) to study the ultrafast excited state electron transfer at a water/organic liquid interface. In the SHG experiment, a 424 nm photon excites C314 adsorbed at the water/dimethylaniline (DMA) interface. The electron transfer from an interfacial DMA molecule to the excited state coumarin (C314*) was explored by measuring the resonant SHG signal produced from the C314 by a probe pulse. The fast signal change was attributed to the solvation dynamics of C314* on the subpicosecond timescale, followed by ET on a 14–16 ps timescale.

Nucleophilic Substitution Reactions and Phase Transfer Catalysis (PTC)

Many chemical reactions that take place at the interface between two immiscible liquids are coupled to reactant/product transfer processes, both to and from the bulk phases and across the interface. Sometimes, depending

on the reaction, these transfer processes complicate the theoretical and the experimental analysis, as is the case for coupled electron and ion transfer mentioned in the previous section. However, in other cases this coupling is the basis of the process being studied and cannot be avoided, as in Liquid-Liquid Phase Transfer Catalysis^{5,6,612–614} (LLPTC). This process is used widely in organic synthesis,⁶¹⁵ in pharmaceutical and agrochemical industries,⁵ in materials science,⁶¹⁶ and in “green” chemistry applications.⁶¹⁴ In LLPTC, a water-soluble reactant is transferred, with the aid of a phase transfer catalyst, from an aqueous phase into an organic phase, where it reacts with a water-insoluble reactant. Once complete, the catalyst, which is typically a quaternary ammonium cation, transfers the product to the aqueous phase, and the catalytic cycle repeats.

One of the most common reactions carried out under PTC conditions is nucleophilic substitution (S_N2). It is well known that the strong reactivity of anionic nucleophiles in gas phase S_N2 reactions is reduced markedly when the reaction is carried out in a polar protic solvent such as water.^{327,617–627} The condensed phase reactivity can be enhanced if the reaction is done in a low-polarity aprotic solvent, like chloroform, which can lower the barrier compared with that in bulk water significantly. A PT catalyst can transfer small nucleophiles such as F^- and Cl^- into the low-polarity solvents and enable the reaction.

Our earlier discussion on solute behavior at the liquid/liquid interface raises several fundamental questions about LLPTC. For example, how important is it to consider the hydration state of the nucleophilic ions for reactions carried out under PTC conditions? We already demonstrated that the transfer of small hydrophilic anions from water to an organic solvent is accompanied by a few water molecules.⁶ Experimental studies in bulk nonpolar solvents suggest that the hydration state of the anion strongly influences its nucleophilicity.^{628–630} Much theoretical support for this has also been provided from studies of S_N2 reactions in gas phase clusters^{631–633} and in bulk liquids.^{626,634} Another question revolves around the finding about the strong dependence of solvent polarity on the surface location and orientation. How would this affect the reactivity of an S_N2 reaction given its strong dependence on polarity?

To address these questions, molecular dynamics simulations were carried out for a simple benchmark symmetric S_N2 reaction, $Cl^- + CH_3Cl \rightarrow CH_3Cl + Cl^-$, at different locations of the water/chloroform interface.⁶³⁵ The reaction was modeled using the Empirical Valence Bond (EVB) approach.^{618,619,622,636} Briefly, EVB assumes the electronic state of the reactive system can be described using two orthonormal valence states, $\psi_1 = Cl^-CH_3-Cl$ and $\psi_2 = Cl-CH_3Cl^-$

$$\Psi = c_1\psi_1 + c_2\psi_2, \quad \langle \psi_i | \psi_j \rangle = \delta_{ij} \quad [63]$$

The total Hamiltonian is written as:

$$\hat{H} = \begin{pmatrix} H_{11}(\mathbf{r}_i, \mathbf{r}_d, \mathbf{r}_s) & H_{12}(r_1, r_2, \theta) \\ H_{12}(r_1, r_2, \theta) & H_{22}(\mathbf{r}_i, \mathbf{r}_d, \mathbf{r}_s) \end{pmatrix} \quad [64]$$

$$H_{11} = E_k + H_{11}^0(r_1, r_2, \theta) + U_{ss}(\mathbf{r}_s) + U_{si}(\mathbf{r}_s, \mathbf{r}_i) + U_{sd}(\mathbf{r}_s, \mathbf{r}_d) \quad [65]$$

where H_{11} is the diabatic Hamiltonian describing the system in the state ψ_1 . It includes E_k – the kinetic energy of all atoms; $H_{11}^0(r_1, r_2, \theta)$ – the gas phase interaction between the Cl^- ion and the CH_3Cl molecule; $U_{ss}(\mathbf{r}_s)$ – the individual solvents and the solvent–solvent potential energies; $U_{si}(\mathbf{r}_s, \mathbf{r}_i)$ – the solvent–ion potential energy; and $U_{sd}(\mathbf{r}_s, \mathbf{r}_d)$ – the solvent– CH_3Cl potential energy. In Eqs. [64] and [65], \mathbf{r}_i is the vector position of the Cl^- ion, \mathbf{r}_d is the vector position of the CH_3Cl atoms, and \mathbf{r}_s stands for the positions of all the solvent atoms. r_1 is the distance between the Cl^- ion and the carbon atom, r_2 is the C–Cl bond distance in CH_3Cl , and θ is the Cl^- – C–Cl angle. H_{22} is the diabatic Hamiltonian describing the system in the state ψ_2 , and due to the symmetry of the reaction, H_{22} has the same functional form as H_{11} but with the two chlorine atom labels interchanged.

The detailed functional forms and parameter values of all the potential energy terms in Eq. [65] can be found elsewhere.⁶³⁶ Here we note that the gas phase potential energy, $H_{11}^0(r_1, r_2, \theta)$, is a generalization to noncollinear geometries of the form suggested by Mathis et al.⁶²² It includes a Morse potential for the CH_3Cl bond, an exponential repulsive term for the interaction between the Cl^- ion and the CH_3 radical, and an ion-dipole term for combined short-range repulsion and long-range attractive interactions between the Cl^- ion and the CH_3Cl bond. These terms are obtained from a fit to the *ab initio* calculations of Tucker and Truhlar⁶³⁷ and to experimental data.⁶²² The generalization to nonlinear geometry is accomplished by making some of the parameters θ -dependent and adding a bending energy term with parameters determined by a best fit to the gas phase *ab initio* values of the energy, to the location of the transition state, and to the ion-dipole depth as a function of θ . $U_{ss}(\mathbf{r}_s)$, $U_{si}(\mathbf{r}_s, \mathbf{r}_i)$, and $U_{sd}(\mathbf{r}_s, \mathbf{r}_d)$ are all given by the sum of Lennard-Jones plus Coulomb interactions between every two sites on different molecules. The solvents' Lennard-Jones parameters, the intramolecular potential terms, and the corresponding intramolecular parameters can be found elsewhere.⁶³⁸ The water model was selected to be the model used previously to study the bulk and interfacial properties of water. The water and chloroform potentials used gives rise to a stable liquid/liquid interface with a surface tension of 25 ± 3 dynes/cm, in reasonable agreement with the experimental value of 26.6 dynes/cm. The off-diagonal electronic coupling term H_{12} in Eq. [64] is the one suggested by Hynes and coworkers.^{622,639}

$$H_{12} = -QS(r_1)S(r_2) \quad [66]$$

where $S(r)$ is the overlap integral for the sigma orbital formed from the carbon 2p and chlorine 3p atomic orbitals. $S(r)$ is determined using Slater-type orbitals and the approximation of Mulliken et al.,^{636,640} and $Q = 678.0$ kcal/mol is a parameter that is fitted to obtain the correct gas phase activation energy.

The diagonalization of Eq. [64] yields the electronic ground state adiabatic Hamiltonian as a function of all nuclear coordinates:

$$H_{\text{ad}} = \frac{1}{2}(H_{11} + H_{22}) - \frac{1}{2} \left[(H_{11} - H_{22})^2 + 4H_{12}^2 \right]^{1/2} \quad [67]$$

The classical trajectory calculations are carried out using this Hamiltonian. The reaction coordinate is defined by

$$\xi = r_1 - r_2 \quad [68]$$

so the reactants and products' states correspond to $\xi \ll 0$ and $\xi \gg 0$, respectively. The minimum energy path along ξ for the collinear geometry is shown in Figure 14. The total wavefunction (the values for c_1 and c_2 in Eq. [63]) shows that at the transition state in a vacuum (and on average in solution) each Cl atom in the reaction system carries a partial charge of $\delta \approx 0.5$: $[\text{Cl}^{-\delta} - \text{CH}_3 - \text{Cl}^{-\delta}]$. As ξ varies from $-\infty$ to $+\infty$, the charge on the nucleophile varies from -1 to the charge on the Cl atom in the isolated CH_3Cl molecule.

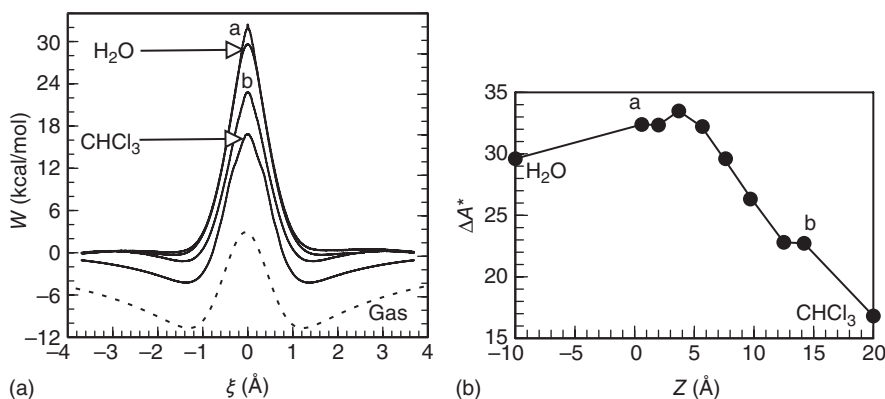


Figure 14 (a) The reaction free energy profile for the $\text{Cl}^- + \text{CH}_3\text{Cl}$ reaction at different locations of the water/chloroform interface. The lines labeled H_2O and CHCl_3 depict the profiles in the corresponding bulk solvents. The dotted line is the minimum energy path along the collinear geometry in the gas phase. (b) The activation free energy of this reaction versus all the locations studied along the interface normal. (Reprinted with permission from Ref. 479. Copyright 2010, American Chemical Society.)

The reaction free energy profile as a function of the reaction coordinate was calculated using umbrella sampling with overlapping windows and a biasing potential,²¹² as discussed earlier. The specific expressions used are:

$$W(\xi) = -\beta^{-1} \ln P(\xi) - U_b(\xi) \quad [69]$$

$$P(\xi) = \frac{\int \delta(r_1 - r_2 - \xi) \exp[-\beta(H_{ad} + U_b(\xi))] d\Gamma}{\int \exp[-\beta(H_{ad} + U_b(\xi))] d\Gamma} \quad [70]$$

A good choice for the biasing potential $U_b(\xi)$ (an analytic function of ξ chosen to approximate $-W(\xi)$ to accelerate the convergence of the ensemble average in Eq. [70]) was a Gaussian fit of the transition-state region of the free energy profile in bulk chloroform.⁶³⁶ The $W(\xi)$ were calculated at seven different interface locations by restricting the reactants' center of mass to slabs parallel to the liquid/liquid interface. Other details about the calculations are given in Ref. 635.

The results are shown in Figure 14. The top panel includes the free energy profiles at two interface locations, the gas phase potential energy along the minimum energy path for the collinear reaction geometry (dotted line) and the free energy profiles in bulk chloroform and in bulk water. The bottom panel shows the activation free energy barrier ΔA^* for all the locations. As the polarity of the bulk medium increases when going from the gas phase to bulk chloroform and bulk water, there is a significant increase in the activation free energy because the reactants and products experience a much greater lowering of their free energy than does the transition state. This, in turn, is because the separate reactants (or products) having the localized charge distribution on the chloride ion are much more favorably solvated than the delocalized charges of the transition state. Because the polarity of the interface region is expected to be somewhere between that of the two bulk phases,^{356,381} one would expect the activation free energy of the reaction at the different interface locations to fall in between the values in bulk water and in bulk chloroform. The bottom panel of Figure 14 shows the unexpected result that as the reactants' center of mass first moves past the Gibbs surface ($Z = 0$) toward the organic phase, the activation free energy becomes *greater* than in bulk water. As the reactants are moved deeper into the organic phase ($Z > 10 \text{ \AA}$), the activation free energy begins to decrease. While the barrier is lower than that in bulk water, at the largest Z studied, it is still higher than in bulk chloroform. This suggests that *for the reaction rate to be significantly larger than in bulk water, the reaction must take place deep in the organic phase.*

The fundamental reason for the relatively high barrier at or near the interface is the ability of the nucleophile to retain some number of water molecules

when it is in the vicinity of the interface and to keep the reactants hydrated. The resulting deformation of the interface is coupled strongly to the solute charge distribution and thus to the reaction coordinate. The behavior of the reaction far from the Gibbs surface is similar to that of the reaction $\text{Cl}^-(\text{H}_2\text{O})_n + \text{CH}_3\text{Cl}$ in bulk chloroform as a function of n . For example, at $Z = 15 \text{ \AA}$, $\Delta A^* = 22 \text{ kcal/mol}$, which is similar to $\Delta A^* = 21 \text{ kcal/mol}$ calculated for the reaction in bulk chloroform with $n = 1$. As n increases, the activation free energy increases monotonically to the value in bulk water.⁶⁴¹ Thus, the higher barrier of the reaction proximal to the Gibbs surface arises from a unique surface effect that can be traced to the orientational dependence of the reaction barrier.⁶³⁵ When the system is at or near the transition state ($\xi = 0$), the $\text{Cl}^{-0.5} - \text{CH}_3 - \text{Cl}^{-0.5}$ vector tends to lie parallel to the interface, but when the charge on the nucleophile is more or less fully developed (at $\xi \geq 0.3 \text{ \AA}$), the vector $\text{Cl}^- - \text{CH}_3 - \text{Cl}$ tends to lie perpendicular to the interface, with the Cl^- pointing toward the water phase. Thus, the transition state experiences an environment that is significantly less polar than the reactants, explaining the high barrier in the $Z < 5 \text{ \AA}$ region.

The activation free energy ΔA^* can be used to compute the TST approximation of the rate constant $k_{\text{TST}} = Ce^{-\beta\Delta A^*}$, where C is the preexponential factor. Because not every trajectory that reaches the transition state ends up as products, the actual rate is reduced by a factor κ (the transmission coefficient) as described earlier. The transmission coefficient can be calculated using the reactive flux correlation function method.^{540,541,642} Starting from an equilibrated ensemble of the solute molecules constrained to the transition state ($\xi = 0$), random velocities in the direction of the reaction coordinate are assigned from a flux-weighted Maxwell–Boltzmann distribution, and the constraint is released. The value of the reaction coordinate is followed dynamically until the solvent-induced recrossings of the transition state cease (in less than 0.1 ps). The normalized flux correlation function can be calculated using⁶⁴²

$$\kappa(t) = N_+^{-1} \sum_{i=1}^{N_+} \theta[\xi_i^+(t)] - N_-^{-1} \sum_{i=1}^{N_-} \theta[\xi_i^-(t)] \quad [71]$$

where ξ_i^\pm is the value of the reaction coordinate for the i th trajectory at time t , given that at $t = 0$, $d\xi/dt$ is positive (negative), N_+ (N_-) is the corresponding number of trajectories, and θ is the unit step function. $\kappa(t)$ converges to a fixed value when the recrossing of the transition state is complete. The total number of trajectories, $N = N_+ + N_-$, should be about 1000 for this procedure to converge.

The TST assumes no recrossings ($\kappa = 1$); it may fail due to interaction of the solute with the solvent molecules, causing the trajectory to recross the top of the barrier.^{539,540} Specifically, the solvent molecules that are equilibrated to the transition state charge distribution are not in the proper orientation necessary to solvate the product charge distribution. This might give rise to an additional

temporary solvent barrier preventing the system from proceeding directly to the product side and induce recrossings.⁶⁴³ The results of the calculations⁶³⁵ are consistent with the above picture. In general, however, deviation from TST values are not large, and the κ values fall in between the values in bulk water ($\kappa = 0.57$) and bulk chloroform ($\kappa = 0.76$) when the reaction takes place at the interface.

Given that the main role played by the phase transfer catalyst is to bring the hydrophilic reactant into contact with the hydrophobic reactant confined to the organic phase, an important question is: To what extent does the catalyst influence the reaction itself? Calculations were performed of the free energy profile of the benchmark $\text{Cl}^- + \text{CH}_3\text{Cl}$ S_N2 reaction at the water/chloroform interface in the presence of the phase transfer catalyst tetramethylammonium cation (TMA^+).⁶⁴⁴ TMA^+ moderately *increases* the barrier height of this reaction when it is associated with the Cl^- nucleophile. This is especially evident when the nucleophile is hydrated by a few water molecules. This suggests that the most effective role of the phase transfer catalyst is to bring the nucleophile deep into the organic phase with a minimal number of associated water molecules, followed by dissociation of the ion pair in the bulk organic phase before reaction.

CONCLUSIONS

Computational and experimental studies reveal that the interface between two fluid phases is a few nm thick highly anisotropic region, characterized by rapidly varying density, dielectric response, and molecular structure. It is also dynamic. Molecular motions are anisotropic, and density fluctuations create instantaneous structures that are significant on the narrow scale of the interface. These characteristics result in a marked influence on the solvation of solute molecules and on the equilibrium and rate of chemical reactions that take place in this region. In some cases, the effect of the interface region can be understood by the direct application of theories developed for understanding solvation and reactivity in bulk liquids. For example, by introducing interfacial solvent friction (in analogy with the bulk concept), one can understand the solvent effect on the rate of molecular reorientation and isomerization reactions. In other cases, one must take into account the unique interface characteristics to explain surface effects. For example, surface roughness at the interface between two immiscible liquids can have a significant effect on solvation dynamics and activation free energy for S_N2 reactions.

Despite the significant computational and experimental progress made in recent years, much more research is needed at both fronts to gain a molecular-level understanding of structure, thermodynamics, and dynamics at liquid interfaces. In particular, molecular-level, time-resolved experimental studies of solvation, relaxation, and reactions at liquid interfaces are needed.

At the theoretical level, simulations are needed of systems with more realistic potentials and of quantities that can be directly compared with experimental observations (such as from electronic sum frequency), while pushing the limit of system size and timescale. The development of multiscale theoretical models combining simple continuum models with some microscopic structure of the interface would also be desirable. Progress in these areas will advance our fundamental understanding of liquid interfacial phenomena while providing support for technological development in the areas of energy storage, catalysis, and the environment.

ACKNOWLEDGMENTS

This work was supported by the National Science Foundation (most recently by grant CHE-0809164). I would like to thank my collaborators: Daniel Rose, Karl Schweighofer, David Michael, Ilya Chorniy, John Viecele Nicholas Winter, and Katherine Nelson.

REFERENCES

1. J. O. M. Bockris and A. Gonzalez-Martin, in *Spectroscopic and Diffraction Techniques in Interfacial Electrochemistry*, C. Gutierrez and C. Melendres (Eds.), Kluwer Academic Publishers, Dordrecht, 1990, p. 1, The Advancing Frontier in the Knowledge of the Structure of the Interphases.
2. A. J. Bard and L. R. Faulkner, *Electrochemical Methods: Fundamentals and Applications*, New York, Wiley, 1980.
3. M. Cox, M. Hidalgo, and M. Valiente, *Solvent Extraction for the 21st Century*, London, SCI, 2001.
4. H. Watarai, N. Teramae, and T. Sawada, *Interfacial Nanochemistry: Molecular Science and Engineering at Liquid-Liquid Interfaces*, Kluwer Academic/Plenum, New York, 2005.
5. C. M. Starks, C. L. Liotta, and M. Halpern, *Phase Transfer Catalysis*, New York, Chapman & Hall, 1994.
6. A. G. Volkov, *Interfacial Catalysis*, New York, Marcel Dekker, 2003.
7. K. Arai, M. Ohsawa, F. Kusu, and K. Takamura, *Bioelectrochemistry and Bioenergetics*, **31**, 65 (1993). Drug Ion Transfer Across an Oil–Water Interface and Pharmacological Activity.
8. R. B. Gennis, *Biomembranes*, Springer, New York, 1989.
9. R. W. Johnson and G. E. Gordon, *The Chemistry of Acid Rain: Sources and Atmospheric Processes*, ACS Symposium Series, Washington, 1987.
10. B. J. Finlayson-Pitts, *Chem. Rev.*, **103**, 4801 (2003). The Tropospheric Chemistry of Sea Salt: A Molecular-Level View of the Chemistry of NaCl and NaBr.
11. A. W. Adamson, *Physical Chemistry of Surfaces*, Fifth edition, Wiley, New York, 1990.
12. H. H. Girault and D. J. Schiffrin, in *Electroanalytical Chemistry*, A. J. Bard (Ed.), Dekker, New York, 1989, p. 1, Electrochemistry of Liquid-Liquid Interfaces.
13. Y. R. Shen, *The Principles of Nonlinear Optics*, New York, Wiley, 1984.
14. Y. R. Shen, *Annu. Rev. Phys. Chem.*, **40**, 327 (1989). Optical 2nd Harmonic-Generation at Interfaces.
15. Y. R. Shen, *Nature*, **337**, 519 (1989). Surface Properties Probed by 2nd Harmonic and Sum Frequency Generation.

16. K. B. Eisenthal, *Annu. Rev. Phys. Chem.*, **43**, 627 (1992). Equilibrium and Dynamic Processes at Interfaces by Second Harmonic and Sum Frequency Generation.
17. K. B. Eisenthal, *Chem. Rev.*, **96**, 1343 (1996). Liquid Interfaces by Second Harmonic and Sum-Frequency Spectroscopy.
18. G. L. Richmond, *Chem. Rev.*, **102**, 2693 (2002). Molecular Bonding and Interactions at Aqueous Surfaces as Probed by Vibrational Sum Frequency Spectroscopy.
19. S. G. Grubb, M. W. Kim, T. Raising, and Y. R. Shen, *Langmuir*, **4**, 452 (1988). Orientation of Molecular Monolayers at the Liquid-Liquid Interface as Studied by Optical Second Harmonic Generation.
20. R. M. Corn and D. A. Higgins, *Chem. Rev.*, **94**, 107 (1994). Optical Second Harmonic Generation as a Probe of Surface Chemistry.
21. P. F. Brevet and H. H. Girault, in *Liquid-Liquid Interfaces*, A. G. Volkov and D. W. Deamer (Eds.), CRC Press, Boca Raton, 1996, p. 103, Second Harmonic Generation at Liquid/Liquid Interfaces.
22. G. L. Richmond, *Annu. Rev. Phys. Chem.*, **52**, 257 (2001). Structure and Bonding of Molecules at Aqueous Surfaces.
23. W. H. Steel and R. A. Walker, *Nature*, **424**, 296 (2003). Measuring Dipolar Width across Liquid-Liquid Interfaces with 'Molecular Rulers'.
24. M. A. Mendez, R. Partovi-Nia, I. Hatay, B. Su, P. Y. Ge, A. Olaya, N. Younan, M. Hojeij, and H. H. Girault, *Phys. Chem. Chem. Phys.*, **12**, 15163 (2010). Molecular Electrocatalysis at Soft Interfaces.
25. S. Ong, X. Zhao, and K. B. Eisenthal, *Chem. Phys. Lett.*, **191**, 327 (1992). Polarization of Water Molecules at a Charged Interface: Second Harmonic Studies of the Silica/Water Interface.
26. P. R. Fischer, J. L. Daschbach, and G. L. Richmond, *Chem. Phys. Lett.*, **218**, 200 (1994). Surface Second Harmonic Studies of Si(111)/Electrolyte and Si(111)/SiO₂/Electrolyte Interfaces.
27. K. B. Eisenthal, *Chem. Rev.*, **106**, 1462 (2006). Second Harmonic Spectroscopy of Aqueous Nano- and Microparticle Interfaces.
28. F. M. Geiger, *Annu. Rev. Phys. Chem.*, **60**, 61 (2009). Second Harmonic Generation, Sum Frequency Generation, and $\chi^{(3)}$: Dissecting Environmental Interfaces with a Nonlinear Optical Swiss Army Knife.
29. M. B. Pomfret, J. C. Owrutsky, and R. A. Walker, *Ann. Rev. Anal. Chem.*, **3**, 151 (2010). In Situ Optical Studies of Solid-Oxide Fuel Cells.
30. A. Lewis, A. Khatchatourians, M. Treinin, Z. P. Chen, G. Peleg, N. Friedman, O. Bouevitch, Z. Rothman, L. Loew, and M. Sheres, *Elegans. Chem. Phys.*, **245**, 133 (1999). Second-Harmonic Generation of Biological Interfaces: Probing the Membrane Protein Bacteriorhodopsin and Imaging Membrane Potential around GFP Molecules at Specific Sites in Neuronal Cells of C.
31. J. S. Salafsky, *Phys. Chem. Chem. Phys.*, **9**, 5704 (2007). Second-Harmonic Generation for Studying Structural Motion of Biological Molecules in Real Time and Space.
32. D. Beaglehole, in *Fluid Interfacial Phenomena*, C. A. Croxton (Ed.), Wiley, New York, 1986, p. 523, Experimental Studies of Liquid Interfaces.
33. P. S. Pershan, *Faraday Discuss. Chem. Soc.*, **89**, 231 (1990). Structure of Surfaces and Interfaces as Studied Using Synchrotron Radiation: Liquid Surfaces.
34. D. K. Schwartz, M. L. Schlossman, E. H. Kawamoto, J. G. Kellogg, P. S. Pershan, and B. M. Ocko, *Phys. Rev. A*, **41**, 5687 (1990). Thermal Diffuse X-Ray-Scattering of the Water-Vapor Interface.
35. K. Yasumoto, N. Hirota, and M. Terazima, *Phys. Rev. B*, **60**, 9100 (1999). Surface and Molecular Dynamics at Gas-liquid Interfaces Probed by Interface-Sensitive Forced Light Scattering in the Time Domain.
36. M. G. Munoz, M. Encinar, L. J. Bonales, F. Ortega, F. Monroy, and R. G. Rubio, *J. Phys. Chem. B*, **109**, 4694 (2005). Surface Light-Scattering at the Air-Liquid Interface: From Newtonian to Viscoelastic Polymer Solutions.

37. J. Als-Nielsen, *Physica*, **140A**, 376 (1986). Synchrotron X-Ray Studies of Liquid–Vapor Interfaces.
38. M. K. Sanyal, S. K. Sinha, K. G. Huang, and B. M. Ocko, *Phys. Rev. Lett.*, **66**, 628 (1991). X-Ray Scattering Study of Capillary-Wave Fluctuations at a Liquid Surface.
39. L. T. Lee, D. Langevin, and B. Farnoux, *Phys. Rev. Lett.*, **67**, 2678 (1991). Neutron Reflectivity of an Oil–Water Interface.
40. R. A. Cowley, in *Equilibrium Structure and Properties of Surfaces and Interfaces*, A. Gonis and G. M. Stocks (Eds.), Plenum, New York, 1992, p. 1, X-Ray Scattering from Surfaces and Interfaces.
41. P. S. Pershan, *Physica A*, **231**, 111 (1996). Liquid Surface Order: X-Ray Reflectivity.
42. D. M. Mitrinovic, Z. Zhang, S. M. Williams, Z. Huang, and M. L. Schlossman, *J. Phys. Chem. B*, **103**, 1779 (1999). X-Ray Reflectivity Study of the Water–Hexane Interface.
43. M. L. Schlossman, *Curr. Opin. Coll. Interf. Sci.*, **7**, 235 (2002). Liquid–Liquid Interfaces: Studied by X-Ray and Neutron Scattering.
44. G. Luo, S. Malkova, S. V. Pingali, D. G. Schultz, B. Lin, M. Meron, T. J. Graber, J. Gebhardt, P. Vanysek, and M. L. Schlossman, *Faraday Discuss*, **129**, 23 (2005). X-Ray Studies of the Interface between Two Polar Liquids: Neat and with Electrolytes.
45. M. E. Saecker, S. T. Govoni, D. V. Kowalski, M. E. King, and G. M. Nathanson, *Science*, **252**, 1421 (1991). Molecular Beam Scattering from Liquid Surfaces.
46. M. J. Wirth and J. D. Burbage, *J. Phys. Chem.*, **96**, 9022 (1992). Reorientation of Acridine Orange at Liquid Alkane Water Interfaces.
47. J. M. Kovaleski and M. J. Wirth, *J. Phys. Chem.*, **99**, 4091 (1995). Lateral Diffusion of Acridine Orange at Liquid Hydrocarbon/Water Interfaces.
48. A. J. Bard and M. V. Mirkin, *Scanning Electrochemical Microscope*, New York, Marcel Dekker, 2001.
49. F. O. Laforge, P. Sun, and M. V. Mirkin, *Adv. Chem. Phys.*, **139**, 177 (2008). Physicochemical Applications of Scanning Electrochemical Microscopy.
50. R. P. Sperline and H. Freiser, *Langmuir*, **6**, 344 (1990). Adsorption at the Liquid–Liquid Interface Analyzed by in Situ Infrared Attenuated Total Reflection Spectroscopy.
51. A. B. Horn and J. Sully, *J. Chem. Soc. Faraday Trans.*, **93**, 2741 (1997). Reaction and Diffusion in Heterogeneous Atmospheric Chemistry Studied by Attenuated Total Internal Reflection IR Spectroscopy.
52. K. R. Wilson, B. S. Rude, T. Catalano, R. D. Schaller, J. G. Tobin, D. T. Co, and R. J. Saykally, *J. Phys. Chem. B*, **105**, 3346 (2001). X-Ray Spectroscopy of Liquid Water Microjets.
53. K. R. Wilson, R. D. Schaller, D. T. Co, R. J. Saykally, B. S. Rude, T. Catalano, and J. D. Bozek, *J. Chem. Phys.*, **117**, 7738 (2002). Surface Relaxation in Liquid Water and Methanol Studied by X-Ray Absorption Spectroscopy.
54. C. A. Croxton, *Statistical Mechanics of the Liquid Surface*, New York, Wiley, 1980.
55. J. S. Rowlinson and B. Widom, *Molecular Theory of Capillarity*, Oxford, Clarendon, 1982.
56. J. K. Percus and G. O. Williams, in *Fluid Interfacial Phenomena*, C. A. Croxton (Ed.), Wiley, New York, 1986, p. 1, The Intrinsic Interface.
57. D. Henderson, *Fundamentals of Inhomogeneous Fluids*, New York, Marcel Dekker, 1992.
58. A. Kovalenko and F. Hirata, in *Interfacial Nanochemistry: Molecular Science and Engineering at Liquid–Liquid Interfaces*, H. Watarai, N. Teramae, and T. Sawada (Eds.), Kluwer Academic/Plenum, New York, 2005, p. 97, A Molecular Theory of Solutions at Liquid Interfaces.
59. J. C. Shelley and D. R. Berard, in *Reviews in Computational Chemistry*, K. B. Lipkowitz and D. B. Boyd (Eds.), VCH, New York, 1998, Vol. 12, p. 137, Computer Simulation of Water Physisorption at Metal–Water Interfaces.

60. M. Schoen and S. H. L. Klapp, in *Reviews in Computational Chemistry*, K. B. Lipkowitz and D. B. Boyd (Eds.), 2007, Vol. 24, p. 1, Nanoconfined Fluids: Soft Matter between Two and Three Dimensions.
61. M. P. Allen and D. J. Tildesley, *Computer Simulation of Liquids*, Clarendon, Oxford, 1987.
62. A. R. Leach, *Molecular Modeling: Principles and Applications*, 2nd edition, Pearson, New York, 2001.
63. D. Frenkel and B. Smit, *Understanding Molecular Simulation: From Algorithms to Applications*, 2nd edition, Academic Press, San Diego, 2002.
64. D. C. Rapaport, *The Art of Molecular Dynamics Simulations*, 2nd edition, Cambridge University Press, Cambridge, 2004.
65. D. B. Boyd, in *Reviews in Computational Chemistry*, K. B. Lipkowitz and D. B. Boyd (Eds.), Wiley-VCH, New York, 1997, Vol. 11, p. 373, Appendix: Compendium of Software and Internet Tools for Computational Chemistry.
66. S. Nosé, *J. Phys. Condens. Matter*, 2, SA115 (1991). Constant-Temperature Molecular Dynamics.
67. U. Burkert and N. L. Allinger, *Molecular Mechanics*, Washington, ACS, 1982.
68. U. Dinur and A. T. Hagler, in *Reviews in Computational Chemistry*, K. B. Lipkowitz and D. B. Boyd (Eds.), Wiley-VCH, New York, 1991, Vol. 2, p. 99, New Approaches to Empirical Force Fields.
69. M. Jalaie and K. B. Lipkowitz, in *Reviews in Computational Chemistry*, K. B. Lipkowitz and D. B. Boyd (Eds.), Wiley-VCH, New York, 2000, Vol. 14, p. 441, Appendix: Published Force Field Parameters for Molecular Mechanics, Molecular Dynamics, and Monte Carlo Simulations.
70. W. D. Cornell, P. Cieplak, C. I. Bayly, I. R. Gould, K. M. Merz, D. M. Ferguson, D. C. Spellmeyer, T. Fox, J. W. Caldwell, and P. A. Kollman, *J. Am. Chem. Soc.*, 117, 5179 (1996). A Second Generation Force Field for the Simulation of Proteins, Nucleic Acids, and Organic Molecules.
71. J.-P. Hansen and I. R. McDonald, *Theory of Simple Liquids*, 2nd edition, Academic, London, 1986, p. 179.
72. A. R. Vanbuuren, S. J. Marrink, and H. J. C. Berendsen, *J. Phys. Chem.*, 97, 9206 (1993). A Molecular Dynamics Study of the Decane Water Interface.
73. M. Hayoun, M. Meyer, and M. Mareschal, in *Chemical Reactivity in Liquids*, G. Ciccotti and P. Turq (Eds.), Plenum, New York, 1987, p. 279, Molecular Dynamics Simulation of a Liquid-Liquid Interface.
74. A. W. Hill and I. Benjamin, *J. Phys. Chem. B*, 108, 15443 (2004). Influence of Surface Tension on Adsorbate Molecular Rotation at Liquid/Liquid Interfaces.
75. R. J. Sadus, *Molecular Simulation of Fluids: Theory, Algorithms and Object-Orientation*, Elsevier, Amsterdam, 1999.
76. J. A. Barker, *Mol. Phys.*, 80, 815 (1993). Surface Tension and Atomic Interactions in Simple Liquids.
77. P. A. Pieniazek, C. J. Tainter, and J. L. Skinner, *J. Am. Chem. Soc.*, 133, 10360 (2011). Surface of Liquid Water: Three-Body Interactions and Vibrational Sum-Frequency Spectroscopy.
78. R. D. Levine, *Molecular Reaction Dynamics*, Cambridge University Press, Cambridge, UK, 2005.
79. B. J. Alder and E. L. Pollock, *Ann. Rev. Phys. Chem.*, 32, 311 (1981). Simulation of Polar and Polarizable Fluids.
80. M. Sprik and M. L. Klein, *J. Chem. Phys.*, 89, 7556 (1988). A Polarizable Model for Water Using Distributed Charge Sites.
81. Y. C. Chen, J. Lebowitz, and P. Nielaba, *J. Chem. Phys.*, 91, 340 (1989). Line Shifts and Broadenings in Polarizable Liquids.
82. P. Ahlstrom, A. Wallqvist, S. Engstrom, and B. Jonsson, *Mol. Phys.*, 68, 563 (1989). A Molecular Dynamics Study of Polarizable Water.

83. J. Caldwell, L. X. Dang, and P. A. Kollman, *J. Am. Chem. Soc.*, **112**, 9144 (1990). Implementation of Nonadditive Intermolecular Potentials by Use of Molecular-Dynamics - Development of a Water-Water Potential and Water Ion Cluster Interactions.
84. A. Wallqvist, *Chem. Phys. Lett.*, **165**, 437 (1990). Polarizable Water at a Hydrophobic Wall.
85. A. Wallqvist, *Chem. Phys.*, **148**, 439 (1990). Incorporating Intramolecular Degrees of Freedom in Simulations of Polarizable Liquid Water.
86. K. Motakabbir and M. Berkowitz, *Chem. Phys. Lett.*, **176**, 61 (1991). Liquid Vapor Interface of TIP4P Water: Comparison between a Polarizable and a Nonpolarizable Model.
87. L. X. Dang, J. E. Rice, J. Caldwell, and P. A. Kollman, *J. Am. Chem. Soc.*, **113**, 2481 (1991). Ion Solvation in Polarizable Water- Molecular Dynamics Simulations.
88. L. X. Dang, *J. Chem. Phys.*, **96**, 6970 (1992). Development of Nonadditive Intermolecular Potentials Using Molecular-Dynamics - Solvation of Li^+ and F^- Ions in Polarizable Water.
89. O. A. Karim, *J. Chem. Phys.*, **96**, 9237 (1992). Potential of Mean Force for an Aqueous Chloride Ion Pair - Simulation with a Polarizable Model.
90. G. Corongiu and E. Clementi, *J. Chem. Phys.*, **98**, 4984 (1993). Molecular-Dynamics Simulations with a Flexible and Polarizable Potential - Density of States for Liquid Water at Different Temperatures.
91. D. E. Smith and L. X. Dang, *J. Chem. Phys.*, **100**, 3757 (1994). Computer Simulations of NaCl Association in Polarizable Water.
92. J. S. Bader and B. J. Berne, *J. Chem. Phys.*, **104**, 1293 (1996). Solvation Energies and Electronic Spectra in Polar, Polarizable Media: Simulation Tests of Dielectric Continuum Theory.
93. T. M. Chang and L. X. Dang, *J. Chem. Phys.*, **104**, 6772 (1996). Molecular Dynamics Simulations of $\text{CCl}_4\text{-H}_2\text{O}$ Liquid-Liquid Interface with Polarizable Potential Models.
94. C. Tsun-Mei, L. X. Dang, and K. A. Peterson, *J. Phys. Chem. B*, **101**, 3413 (1997). Computer Simulation of Chloroform with a Polarizable Potential Model.
95. P. Jungwirth and D. J. Tobias, *J. Phys. Chem. A*, **106**, 379 (2002). Chloride Anion on Aqueous Clusters, at the Air-Water Interface, and in Liquid Water: Solvent Effects on Cl^- Polarizability.
96. D. W. Small, D. V. Matyushov, and G. A. Voth, *J. Am. Chem. Soc.*, **125**, 7470 (2003). The Theory of Electron Transfer Reactions: What May Be Missing?
97. S. W. Rick and S. J. Stuart, in *Reviews in Computational Chemistry*, K. B. Lipkowitz and D. B. Boyd (Eds.), Wiley-VCH, Hoboken, NJ, 2002, Vol. **18**, p. 89, Potentials and Algorithms for Incorporating Polarizability in Computer Simulations.
98. G. Ciccotti and J. P. Ryckaert, *Computer Physics Reports*, **4**, 345 (1986). Molecular Dynamics Simulation of Rigid Molecules.
99. A. Wallqvist and R. D. Mountain, in *Reviews in Computational Chemistry*, K. B. Lipkowitz and D. B. Boyd (Eds.), Wiley-VCH, New York, 1999, Vol. **13**, p. 183, Molecular Models of Water: Derivation and Description.
100. A. Trokhymchuk and J. Alejandre, *J. Chem. Phys.*, **111**, 8510 (1999). Computer Simulations of Liquid/Vapor Interface in Lennard-Jones Fluids: Some Questions and Answers.
101. J. Janacek, *J. Phys. Chem. B*, **110**, 6264 (2006). Long Range Corrections in Inhomogeneous Simulations.
102. P. Grosfils and J. F. Lutsko, *J. Chem. Phys.*, **130** (2009). Dependence of the Liquid-Vapor Surface Tension on the Range of Interaction: A Test of the Law of Corresponding States.
103. P. Auffinger and D. L. Beveridge, *Chem. Phys. Lett.*, **234**, 413 (1995). A Simple Test for Evaluating the Truncation Effects in Simulations of Systems Involving Charged Groups.
104. C. Sagui and T. A. Darden, *Annu. Rev. Biophys. Biomol. Struct.*, **28**, 155 (1999). Molecular Dynamics Simulations of Biomolecules: Long-Range Electrostatic Effects.
105. P. Ewald, *Ann. Phys.*, **64**, 253 (1921). Die Berechnung Optischer Und Elektrostatischer Gitterpotentiale.

106. S. W. d. Leeuw, J. W. Perram, and E. R. Smith, *Proc. Roy. Soc. London. Series A, Mathematical and Physical Sciences*, **373**, 27 (1980). Simulation of Electrostatic Systems in Periodic Boundary Conditions.
107. T. Darden, D. York, and L. Pedersen, *J. Chem. Phys.*, **98**, 10089 (1993). Particle Mesh Ewald – an $N \log(N)$ Method for Ewald Sums in Large Systems.
108. U. Essmann, L. Perera, M. L. Berkowitz, T. Darden, H. Lee, and L. G. Pedersen, *J. Chem. Phys.*, **103**, 8577 (1995). A Smooth Particle Mesh Ewald Method.
109. A. Y. Toukmaji and J. A. Board, *Comput. Phys. Commun.*, **95**, 73 (1996). Ewald Summation Techniques in Perspective: A Survey.
110. M. Deserno and C. Holm, *J. Chem. Phys.*, **109**, 7678 (1998). How to Mesh up Ewald Sums. I. A Theoretical and Numerical Comparison of Various Particle Mesh Routines.
111. M. Deserno and C. Holm, *J. Chem. Phys.*, **109**, 7694 (1998). How to Mesh up Ewald Sums. II. An Accurate Error Estimate for the Particle-Particle-Particle-Mesh Algorithm.
112. A. Brodka and A. Grzybowski, *J. Chem. Phys.*, **117**, 8208 (2002). Electrostatic Interactions in Computer Simulations of a Three-Dimensional System Periodic in Two Directions: Ewald-Type Summation.
113. I. C. Yeh and M. L. Berkowitz, *J. Chem. Phys.*, **111**, 3155 (1999). Ewald Summation for Systems with Slab Geometry.
114. M. Kawata and U. Nagashima, *Chem. Phys. Lett.*, **340**, 165 (2001). Particle Mesh Ewald Method for Three-Dimensional Systems with Two-Dimensional Periodicity.
115. D. Lindbo and A. K. Tornberg, *J. Chem. Phys.*, **136** (2012). Fast and Spectrally Accurate Ewald Summation for 2-Periodic Electrostatic Systems.
116. D. Zahn, B. Schilling, and S. M. Kast, *J. Phys. Chem. B*, **106**, 10725 (2002). Enhancement of the Wolf Damped Coulomb Potential: Static, Dynamic, and Dielectric Properties of Liquid Water from Molecular Simulation.
117. D. Wolf, P. Keblinski, S. R. Phillpot, and J. Eggebrecht, *J. Chem. Phys.*, **110**, 8254 (1999). Exact Method for the Simulation of Coulombic Systems by Spherically Truncated, Pairwise R^{-1} Summation.
118. S. Kale and J. Herzfeld, *J. Chem. Theory Comput.*, **7**, 3620 (2011). Pairwise Long-Range Compensation for Strongly Ionic Systems.
119. K. Z. Takahashi, T. Narumi, and K. Yasuoka, *J. Chem. Phys.*, **134** (2011). Cutoff Radius Effect of the Isotropic Periodic Sum and Wolf Method in Liquid–Vapor Interfaces of Water.
120. H. C. Andersen, *J. Chem. Phys.*, **72**, 2384 (1980). Molecular Dynamics Simulation at Constant Pressure and/or Temperature.
121. G. J. Martyna, D. J. Tobias, and M. L. Klein, *J. Chem. Phys.*, **101**, 4177 (1994). Constant-Pressure Molecular-Dynamics Algorithms.
122. Y. Zhang, S. E. Feller, B. R. Brooks, and R. W. Pastor, *J. Chem. Phys.*, **103**, 10252 (1995). Computer Simulation of Liquid/Liquid Interfaces. 1. Theory and Application to Octane/Water.
123. J. P. Valleau and G. M. Torrie, in *Statistical Mechanics, Part A: Equilibrium Techniques*, B. J. Berne (Ed.), Plenum, New York, 1977, A Guide to Monte Carlo for Statistical Mechanics. 2. Byways.
124. K. S. Liu, *J. Chem. Phys.*, **60**, 4226 (1974). Phase Separation of Lennard-Jones Systems - Film in Equilibrium with Vapor.
125. P. Linse, *J. Chem. Phys.*, **86**, 4177 (1987). Monte Carlo Simulation of Liquid-Liquid Benzene-Water Interface.
126. A. Z. Panagiotopoulos, *Mol. Phys.*, **61**, 813 (1987). Direct Determination of Phase Coexistence Properties of Fluids by Monte-Carlo Simulation in a New Ensemble.
127. L. X. Dang, T. M. Chang, and A. Z. Panagiotopoulos, *J. Chem. Phys.*, **117**, 3522 (2002). Gibbs Ensemble Monte Carlo Simulations of Coexistence Properties of a Polarizable Potential Model of Water.

128. D. M. Heyes and J. H. R. Clarke, *J. Chem. Soc.-Faraday Trans. II*, **75**, 1240 (1979). Molecular-Dynamics Model of the Vapor–Liquid Interface of Molten Potassium-Chloride.
129. B. Smit, *Phys. Rev. A*, **37**, 3431 (1988). Molecular Dynamics Simulation of Amphiphilic Molecules at a Liquid-Liquid Interface.
130. M. Meyer, M. Mareschal, and M. Hayoun, *J. Chem. Phys.*, **89**, 1067 (1988). Computer Modeling of a Liquid-Liquid Interface.
131. H. Watanabe, N. Ito, and C.-K. Hu, *J. Chem. Phys.*, **136**, 204102 (2012). Phase Diagram and Universality of the Lennard-Jones Gas–Liquid System.
132. R. S. Taylor, L. X. Dang, and B. C. Garrett, *J. Phys. Chem. B*, **100**, 11720 (1996). Molecular Dynamics Simulations of the Liquid/Vapor Interface of SPC/E Water.
133. L. B. Pártay, G. Hantal, P. Jedlovský, A. Vincze, and G. Horvai, *J. Comput. Chem.*, **29**, 945 (2008). A New Method for Determining the Interfacial Molecules and Characterizing the Surface Roughness in Computer Simulations. Application to the Liquid–Vapor Interface of Water.
134. F. Biscay, A. Ghoufi, V. Lachet, and P. Malfreyt, *J. Phys. Chem. C*, **115**, 8670 (2011). Prediction of the Surface Tension of the Liquid–Vapor Interface of Alcohols from Monte Carlo Simulations.
135. I. Benjamin, *J. Chem. Phys.*, **97**, 1432 (1992). Theoretical Study of the Water/1,2-Dichloroethane Interface: Structure, Dynamics and Conformational Equilibria at the Liquid-Liquid Interface.
136. D. Michael and I. Benjamin, *J. Phys. Chem.*, **99**, 1530 (1995). Solute Orientational Dynamics and Surface Roughness of Water/Hydrocarbon Interfaces.
137. S. Toxvaerd and J. Stecki, *J. Chem. Phys.*, **102**, 7163 (1995). Density Profiles at a Planar Liquid-Liquid Interface.
138. D. Michael and I. Benjamin, *J. Electroanal. Chem.*, **450**, 335 (1998). Molecular Dynamics Simulation of the Water/Nitrobenzene Interface.
139. P. A. Fernandes, M. N. D. S. Cordeiro, and J. A. N. F. Gomes, *J. Phys. Chem. B*, **103**, 6290 (1999). Molecular Dynamics Simulation of the Water/2-Heptanone Liquid-Liquid Interface.
140. J. Chowdhary and B. M. Ladanyi, *J. Phys. Chem. B*, **110**, 15442 (2006). Water-Hydrocarbon Interfaces: Effect of Hydrocarbon Branching on Interfacial Structure.
141. M. N. D. S. Cordeiro, *Molecular Simulation*, **29**, 817 (2003). Interfacial Tension Behaviour of Water/Hydrocarbon Liquid-Liquid Interfaces: A Molecular Dynamics Simulation.
142. M. Jorge and M. N. D. S. Cordeiro, *J. Phys. Chem. C*, **111**, 17612 (2007). Intrinsic Structure and Dynamics of the Water/Nitrobenzene Interface.
143. M. Jorge and M. N. D. S. Cordeiro, *J. Phys. Chem. B*, **112**, 2415 (2008). Molecular Dynamics Study of the Interface between Water and 2-Nitrophenyl Octyl Ether.
144. I. Napari, A. Laaksonen, V. Talanquer, and D. W. Oxtoby, *J. Chem. Phys.*, **110**, 5906 (1999). A Density Functional Study of Liquid-Liquid Interfaces in Partially Miscible Systems.
145. P. Geysermans, N. Elyeznasni, and V. Russier, *J. Chem. Phys.*, **123** (2005). Layered Interfaces Between Immiscible Liquids Studied by Density-Functional Theory and Molecular-Dynamics Simulations.
146. K. Kashimoto, J. Yoon, B. Y. Hou, C. H. Chen, B. H. Lin, M. Aratono, T. Takiue, and M. L. Schlossman, *Phys. Rev. Lett.*, **101** (2008). Structure and Depletion at Fluorocarbon and Hydrocarbon/Water Liquid/Liquid Interfaces.
147. M. Requardt, *J. Stat. Phys.*, **64**, 807 (1991). Does the Three-Dimensional Capillary Wave Model Lead to a Universally Valid and Pathology-Free Description of the Liquid–vapor Interface near $g = 0$? A Controversial Point of View.
148. S. Senapati and M. L. Berkowitz, *Phys. Rev. Lett.*, **87**, 176101 (2001). Computer Simulation Study of the Interface Width of the Liquid/Liquid Interface.
149. B. Lee and F. M. Richards, *J. Mol. Bio.*, **55**, 379 (1971). Interpretation of Protein Structures – Estimation of Static Accessibility.

-
150. E. Chacón, P. Tarazona, and J. Alejandre, *J. Chem. Phys.*, **125**, 014709 (2006). The Intrinsic Structure of the Water Surface.
151. G. Hantal, P. Terleczy, G. Horvai, L. Nyulaszi, and P. Jedlovsky, *J. Phys. Chem. C*, **113**, 19263 (2009). Molecular Level Properties of the Water-Dichloromethane Liquid/Liquid Interface, as Seen from Molecular Dynamics Simulation and Identification of Truly Interfacial Molecules Analysis.
152. A. P. Willard and D. Chandler, *J. Phys. Chem. B*, **114**, 1954 (2010). Instantaneous Liquid Interfaces.
153. M. Jorge, G. Hantal, P. Jedlovsky, and M. N. D. S. Cordeiro, *J. Phys. Chem. C*, **114**, 18656 (2010). Critical Assessment of Methods for the Intrinsic Analysis of Liquid Interfaces. 2. Density Profiles.
154. D. M. Mitrovic, A. M. Tikhonov, M. Li, Z. Huang, and M. L. Schlossman, *Phys. Rev. Lett.*, **85**, 582 (2000). Noncapillary-Wave Structure at the Water-Alkane Interface.
155. E. Chacón and P. Tarazona, *Phys. Rev. Lett.*, **91**, 166103 (2003). Intrinsic Profiles Beyond the Capillary Wave Theory: A Monte Carlo Study.
156. F. Bresme, E. Chacón, P. Tarazona, and K. Tay, *Phys. Rev. Lett.*, **101** (2008). Intrinsic Structure of Hydrophobic Surfaces: The Oil–Water Interface.
157. J. R. Errington and D. A. Kofke, *J. Chem. Phys.*, **127**, 174709 (2007). Calculation of Surface Tension Via Area Sampling.
158. E. M. Blokhuis, D. Bedeaux, and C. D. Holcomb, *Mol. Phys.*, **85**, 665 (1995). Tail Corrections to the Surface Tension of a Lennard-Jones Liquid-Vapour Interface.
159. J. H. Irving and J. G. Kirkwood, *J. Chem. Phys.*, **18**, 817 (1950). The Statistical Mechanical Theory of Transport Processes. 4. The Equations of Hydrodynamics.
160. J. P. R. B. Walton, D. J. Tildesley, J. S. Rowlinson, and J. R. Henderson, *Mol. Phys.*, **48**, 1357 (1983). The Pressure Tensor at the Planar Surface of a Liquid.
161. A. Ghoufi, F. Goujon, V. Lachet, and P. Malfreyt, *J. Chem. Phys.*, **128**, 154716 (2008). Multiple Histogram Reweighting Method for the Surface Tension Calculation.
162. F. Biscay, A. Ghoufi, V. Lachet, and P. Malfreyt, *Phys. Chem. Chem. Phys.*, **11**, 6132 (2009). Calculation of the Surface Tension of Cyclic and Aromatic Hydrocarbons from Monte Carlo Simulations Using an Anisotropic United Atom Model.
163. M. X. Guo and B. C. Y. Lu, *J. Chem. Phys.*, **106**, 3688 (1997). Long Range Corrections to Thermodynamic Properties of Inhomogeneous Systems with Planar Interfaces.
164. A. Ghoufi, F. Goujon, V. Lachet, and P. Malfreyt, *Phys. Rev. E*, **77** (2008). Expressions for Local Contributions to the Surface Tension from the Virial Route.
165. F. Chen and P. E. Smith, *J. Chem. Phys.*, **126** (2007). Simulated Surface Tensions of Common Water Models.
166. K. E. Gubbins, in *Fluid Interfacial Phenomena*, C. A. Croxton (Ed.), Wiley, New York, 1986, p. 477, Molecular Orientation at the Free Liquid Surface.
167. T. Raising, Y. R. Shen, M. W. Kim, P. Valint, and J. Bock, *Phys. Rev. A*, **31**, 537 (1985). Orientation of Surfactant Molecules at a Liquid-Air Interface Measured by Optical Second-Harmonic Generation.
168. M. C. Goh, J. M. Hicks, K. Kemnitz, G. R. Pinto, K. Bhattacharyya, K. B. Eisenthal, and T. F. Heinz, *J. Phys. Chem.*, **92**, 5074 (1988). Absolute Orientation of Water Molecules at the Neat Water Surface.
169. D. A. Higgins, R. R. Naujok, and R. M. Corn, *Chem. Phys. Lett.*, **213**, 485 (1993). Second Harmonic Generation Measurements of Molecular Orientation and Coadsorption at the Interface between Two Immiscible Electrolyte Solutions.
170. R. R. Naujok, D. A. Higgins, D. G. Hanken, and R. M. Corn, *J. Chem. Soc. Faraday Trans.*, **91**, 1411 (1995). Optical Second-Harmonic Generation Measurements of Molecular Adsorption and Orientation at the Liquid/Liquid Electrochemical Interface.
171. F. Eisert, O. Dannenberger, and M. Buck, *Phys. Rev. B*, **58**, 10860 (1998). Molecular Orientation Determined by Second-Harmonic Generation: Self-Assembled Monolayers.

172. Y. R. Shen and V. Ostroverkhov, *Chem. Rev.*, **106**, 1140 (2006). Sum-Frequency Vibrational Spectroscopy on Water Interfaces: Polar Orientation of Water Molecules at Interfaces.
173. Y. Rao, M. Comstock, and K. B. Eisenthal, *J. Phys. Chem. B*, **110**, 1727 (2006). Absolute Orientation of Molecules at Interfaces.
174. M. Matsumoto and Y. Kataoka, *J. Chem. Phys.*, **88**, 3233 (1988). Study on Liquid–Vapor Interface of Water. I. Simulational Results of Thermodynamic Properties and Orientational Structure.
175. P. Jedlovsky, Á. Vincze, and G. Horvai, *J. Chem. Phys.*, **117**, 2271 (2002). New Insight into the Orientational Order of Water Molecules at the Water/1,2-Dichloroethane Interface: A Monte Carlo Simulation Study.
176. P. Jedlovsky, Á. Vincze, and G. Horvai, *J. Mol. Liq.*, **109**, 99 (2004). Properties of Water/Apolar Interfaces as Seen from Monte Carlo Simulations.
177. P. Jedlovsky, Á. Vincze, and G. Horvai, *Phys. Chem. Chem. Phys.*, **6**, 1874 (2004). Full Description of the Orientational Statistics of Molecules near to Interfaces. Water at the Interface with CCl₄.
178. D. S. Walker, D. K. Hore, and G. L. Richmond, *J. Phys. Chem. B*, **110**, 20451 (2006). Understanding the Population, Coordination, and Orientation of Water Species Contributing to the Nonlinear Optical Spectroscopy of the Vapor–Water Interface through Molecular Dynamics Simulations.
179. G. Hantal, M. Darvas, L. B. Partay, G. Horvai, and P. Jedlovsky, *J. Phys.-Condensed Matter*, **22**, 284112 (2010). Molecular Level Properties of the Free Water Surface and Different Organic Liquid/Water Interfaces, as Seen from ITIM Analysis of Computer Simulation Results.
180. W. L. Jorgensen, *Chem. Phys. Lett.*, **70**, 326 (1980). Monte-Carlo Results for Hydrogen-Bond Distributions in Liquid Water.
181. M. Matsumoto and I. Ohmine, *J. Chem. Phys.*, **104**, 2705 (1996). A New Approach to the Dynamics of Hydrogen Bond Network in Liquid Water.
182. F. W. Starr, J. K. Nielsen, and H. E. Stanley, *Phys. Rev. Lett.*, **82**, 2294 (1999). Fast and Slow Dynamics of Hydrogen Bonds in Liquid Water.
183. M. G. Sceats and S. A. Rice, *J. Chem. Phys.*, **72**, 3236 (1980). The Water–Water Pair Potential near the Hydrogen-Bonded Equilibrium Configuration.
184. M. Mezei and D. L. Beveridge, *J. Chem. Phys.*, **74**, 622 (1981). Theoretical-Studies of Hydrogen-Bonding in Liquid Water and Dilute Aqueous-Solutions.
185. A. Luzar and D. Chandler, *Nature*, **379**, 55 (1996). Hydrogen-Bond Kinetics in Liquid Water.
186. R. Kumar, J. R. Schmidt, and J. L. Skinner, *J. Chem. Phys.*, **126**, 204107 (2007). Hydrogen Bonding Definitions and Dynamics in Liquid Water.
187. F. W. Starr, J. K. Nielsen, and H. E. Stanley, *Phys. Rev. E*, **62**, 579 (2000). Hydrogen-Bond Dynamics for the Extended Simple Point-Charge Model of Water.
188. J. B. Brubach, A. Mermet, A. Filabozzi, A. Gerschel, and P. Roy, *J. Chem. Phys.*, **122**, 184509 (2005). Signatures of the Hydrogen Bonding in the Infrared Bands of Water.
189. D. A. Schmidt and K. Miki, *J. Phys. Chem. A*, **111**, 10119 (2007). Structural Correlations in Liquid Water: A New Interpretation of IR Spectroscopy.
190. P. L. Geissler, *J. Am. Chem. Soc.*, **127**, 14930 (2005). Temperature Dependence of Inhomogeneous Broadening: On the Meaning of Isosbestic Points.
191. Q. Du, R. Superfine, E. Freysz, and Y. R. Shen, *Phys. Rev. Lett.*, **70**, 2313 (1993). Vibrational Spectroscopy of Water at the Vapor/Water Interface.
192. Q. Du, E. Freysz, and Y. R. Shen, *Science*, **264**, 826 (1994). Surface Vibrational Spectroscopic Studies of Hydrogen Bonding and Hydrophobicity.
193. L. F. Scatena, M. G. Brown, and G. L. Richmond, *Science*, **292**, 908 (2001). Water at Hydrophobic Surfaces: Weak Hydrogen Bonding and Strong Orientation Effects.

-
194. I. V. Stiopkin, H. D. Jayathilake, A. N. Bordenyuk, and A. V. Benderskii, *J. Am. Chem. Soc.*, **130**, 2271 (2008). Heterodyne-Detected Vibrational Sum Frequency Generation Spectroscopy.
195. M. Sovago, R. K. Campen, G. W. H. Wurpel, M. Muller, H. J. Bakker, and M. Bonn, *Phys. Rev. Lett.*, **100**, 173901 (2008). Vibrational Response of Hydrogen-Bonded Interfacial Water Is Dominated by Intramolecular Coupling.
196. C. S. Tian and Y. R. Shen, *Chem. Phys. Lett.*, **470**, 1 (2009). Sum-Frequency Vibrational Spectroscopic Studies of Water/Vapor Interfaces.
197. A. M. Jubb, W. Hua, and H. C. Allen, *Annu. Rev. Phys. Chem.*, **63**, 107 (2012). Environmental Chemistry at Vapor/Water Interfaces: Insights from Vibrational Sum Frequency Generation Spectroscopy.
198. I. V. Stiopkin, C. Weeraman, P. A. Pieniazek, F. Y. Shalhout, J. L. Skinner, and A. V. Benderskii, *Nature*, **474**, 192 (2011). Hydrogen Bonding at the Water Surface Revealed by Isotopic Dilution Spectroscopy.
199. J. L. Skinner, B. M. Auer, and Y. S. Lin, *Adv. Chem. Phys.*, **142**, 59 (2009). Vibrational Line Shapes, Spectral Diffusion, and Hydrogen Bonding in Liquid Water.
200. I. Benjamin, *Phys. Rev. Lett.*, **73**, 2083 (1994). Vibrational Spectrum of Water at the Liquid/Vapor Interface.
201. I. F. W. Kuo and C. J. Mundy, *Science*, **303**, 658 (2004). An Ab Initio Molecular Dynamics Study of the Aqueous Liquid–Vapor Interface.
202. V. Buch, *J. Phys. Chem. B*, **109**, 17771 (2005). Molecular Structure and OH-Stretch Spectra of Liquid Water Surface.
203. F. G. Moore and G. L. Richmond, *Acc. Chem. Res.*, **41**, 739 (2008). Integration or Segregation: How Do Molecules Behave at Oil/Water Interfaces?
204. A. Perry, C. Neipert, B. Space, and P. B. Moore, *Chem. Rev.*, **106**, 1234 (2006). Theoretical Modeling of Interface Specific Vibrational Spectroscopy: Methods and Applications to Aqueous Interfaces.
205. A. Morita and J. T. Hynes, *J. Phys. Chem. B.*, **106**, 673 (2002). A Theoretical Analysis of the Sum Frequency Generation Spectrum of the Water Surface. II. Time-Dependent Approach.
206. A. Morita, *J. Phys. Chem. B*, **110**, 3158 (2006). Improved Computation of Sum Frequency Generation Spectrum of the Surface of Water.
207. B. M. Auer and J. L. Skinner, *J. Chem. Phys.*, **129**, 214705 (2008). Vibrational Sum-Frequency Spectroscopy of the Liquid/Vapor Interface for Dilute HOD in D₂O.
208. C. J. Tainter, P. A. Pieniazek, Y. S. Lin, and J. L. Skinner, *J. Chem. Phys.*, **134**, 184501 (2011). Robust Three-Body Water Simulation Model.
209. J. L. Skinner, P. A. Pieniazek, and S. M. Gruenbaum, *Acc. Chem. Res.*, **45**, 93 (2012). Vibrational Spectroscopy of Water at Interfaces.
210. D. S. Walker and G. L. Richmond, *J. Phys. Chem. C.*, **111**, 8321 (2007). Understanding the Effects of Hydrogen Bonding at the Vapor–Water Interface: Vibrational Sum Frequency Spectroscopy of H₂O/HOD/D₂O Mixtures Studied Using Molecular Dynamics Simulations.
211. M. D. Fayer, *Acc. Chem. Res.*, **45**, 3 (2012). Dynamics of Water Interacting with Interfaces, Molecules, and Ions.
212. D. Chandler, *Introduction to Modern Statistical Mechanics*, Oxford University Press, Oxford, 1987.
213. D. Duque, P. Tarazona, and E. Chacón, *J. Chem. Phys.*, **128**, 134704 (2008). Diffusion at the Liquid–Vapor Interface.
214. R. G. Winkler, R. H. Schmid, A. Gerstmair, and P. Reineker, *J. Chem. Phys.*, **104**, 8103 (1996). Molecular Dynamics Simulation Study of the Dynamics of Fluids in Thin Films.
215. E. A. J. F. Peters and T. M. A. O. M. Barenbrug, *Phys. Rev. E*, **66** (056701) (2002). Efficient Brownian Dynamics Simulation of Particles near Walls. I. Reflecting and Absorbing Walls.
216. M. Sega, R. Vallauri, and S. Melchionna, *Phys. Rev. E*, **72**, 041201 (2005). Diffusion of Water in Confined Geometry: The Case of a Multilamellar Bilayer.

217. P. Liu, E. Harder, and B. J. Berne, *J. Phys. Chem. B*, **108**, 6595 (2004). On the Calculation of Diffusion Coefficients in Confined Fluids and Interfaces with an Application to the Liquid–Vapor Interface of Water.
218. J. Chowdhary and B. M. Ladanyi, *J. Phys. Chem. B*, **112**, 6259 (2008). Water/Hydrocarbon Interfaces: Effect of Hydrocarbon Branching on Single-Molecule Relaxation.
219. W. A. Steele, *Adv. Chem. Phys.*, **34**, 1 (1976). The Rotation of Molecules in Dense Phases.
220. A. I. Burshtein and S. I. Temkin, *Spectroscopy of Molecular Rotation in Gases and Liquids*, Cambridge University Press, Cambridge, 1994.
221. G. R. Fleming, *Chemical Applications of Ultrafast Spectroscopy*, New York, Oxford University, 1986.
222. X. Wei and Y. R. Shen, *Phys. Rev. Lett.*, **86**, 4799 (2001). Motional Effect in Surface Sum-Frequency Vibrational Spectroscopy.
223. J. T. Fourkas, R. A. Walker, S. Z. Can, and E. Gershgoren, *J. Phys. Chem. C*, **111**, 8902 (2007). Effects of Reorientation in Vibrational Sum-Frequency Spectroscopy.
224. M. Hayashi, Y. J. Shiu, K. K. Liang, S. H. Lin, and Y. R. Shen, *J. Phys. Chem. A*, **111**, 9062 (2007). Theory of Time-Resolved Sum-Frequency Generation and Its Applications to Vibrational Dynamics of Water.
225. H. K. Nienhuys and M. Bonn, *J. Phys. Chem. B*, **113**, 7564 (2009). Measuring Molecular Reorientation at Liquid Surfaces with Time-Resolved Sum-Frequency Spectroscopy: A Theoretical Framework.
226. Z. Gengeliczki, D. E. Rosenfeld, and M. D. Fayer, *J. Chem. Phys.*, **132**, 244703 (2010). Theory of Interfacial Orientational Relaxation Spectroscopic Observables.
227. C. S. Hsieh, R. K. Campen, A. C. V. Verde, P. Bolhuis, H. K. Nienhuys, and M. Bonn, *Phys. Rev. Lett.*, **107**, 116102 (2011). Ultrafast Reorientation of Dangling OH Groups at the Air–Water Interface Using Femtosecond Vibrational Spectroscopy.
228. I. Benjamin, *J. Chem. Phys.*, **95**, 3698 (1991). Theoretical Study of Ion Solvation at the Water Liquid–Vapor Interface.
229. S. R. V. Castrillon, N. Giovambattista, I. A. Aksay, and P. G. Debenedetti, *J. Phys. Chem. B*, **113**, 1438 (2009). Effect of Surface Polarity on the Structure and Dynamics of Water in Nanoscale Confinement.
230. G. Stirnemann, P. J. Rossky, J. T. Hynes, and D. Laage, *Faraday Discuss.*, **146**, 263 (2010). Water Reorientation, Hydrogen-Bond Dynamics and 2D-IR Spectroscopy Next to an Extended Hydrophobic Surface.
231. G. Stirnemann, S. R. V. Castrillon, J. T. Hynes, P. J. Rossky, P. G. Debenedetti, and D. Laage, *Phys. Chem. Chem. Phys.*, **13**, 19911 (2011). Non-Monotonic Dependence of Water Reorientation Dynamics on Surface Hydrophilicity: Competing Effects of the Hydration Structure and Hydrogen-Bond Strength.
232. D. Laage and J. T. Hynes, *Science*, **311**, 832 (2006). A Molecular Jump Mechanism of Water Reorientation.
233. G. M. Gale, G. Gallot, F. Hache, N. Lascoux, S. Bratos, and J.-C. Leicknam, *Phys. Rev. Lett.*, **82**, 1068 (1999). Femtosecond Dynamics of Hydrogen Bonds in Liquid Water: A Real Time Study.
234. J. B. Asbury, T. Steinell, C. Stromberg, K. J. Gaffney, I. R. Piletic, A. Goun, and M. D. Fayer, *Phys. Rev. Lett.*, **91**, 7402 (2003). Hydrogen Bond Dynamics Probed with Ultrafast Infrared Heterodyne-Detected Multidimensional Vibrational Stimulated Echoes.
235. C. J. Fecko, J. D. Eaves, J. J. Loparo, A. Tokmakoff, and P. L. Geissler, *Science*, **301**, 1698 (2003). Ultrafast Hydrogen-Bond Dynamics in the Infrared Spectroscopy of Water.
236. E. T. J. Nibbering and T. Elsaesser, *Chem. Rev.*, **104**, 1887 (2004). Ultrafast Vibrational Dynamics of Hydrogen Bonds in the Condensed Phase.
237. S. Park and M. D. Fayer, *Proc. Nat. Acad. Sci. U. S. A.*, **104**, 16731 (2007). Hydrogen Bond Dynamics in Aqueous NaBr Solutions.

-
238. F. D'amico, F. Bencivenga, A. Gessini, and C. Masciovecchio, *J. Phys. Chem. B*, **114**, 10628 (2010). Temperature Dependence of Hydrogen-Bond Dynamics in Acetic Acid-Water Solutions.
239. A. A. Bakulin, M. S. Pshenichnikov, H. J. Bakker, and C. Petersen, *J. Phys. Chem. A*, **115**, 1821 (2011). Hydrophobic Molecules Slow Down the Hydrogen-Bond Dynamics of Water.
240. A. Luzar and D. Chandler, *Phys. Rev. Lett.*, **76**, 928 (1996). Effect of Environment on Hydrogen Bond Dynamics in Liquid Water.
241. A. Luzar, *J. Chem. Phys.*, **113**, 10663 (2000). Resolving the Hydrogen Bond Dynamics Conundrum.
242. A. Chandra, *Phys. Rev. Lett.*, **85**, 768 (2000). Effects of Ion Atmosphere on Hydrogen-Bond Dynamics in Aqueous Electrolyte Solutions.
243. H. Xu, H. A. Stern, and B. J. Berne, *J. Phys. Chem. B*, **106**, 2054 (2002). Can Water Polarizability Be Ignored in Hydrogen Bond Kinetics?
244. K. B. Mller, R. Rey, and J. T. Hynes, *J. Phys. Chem. A*, **108**, 1275 (2004). Hydrogen Bond Dynamics in Water and Ultrafast Infrared Spectroscopy: A Theoretical Study.
245. B. Nigro, S. Re, D. Laage, R. Rey, and J. T. Hynes, *J. Phys. Chem. A*, **110**, 11237 (2006). On the Ultrafast Infrared Spectroscopy of Anion Hydration Shell Hydrogen Bond Dynamics.
246. F. Sterpone, G. Stirnemann, J. T. Hynes, and D. Laage, *J. Phys. Chem. B*, **114**, 2083 (2010). Water Hydrogen-Bond Dynamics around Amino Acids: The Key Role of Hydrophilic Hydrogen-Bond Acceptor Groups.
247. B. S. Mallik and A. Chandra, *J. Chem. Sci.*, **124**, 215 (2012). Hydrogen Bond Dynamics and Vibrational Spectral Diffusion in Aqueous Solution of Acetone: A First Principles Molecular Dynamics Study.
248. S. Balasubramanian, S. Pal, and B. Bagchi, *Phys. Rev. Lett.*, **89**, 115505/1 (2002). Hydrogen-Bond Dynamics near a Micellar Surface: Origin of the Universal Slow Relaxation at Complex Aqueous Interfaces.
249. M. Tarek and D. J. Tobias, *Phys. Rev. Lett.*, **88**, 138101 (2002). Role of Protein-Water Hydrogen Bond Dynamics in the Protein Dynamical Transition.
250. C. F. Lopez, S. O. Nielsen, M. L. Klein, and P. B. Moore, *J. Phys. Chem. B*, **108**(6603) (2004). Hydrogen Bonding Structure and Dynamics of Water at the Dimyristoylphosphatidylcholine Lipid Bilayer Surface from a Molecular Dynamics Simulation.
251. S. Paul and A. Chandra, *Chem. Phys. Lett.*, **386**, 218 (2004). Hydrogen Bond Dynamics at Vapour-Water and Metal-Water Interfaces.
252. P. Liu, E. Harder, and B. J. Berne, *J. Phys. Chem. B*, **109**, 2949 (2005). Hydrogen-Bond Dynamics in the Air-Water Interface.
253. I. Benjamin, *J. Phys. Chem. B*, **109**, 13711 (2005). Hydrogen Bond Dynamics at Water/Organic Liquid Interfaces.
254. N. Winter, J. Vieceli, and I. Benjamin, *J. Phys. Chem. B*, **112**, 227 (2008). Hydrogen-Bond Structure and Dynamics at the Interface between Water and Carboxylic Acid-Functionalized Self-Assembled Monolayers.
255. B. Jana, S. Pal, and B. Bagchi, *J. Phys. Chem. B*, **112**, 9112 (2008). Hydrogen Bond Breaking Mechanism and Water Reorientational Dynamics in the Hydration Layer of Lysozyme.
256. J. Chowdhary and B. M. Ladanyi, *J. Phys. Chem. B*, **113**, 4045 (2009). Hydrogen Bond Dynamics at the Water/Hydrocarbon Interface.
257. D. E. Rosenfeld and C. A. Schmittenmaer, *J. Phys. Chem. B*, **115**, 1021 (2011). Dynamics of the Water Hydrogen Bond Network at Ionic, Nonionic, and Hydrophobic Interfaces in Nanopores and Reverse Micelles.
258. T. Yamamoto, *J. Chem. Phys.*, **33**, 281 (1960). Quantum Statistical Mechanical Theory of the Rate of Exchange Chemical Reactions in the Gas Phase.
259. I. Benjamin, *J. Chem. Phys.*, **110**, 8070 (1999). Structure Thermodynamics and Dynamics of the Liquid/Vapor Interface of Water/DMSO Mixtures.

260. T.-M. Chang and L. X. Dang, *J. Phys. Chem. B*, **109**, 5759 (2005). Liquid–Vapor Interface of Methanol–Water Mixtures: A Molecular Dynamics Study.
261. P. Salvador, J. E. Curtis, D. J. Tobias, and P. Jungwirth, *Phys. Chem. Chem. Phys.*, **5**, 3752 (2003). Polarizability of the Nitrate Anion and Its Solvation at the Air/Water Interface.
262. B. Minofar, M. Mucha, P. Jungwirth, X. Yang, Y. J. Fu, X. B. Wang, and L. S. Wang, *J. Am. Chem. Soc.*, **126**, 11691 (2004). Bulk Versus Interfacial Aqueous Solvation of Dicarboxylate Dianions.
263. L. Vrbka, M. Mucha, B. Minofar, P. Jungwirth, E. C. Brown, and D. J. Tobias, *Curr. Opin. Coll. Interf. Sci.*, **9**, 67 (2004). Propensity of Soft Ions for the Air/Water Interface.
264. P. B. Petersen and R. J. Saykally, *J. Phys. Chem. B*, **109**, 7976 (2005). Evidence for an Enhanced Hydronium Concentration at the Liquid Water Surface.
265. P. B. Petersen, R. J. Saykally, M. Mucha, and P. Jungwirth, *J. Phys. Chem. B*, **109**, 10915 (2005). Enhanced Concentration of Polarizable Anions at the Liquid Water Surface: SHG Spectroscopy and MD Simulations of Sodium Thiocyanide.
266. T. M. Chang and L. X. Dang, *Chem. Rev.*, **106**, 1305 (2006). Recent Advances in Molecular Simulations of Ion Solvation at Liquid Interfaces.
267. P. Jungwirth and D. J. Tobias, *Chem. Rev.*, **106**, 1259 (2006). Specific Ion Effects at the Air/Water Interface.
268. P. Jungwirth and B. Winter, *Ann. Rev. Phys. Chem.*, **59**, 343 (2008). Ions at Aqueous Interfaces: From Water Surface to Hydrated Proteins.
269. L. Sun, X. Li, T. Hede, Y. Q. Tu, C. Leck, and H. Agren, *J. Phys. Chem. B*, **116**, 3198 (2012). Molecular Dynamics Simulations of the Surface Tension and Structure of Salt Solutions and Clusters.
270. S. Gopalakrishnan, P. Jungwirth, D. J. Tobias, and H. C. Allen, *J. Phys. Chem. B*, **109**, 8861 (2005). Air–Liquid Interfaces of Aqueous Solutions Containing Ammonium and Sulfate: Spectroscopic and Molecular Dynamics Studies.
271. P. B. Petersen and R. J. Saykally, *Annu. Rev. Phys. Chem.*, **57**, 333 (2006). On the Nature of Ions at the Liquid Water Surface.
272. E. C. Brown, M. Mucha, P. Jungwirth, and D. J. Tobias, *J. Phys. Chem. B*, **109**, 7934 (2005). Structure and Vibrational Spectroscopy of Salt Water/Air Interfaces: Predictions from Classical Molecular Dynamics Simulations.
273. G. Luo, S. Malkova, J. Yoon, D. G. Schultz, B. Lin, M. Meron, I. Benjamin, P. Vanysek, and M. L. Schlossman, *Science*, **311**, 216 (2006). Ion Distributions near a Liquid–Liquid Interface.
274. G. Luo, S. Malkova, J. Yoon, D. G. Schultz, B. Lin, M. Meron, I. Benjamin, P. Vanysek, and M. L. Schlossman, *J. Electroanal. Chem.*, **593**, 142 (2006). Ion Distributions at the Nitrobenzene–Water Interface Electrified by a Common Ion.
275. A. Pohorille and M. A. Wilson, *J. Mol. Struct.*, **103**, 271 (1993). Molecular Structure of Aqueous Interfaces.
276. S. Kumar, J. M. Rosenberg, D. Bouzida, R. H. Swendsen, and P. A. Kollman, *J. Comput. Chem.*, **16**, 1339 (1995). Multidimensional Free-Energy Calculations Using the Weighted Histogram Analysis Method.
277. J. Kastner, *Wiley Interdisciplinary Reviews-Computational Molecular Science*, **1**, 932 (2011). Umbrella Sampling.
278. K. J. Schweighofer and I. Benjamin, *Chem. Phys. Lett.*, **202**, 379 (1993). Dynamics of Ion Desorption from the Liquid–Vapor Interface of Water.
279. E. Darve and A. Pohorille, *J. Chem. Phys.*, **115**, 9169 (2001). Calculating Free Energies Using Average Force.
280. L. X. Dang, *J. Phys. Chem. B*, **106**, 10388 (2002). Computational Study of Ion Binding to the Liquid Interface of Water.
281. C. D. Wick and L. X. Dang, *J. Phys. Chem. B*, **110**, 6824 (2006). Distribution, Structure, and Dynamics of Cesium and Iodide Ions at the H_2O – CCl_4 and H_2O –Vapor Interfaces.

-
282. C. D. Wick and L. X. Dang, *J. Phys. Chem. C*, **112**, 647 (2008). Molecular Dynamics Study of Ion Transfer and Distribution at the Interface of Water and 1,2-Dichloroethane.
283. A. Pohorille, C. Jarzynski, and C. Chipot, *J. Phys. Chem. B*, **114**, 10235 (2010). Good Practices in Free-Energy Calculations.
284. T. P. Straatsma, in *Reviews in Computational Chemistry*, K. B. Lipkowitz and D. B. Boyd (Eds.), VCH Publishers, New York, 1996, Vol. 9, p. 81, Free Energy by Molecular Simulation.
285. M. A. Wilson and A. Pohorille, *J. Chem. Phys.*, **95**, 6005 (1991). Interaction of Monovalent Ions with the Water Liquid–Vapor Interface: A Molecular Dynamics Study.
286. M. N. Tamashiro and M. A. Constantino, *J. Phys. Chem. B*, **114**, 3583 (2010). Ions at the Water–Vapor Interface.
287. Y. Levin, *J. Chem. Phys.*, **129** (2008). “Phantom Ion Effect” And the Contact Potential of the Water–Vapor Interface.
288. Y. Levin, A. P. dos Santos, and A. Diehl, *Phys. Rev. Lett.*, **103** (2009). Ions at the Air–Water Interface: An End to a Hundred-Year-Old Mystery?
289. A. P. dos Santos and Y. Levin, *Langmuir*, **28**, 1304 (2012). Ions at the Water–Oil Interface: Interfacial Tension of Electrolyte Solutions.
290. G. L. Warren and S. Patel, *J. Phys. Chem. C*, **112**, 7455 (2008). Comparison of the Solvation Structure of Polarizable and Nonpolarizable Ions in Bulk Water and near the Aqueous Liquid–vapor Interface.
291. E. A. Raymond and G. L. Richmond, *J. Phys. Chem. B*, **108**, 5051 (2004). Probing the Molecular Structure and Bonding of the Surface of Aqueous Salt Solutions.
292. D. F. Liu, G. Ma, L. M. Levering, and H. C. Allen, *J. Phys. Chem. B*, **108**, 2252 (2004). Vibrational Spectroscopy of Aqueous Sodium Halide Solutions and Air–Liquid Interfaces: Observation of Increased Interfacial Depth.
293. C. Coleman, J. S. Hub, P. J. van Maaren, and D. van der Spoel, *Proc. Natl. Acad. Sci. U.S.A.*, **108**, 6838 (2011). Atomistic Simulation of Ion Solvation in Water Explains Surface Preference of Halides.
294. J. Noah-Vanhoecke and P. L. Geissler, *Proc. Nat. Acad. Sci. U. S. A.*, **106**, 15125 (2009). On the Fluctuations That Drive Small Ions toward, and Away from, Interfaces between Polar Liquids and Their Vapors.
295. T. L. Tarbuck, S. T. Ota, and G. L. Richmond, *J. Am. Chem. Soc.*, **128**, 14519 (2006). Spectroscopic Studies of Solvated Hydrogen and Hydroxide Ions at Aqueous Surfaces.
296. R. Vacha, D. Horinek, M. L. Berkowitz, and P. Jungwirth, *Phys. Chem. Chem. Phys.*, **10**, 4975 (2008). Hydronium and Hydroxide at the Interface between Water and Hydrophobic Media.
297. B. Winter, M. Faubel, R. Vacha, and P. Jungwirth, *Chem. Phys. Lett.*, **474**, 241 (2009). Behavior of Hydroxide at the Water/Vapor Interface.
298. B. Winter, M. Faubel, R. Vacha, and P. Jungwirth, *Chem. Phys. Lett.*, **481**, 19 (2009). Reply to Comments on Frontiers Article ‘Behavior of Hydroxide at the Water/Vapor Interface’.
299. J. K. Beattie, *Chem. Phys. Lett.*, **481**, 17 (2009). Comment on ‘Behaviour of Hydroxide at the Water/Vapor Interface’ [*Chem. Phys. Lett.* 474 (2009) 241].
300. A. Gray-Weale, *Chem. Phys. Lett.*, **481**, 22 (2009). Comment on ‘Behaviour of Hydroxide at the Water/Vapor Interface’ [*Chem. Phys. Lett.* 474 (2009) 241].
301. C. J. Mundy, I. F. W. Kuo, M. E. Tuckerman, H. S. Lee, and D. J. Tobias, *Chem. Phys. Lett.*, **481**, 2 (2009). Hydroxide Anion at the Air–Water Interface.
302. K. J. Schweighofer and I. Benjamin, *J. Phys. Chem.*, **99**, 9974 (1995). Transfer of Small Ions across the Water/1,2-Dichloroethane Interface.
303. A. Pohorille, P. Cieplak, and M. A. Wilson, *Chem. Phys.*, **204**, 337 (1996). Interactions of Anesthetics with the Membrane–Water Interface.
304. C. Chipot, M. A. Wilson, and A. Pohorille, *J. Phys. Chem. B*, **101**, 782 (1997). Interactions of Anesthetics with the Water–Hexane Interface. A Molecular Dynamics Study.

305. I. Benjamin, *Annu. Rev. Phys. Chem.*, **48**, 401 (1997). Molecular Structure and Dynamics at Liquid-Liquid Interfaces.
306. K. J. Schweighofer and I. Benjamin, *J. Phys. Chem. A*, **103**, 10274 (1999). Transfer of a Tetra Methyl Ammonium Ion across the Water-Nitrobenzene Interface: Potential of Mean Force and Non-Equilibrium Dynamics.
307. L. X. Dang, *J. Phys. Chem. B*, **103**, 8195 (1999). Computer Simulation Studies of Ion Transport across a Liquid/Liquid Interface.
308. C. D. Wick and L. X. Dang, *Chem. Phys. Lett.*, **458**, 1 (2008). Recent Advances in Understanding Transfer Ions across Aqueous Interfaces.
309. C. D. Wick and L. X. Dang, *J. Phys. Chem. C*, **112**, 647 (2008). Molecular Dynamics Study of Ion Transfer and Distribution at the Interface of Water and 1,2-Dichloroethane.
310. N. Kikkawa, T. Ishiyama, and A. Morita, *Chem. Phys. Lett.*, **534**, 19 (2012). Molecular Dynamics Study of Phase Transfer Catalyst for Ion Transfer through Water-Chloroform Interface.
311. D. Rose and I. Benjamin, *J. Phys. Chem. B*, **113**, 9296 (2009). Free Energy of Transfer of Hydrated Ion Clusters from Water to an Immiscible Organic Solvent.
312. M. Saraniti, S. Aboud, and R. Eisenberg, in *Reviews in Computational Chemistry*, K. B. Lipkowitz, T. R. Cundari, and V. J. Gillet (Eds.), Wiley, New York, 2006, Vol. **22**, p. 229, The Simulation of Ionic Charge Transport in Biological Ion Channels: An Introduction to Numerical Methods.
313. M. A. Wilson, C. Y. Wei, P. Bjelkmar, B. A. Wallace, and A. Pohorille, *Biophysical Journal*, **100**, 2394 (2011). Molecular Dynamics Simulation of the Antiamoebin Ion Channel: Linking Structure and Conductance.
314. I. Chorny and I. Benjamin, *J. Phys. Chem. B*, **109**, 16455 (2005). Hydration Shell Exchange Dynamics During Ion Transfer across the Liquid/Liquid Interface.
315. C. A. Wick and S. S. Xantheas, *J. Phys. Chem. B*, **113**, 4141 (2009). Computational Investigation of the First Solvation Shell Structure of Interfacial and Bulk Aqueous Chloride and Iodide Ions.
316. I. Benjamin, *Science*, **261**, 1558 (1993). Mechanism and Dynamics of Ion Transfer across a Liquid-Liquid Interface.
317. I. Benjamin, *J. Phys. Chem. B*, **112**, 15801 (2008). Structure and Dynamics of Hydrated Ions in a Water-Immiscible Organic Solvent.
318. C. D. Wick and O. T. Cummings, *Chem. Phys. Lett.*, **513**, 161 (2011). Understanding the Factors That Contribute to Ion Interfacial Behavior.
319. P. B. Miranda and Y. R. Shen, *J. Phys. Chem. B*, **103**, 3292 (1999). Liquid Interfaces: A Study by Sum-Frequency Vibrational Spectroscopy.
320. Y. Rao, S. Y. Hong, N. J. Turro, and K. B. Eisenthal, *J. Phys. Chem. C*, **115**, 11678 (2011). Molecular Orientational Distribution at Interfaces Using Second Harmonic Generation.
321. A. Pohorille and I. Benjamin, *J. Chem. Phys.*, **94**, 5599 (1991). Molecular Dynamics of Phenol at the Liquid-Vapor Interface of Water.
322. P. Jedlovsky, I. Varga, and T. Gilanyi, *J. Chem. Phys.*, **119**, 1731 (2003). Adsorption of Apolar Molecules at the Water Liquid-Vapor Interface: A Monte Carlo Simulations Study of the Water-*n*-Octane System.
323. B. C. Garrett, G. K. Schenter, and A. Morita, *Chem. Rev.*, **106**, 1355 (2006). Molecular Simulations of the Transport of Molecules across the Liquid/Vapor Interface of Water.
324. R. A. Marcus, *J. Chem. Phys.*, **43**, 1261 (1965). On the Theory of Shifts and Broadening of Electronic Spectra of Polar Solutes in Polar Media.
325. N. Mataga and T. Kubota, *Molecular Interactions and Electronic Spectra*, New York, Dekker, 1970.
326. B. Martire and R. Gilbert, *Chem. Phys.*, **56**, 241 (1981). Langevin Simulation of Picosecond-Resolved Electronic Spectra in Solution.

-
327. C. Reichardt, *Solvents and Solvent Effects in Organic Chemistry*, 2nd edition, Springer-Verlag, Weinheim, 1988.
328. R. F. Loring, *J. Phys. Chem.*, **94**, 513 (1990). Statistical Mechanical Calculation of Inhomogeneously Broadened Absorption-Line Shapes in Solution.
329. N. E. Shemetulskis and R. F. Loring, *J. Chem. Phys.*, **95**, 4756 (1991). Electronic Spectra in a Polar Solvent: Theory and Simulation.
330. H. Ågren and K. V. Mikkelsen, *J. Mol. Struct.*, **234**, 425 (1991). Theory of Solvent Effects on Electronic Spectra.
331. J. G. Saven and J. L. Skinner, *J. Chem. Phys.*, **99**, 4391 (1993). A Molecular Theory of the Line-Shape - Inhomogeneous and Homogeneous Electronic-Spectra of Dilute Chromophores in Nonpolar Fluids.
332. C. Reichardt, *Chem. Rev.*, **94**, 2319 (1994). Solvatochromic Dyes as Solvent Polarity Indicators.
333. S. A. Egorov, E. Gallicchio, and B. J. Berne, *J. Chem. Phys.*, **107**, 9312 (1997). The Simulation of Electronic Absorption Spectrum of a Chromophore Coupled to a Condensed Phase Environment: Maximum Entropy Versus Singular Value Decomposition Approaches.
334. S. A. Egorov, E. Rabani, and B. J. Berne, *J. Chem. Phys.*, **108**, 1407 (1998). Vibronic Spectra in Condensed Matter: A Comparison of Exact Quantum Mechanical and Various Semiclassical Treatments for Harmonic Baths.
335. H. M. Sevan and J. L. Skinner, *J. Chem. Phys.*, **97**, 8 (1992). Molecular Theory of Transition Energy Correlations for Pairs of Chromophores in Liquids or Glasses.
336. M. D. Stephens, J. G. Saven, and J. L. Skinner, *J. Chem. Phys.*, **106**, 2129 (1997). Molecular Theory of Electronic Spectroscopy in Nonpolar Fluids: Ultrafast Solvation Dynamics and Absorption and Emission Line Shapes.
337. E. G. McRae, *J. Phys. Chem.*, **61**, 562 (1957). Theory of Solvent Effects on Molecular Electronic Spectra - Frequency Shifts.
338. N. G. Bakhshiev, *Opt. Spektrosk.*, **16**, 821 (1964). Universal Intermolecular Interactions and Their Effect on the Position of the Electronic Spectra of Molecules in Two Component Solutions
339. D. Chandler, K. S. Schweizer, and P. G. Wolynes, *Phys. Rev. Lett.*, **49**, 1100 (1982). Electronic States of a Topologically Disordered System - Exact Solution of the Mean Spherical Model for Liquids.
340. L. S. P. Mirashi and S. S. Kunte, *Spectrochimica Acta, Part A*, **45**(1147) (1989). Solvent Effects on Electronic Absorption Spectra of Nitrochlorobenzenes, Nitrophenols and Nitroanilines. 3. Excited State Dipole Moments and Specific Solute Solvent Interaction Energies Employing Bakhshiev Approach.
341. J. J. Aaron, M. Maafi, C. Párkányi, and C. Boniface, *Spectrochimica Acta, Part A*, **51**(603) (1995). Quantitative Treatment of the Solvent Effects on the Electronic Absorption and Fluorescence-Spectra of Acridines and Phenazines - The Ground and First Excited Singlet-State Dipole-Moments.
342. M. J. Kamlet, J. L. Abboud, and R. W. Taft, in *Progress in Physical Organic Chemistry*, S. G. Cohen, A. Streitwieser, and R. W. Taft (Eds.), Wiley, New York, 1981, Vol. **13**, p. 485, An Examination of Linear Solvation Energy Relationships.
343. C. Laurence, P. Nicolet, M. T. Dalati, J. L. M. Abboud, and R. Notario, *J. Phys. Chem.*, **98**, 5807 (1994). The Empirical-Treatment of Solvent Solute Interactions - 15 Years of π^* .
344. D. V. Matyushov, R. Schmid, and B. M. Ladanyi, *J. Phys. Chem. B*, **101**, 1035 (1997). A Thermodynamic Analysis of the π^* and ET(30) Polarity Scale.
345. Y. Marcus, *Chem. Soc. Rev.*, **22**, 409 (1993). The Properties of Organic Liquids That Are Relevant to Their Use as Solvating Solvents.
346. M. J. Kamlet and R. W. Taft, *J. Am. Chem. Soc.*, **98**, 377 (1976). Solvatochromic Comparison Method. 1. Beta-Scale of Solvent Hydrogen-Bond Acceptor (HBA) Basicities.

347. M. J. Kamlet, T. N. Hall, J. Boykin, and R. W. Taft, *J. Org. Chem.*, **44**, 2599 (1979). Linear Solvation Energy Relationships. 6. Additions to and Correlations with the π^* Scale of Solvent Polarities.
348. G. Saroja and A. Samanta, *Chem. Phys. Lett.*, **246**, 506 (1995). Polarity of the Micelle-Water Interface as Seen by 4-Aminophthalimide, a Solvent Sensitive Fluorescence Probe.
349. K. Kalyanasundaram and J. K. Thomas, *J. Am. Chem. Soc.*, **99**, 2039 (1977). Environmental Effects on Vibronic Band Intensities in Pyrene Monomer Fluorescence and Their Application in Studies of Micellar Systems.
350. K. Kalyanasundaram and J. K. Thomas, *J. Phys. Chem.*, **81**, 2176 (1977). Solvent-Dependent Fluorescence of Pyrene-3-Carboxaldehyde and Its Applications in Estimation of Polarity at Micelle-Water Interfaces.
351. C. A. T. Laia and S. M. B. Costa, *Phys. Chem. Chem. Phys.*, **1**, 4409 (1999). Probing the Interface Polarity of AOT Reversed Micelles Using Centro-Symmetrical Squaraine Molecules.
352. M. F. Vitha, J. D. Weckwerth, K. Odland, V. Dema, and P. W. Carr, *J. Phys. Chem.*, **100**, 18823 (1996). Study of the Polarity and Hydrogen Bond Ability of Sodium Dodecyl Sulfate Micelles by the Kamlet-Taft Solvatochromic Comparison Method.
353. M. F. Vitha and P. W. Carr, *J. Phys. Chem. B*, **102**, 1888 (1998). Study of the Polarity and Hydrogen-Bond Ability of Dodecyltrimethylammonium Bromide Micelles by the Kamlet-Taft Solvatochromic Comparison Method.
354. R. E. Riter, J. R. Kimmel, E. P. Undiks, and N. E. Levinger, *J. Phys. Chem. B*, **101**, 8292 (1997). Novel Reverse Micelles Partitioning Nonaqueous Polar Solvents in a Hydrocarbon Continuous Phase.
355. H. Wang, E. Borguet, and K. B. Eisenthal, *J. Phys. Chem.*, **101**, 713 (1997). Polarity of Liquid Interfaces by Second Harmonic Generation Spectroscopy.
356. H. F. Wang, E. Borguet, and K. B. Eisenthal, *J. Phys. Chem. B*, **102**, 4927 (1998). Generalized Interface Polarity Scale Based on Second Harmonic Spectroscopy.
357. A. A. Tamburello-Luca, P. Hébert, P. F. Brevet, and H. H. Girault, *J. Chem. Soc., Faraday Trans.*, **92**, 3079 (1996). Resonant-Surface Second-Harmonic Generation Studies of Phenol Derivatives at Air/Water and Hexane/Water Interfaces.
358. A. A. Tamburello-Luca, P. Hébert, R. Antoine, P. F. Brevet, and H. H. Girault, *Langmuir*, **13**, 4428 (1997). Optical Surface Second Harmonic Generation Study of the Two Acid/Base Equilibria of Eosin B at the Air/Water Interface.
359. W. H. Steel and R. A. Walker, *J. Am. Chem. Soc.*, **125**, 1132 (2003). Solvent Polarity at an Aqueous/Alkane Interface: The Effect of Solute Identity.
360. W. H. Steel, Y. Y. Lau, C. L. Beildeck, and R. A. Walker, *J. Phys. Chem. B*, **108**, 13370 (2004). Solvent Polarity across Weakly Associating Interfaces.
361. W. H. Steel, C. L. Beildeck, and R. A. Walker, *J. Phys. Chem. B*, **108**, 16107 (2004). Solvent Polarity Across Strongly Associating Interfaces.
362. M. Essfar, G. Guiheneuf, and J. M. Abboud, *J. Am. Chem. Soc.*, **104**, 6786 (1982). Electronic Absorption-Spectra of Polarity Polarizability Indicators in the Gas-Phase.
363. I. Benjamin, *Chem. Rev.*, **106**, 1212 (2006). Static and Dynamic Electronic Spectroscopy at Liquid Interfaces.
364. W. H. Steel, R. Nolan, F. Damkaci, and R. A. Walker, *J. Am. Chem. Soc.*, **124**, 4824 (2002). Molecular Rulers: A New Family of Surfactants for Measuring Interfacial Widths.
365. T. Uchida, A. Yamaguchi, T. Ina, and N. Teramae, *J. Phys. Chem. B*, **104**, 12091 (2000). Observation of Molecular Association at Liquid/Liquid and Solid/Liquid Interfaces by Second Harmonic Generation Spectroscopy.
366. H. J. Kim and J. T. Hynes, *J. Chem. Phys.*, **93**, 5194 (1990). Equilibrium and Nonequilibrium Solvation and Solute Electronic Structure. I. Formulation.
367. H. J. Kim and J. T. Hynes, *J. Chem. Phys.*, **93**, 5211 (1990). Equilibrium and Nonequilibrium Solvation and Solute Electronic Structure. II. Strong Coupling Limit.

-
368. P. Jacques, *J. Phys. Chem.*, **90**, 5535 (1986). On the Relative Contributions of Nonspecific and Specific Interactions to the Unusual Solvatochromism of a Typical Merocyanine Dye.
369. H. Nagatani, A. Piron, P. F. Brevat, D. J. Fermin, and H. H. Girault, *Langmuir*, **18**, 6647 (2002). Surface Second Harmonic Generation of Cationic Water-Soluble Porphyrins at the Polarized Water/1,2-Dichloroethane Interface.
370. K. S. Suslick, C. T. Chen, G. R. Meredith, and L. T. Cheng, *J. Am. Chem. Soc.*, **114**, 6928 (1992). Push-Pull Porphyrins as Nonlinear Optical-Materials.
371. S. K. Mondal, S. Yamaguchi, and T. Tahara, *J. Phys. Chem. C*, **115**, 3083 (2011). Molecules at the Air/Water Interface Experience a More Inhomogeneous Solvation Environment Than in Bulk Solvents: A Quantitative Band Shape Analysis of Interfacial Electronic Spectra Obtained by HD-ESFG.
372. D. Michael and I. Benjamin, *J. Chem. Phys.*, **107**, 5684 (1997). Electronic Spectra of Dipolar Solutes at Liquid-Liquid Interfaces. Effect of Interface Structure and Polarity.
373. D. Michael and I. Benjamin, *J. Phys. Chem.*, **102**, 5154 (1998). Structure, Dynamics and Electronic Spectrum of N,N'-Diethyl-p-Nitroaniline at Water Interfaces. A Molecular Dynamics Study.
374. I. Benjamin, *Chem. Phys. Lett.*, **287**, 480 (1998). Electronic Spectra in Bulk Water and at the Water Liquid/Vapor Interface. Effect of Solvent and Solute Polarizabilities.
375. I. Benjamin, *Chem. Phys. Lett.*, **393**, 453 (2004). Polarity of the Water/Octanol Interface.
376. F. Franks, *Water: A Comprehensive Treatise*, Plenum, New York, 1982, Vol. 4.
377. N. Nandi, K. Bhattacharyya, and B. Bagchi, *Chem. Rev.*, **100**, 2013 (2000). Dielectric Relaxation and Solvation Dynamics of Water in Complex Chemical and Biological Systems.
378. B. E. Conway, in *The Liquid State and Its Electrical Properties*, E. E. Kunhardt, L. G. Christophorou, and L. H. Luessen (Eds.), NATO ASI series B, Plenum, New York, 1988, Vol. **193**, p. 323, Electrical Aspects of Liquid/Vapor, Liquid/Liquid, and Liquid/Metal Interfaces.
379. R. R. Dogonadze, E. Kalman, A. A. Kornyshev, and J. Ulstrup, *The Chemical Physics of Solvation; Part C*, Elsevier, Amsterdam, 1988.
380. A. M. Kuznetsov, *Charge Transfer in Physics, Chemistry and Biology*, Gordon and Breach, Amsterdam, 1995.
381. I. Benjamin, *J. Phys. Chem. A*, **102**, 9500 (1998). Solvent Effects on Electronic Spectra at Liquid Interfaces. A Continuum Electrostatic Model.
382. K. Shiratori and A. Morita, *J. Chem. Phys.*, **134**, 234705 (2011). Molecular Theory on Dielectric Constant at Interfaces: A Molecular Dynamics Study of the Water/Vapor Interface.
383. R. Kubo, *J. Phys. Soc. Jpn.*, **17**, 1100 (1962). Generalized Cumulant Expansion Method.
384. I. Benjamin, *Chem. Phys. Lett.*, **515**, 56 (2011). Inhomogeneous Broadening of Electronic Spectra at Liquid Interfaces.
385. K. V. Nelson and I. Benjamin, *J. Phys. Chem. B*, **116**, 4286 (2012). Electronic Absorption Line Shapes at the Water Liquid/Vapor Interface.
386. H. Watanabe, S. Yamaguchi, S. Sen, A. Morita, and T. Tahara, *J. Chem. Phys.*, **132**, 144701 (2010). "Half-Hydration" At the Air/Water Interface Revealed by Heterodyne-Detected Electronic Sum Frequency Generation Spectroscopy, Polarization Second Harmonic Generation, and Molecular Dynamics Simulation.
387. D. W. Oxtoby, *Adv. Chem. Phys.*, **47**, 487 (1981). Vibrational Population Relaxation in Liquids.
388. J. Chesnoy and G. M. Gale, *Adv. Chem. Phys.*, **70**(part 2), 297 (1988). Vibrational Relaxation in Condensed Phases.
389. J. C. Owrutsky, D. Raftery, and R. M. Hochstrasser, *Annu. Rev. Phys. Chem.*, **45**, 519 (1994). Vibrational Relaxation Dynamics in Liquids.
390. R. M. Stratt and M. Maroncelli, *J. Phys. Chem.*, **100**, 12981 (1996). Nonreactive Dynamics in Solution: The Emerging Molecular View of Solvation Dynamics and Vibrational Relaxation.

391. M. Stratt and M. Maroncelli, *J. Phys. Chem.*, **100**, 12981 (1996). Nonreactive Dynamics in Solution – The Emerging Molecular View of Solvation Dynamics and Vibrational Relaxation.
392. E. J. Heilweil, M. P. Casassa, R. R. Cavanagh, and J. C. Stephenson, *Annu. Rev. Phys. Chem.*, **40**, 143 (1989). Picosecond Vibrational Energy Transfer Studies of Surface Adsorbates.
393. J. C. Tully, *Annu. Rev. Phys. Chem.*, **51**, 153 (2000). Chemical Dynamics at Metal Surfaces.
394. B. M. Ladanyi and R. M. Stratt, *J. Chem. Phys.*, **111**, 2008 (1999). On the Role of Dielectric Friction in Vibrational Energy Relaxation.
395. R. Rey and J. T. Hynes, *J. Chem. Phys.*, **108**, 142 (1998). Vibrational Phase and Energy Relaxation of CN^- in Water.
396. B. M. Ladanyi and R. M. Stratt, *J. Phys. Chem. A*, **102**, 1068 (1998). Short-Time Dynamics of Vibrational Relaxation in Molecular Fluids.
397. S. A. Egorov and J. L. Skinner, *J. Chem. Phys.*, **112**, 275 (2000). Vibrational Energy Relaxation of Polyatomic Solutes in Simple Liquids and Supercritical Fluids.
398. C. P. Lawrence and J. L. Skinner, *J. Chem. Phys.*, **119**, 1623 (2003). Vibrational Spectroscopy of HOD in Liquid D_2O . VI. Intramolecular and Intermolecular Vibrational Energy Flow.
399. R. D. Coalson and D. G. Evans, *Chem. Phys.*, **296**, 117 (2004). Condensed Phase Vibrational Relaxation: Calibration of Approximate Relaxation Theories with Analytical and Numerically Exact Results.
400. H. J. Bakker, *J. Chem. Phys.*, **121**, 10088 (2004). Vibrational Relaxation in the Condensed Phase.
401. A. Ma and R. M. Stratt, *J. Chem. Phys.*, **121**, 11217 (2004). Multiphonon Vibrational Relaxation in Liquids: Should It Lead to an Exponential-Gap Law?
402. J. C. Bolinger, T. J. Bixby, and P. J. Reid, *J. Chem. Phys.*, **123**, 084503 (2005). Time-Resolved Infrared Absorption Studies of the Solvent-Dependent Vibrational Relaxation Dynamics of Chlorine Dioxide.
403. G. M. Sando, K. Dahl, Q. Zhong, and J. C. Owrrutsky, *J. Phys. Chem. A*, **109**, 5788 (2005). Vibrational Relaxation of Azide in Formamide Reverse Micelles.
404. A. D. Koutselos, *J. Chem. Phys.*, **125**, 244304 (2006). Mixed Quantum-Classical Molecular Dynamics Simulation of Vibrational Relaxation of Ions in an Electrostatic Field.
405. S. Z. Li, J. R. Schmidt, and J. L. Skinner, *J. Chem. Phys.*, **125**, 244507 (2006). Vibrational Energy Relaxation of Azide in Water.
406. I. Navrotskaya and E. Geva, *J. Chem. Phys.*, **127**, 054504 (2007). Comparison between the Landau-Teller and Flux-Flux Methods for Computing Vibrational Energy Relaxation Rate Constants in the Condensed Phase.
407. S. Shigeto, Y. Pang, Y. Fang, and D. D. Dlott, *J. Phys. Chem. B*, **112**, 232 (2008). Vibrational Relaxation of Normal and Deuterated Liquid Nitromethane.
408. Y. S. Lin, S. G. Ramesh, J. M. Shorb, E. L. Sibert, and J. L. Skinner, *J. Phys. Chem. B*, **112**, 390 (2008). Vibrational Energy Relaxation of the Bend Fundamental of Dilute Water in Liquid Chloroform and D-Chloroform.
409. D. J. Shaw, M. R. Panman, and S. Woutersen, *Phys. Rev. Lett.*, **103**, 227401 (2009). Evidence for Cooperative Vibrational Relaxation of the NH^- , OH^- , and OD^- Stretching Modes in Hydrogen-Bonded Liquids Using Infrared Pump-Probe Spectroscopy.
410. A. Kandratsenka, J. Schroeder, D. Schwarzer, and V. S. Vikhrenko, *J. Chem. Phys.*, **130**, 174507 (2009). Nonequilibrium Molecular Dynamics Simulations of Vibrational Energy Relaxation of HOD in D_2O .
411. B. C. Pein, N. H. Seong, and D. D. Dlott, *J. Phys. Chem. A*, **114**, 10500 (2010). Vibrational Energy Relaxation of Liquid Aryl-Halides $\text{X-C}_6\text{H}_5$ ($\text{X} = \text{F}, \text{Cl}, \text{Br}, \text{I}$).
412. A. Eftekhari-Bafrooei and E. Borguet, *J. Am. Chem. Soc.*, **132**, 3756 (2010). Effect of Hydrogen-Bond Strength on the Vibrational Relaxation of Interfacial Water.
413. F. X. Vazquez, S. Talapatra, and E. Geva, *J. Phys. Chem. A*, **115**, 9775 (2011). Vibrational

- Energy Relaxation in Liquid HCl and DCl Via the Linearized Semiclassical Method: Electrostriction Versus Quantum Delocalization.
414. J. Yi and J. Jonas, *J. Phys. Chem.*, **100**, 16789 (1996). Raman Study of Vibrational and Rotational Relaxation Liquid Benzene-D(6) Confined to Nanoporous Silica Glasses.
415. C. Matranga and P. Guyot-Sionnest, *J. Chem. Phys.*, **112**, 7615 (2000). Vibrational Relaxation of Cyanide at the Metal/Electrolyte Interface.
416. Q. Zhong, A. P. Baronavski, and J. C. Owrutsky, *J. Chem. Phys.*, **118**, 7074 (2003). Vibrational Energy Relaxation of Aqueous Azide Ion Confined in Reverse Micelles.
417. Q. Zhong, A. P. Baronavski, and J. C. Owrutsky, *J. Chem. Phys.*, **119**, 9171 (2003). Reorientation and Vibrational Energy Relaxation of Pseudohalide Ions Confined in Reverse Micelle Water Pools.
418. A. G. Kalampounias, S. N. Yannopoulos, W. Steffen, L. I. Kirillova, and S. A. Kirillov, *J. Chem. Phys.*, **118**, 8340 (2003). Short-Time Dynamics of Glass-Forming Liquids: Phenyl Salicylate (Salol) in Bulk Liquid, Dilute Solution, and Confining Geometries.
419. S. M. Li, T. D. Shepherd, and W. H. Thompson, *J. Phys. Chem. A*, **108**, 7347 (2004). Simulations of the Vibrational Relaxation of a Model Diatomic Molecule in a Nanoconfined Polar Solvent.
420. A. M. Dokter, S. Woutersen, and H. J. Bakker, *Phys. Rev. Lett.*, **94**, 178301 (2005). Anomalous Slowing Down of the Vibrational Relaxation of Liquid Water Upon Nanoscale Confinement.
421. A. Ghosh, M. Smits, M. Sovago, J. Bredenbeck, M. Muller, and M. Bonn, *Chem. Phys.*, **350**, 23 (2008). Ultrafast Vibrational Dynamics of Interfacial Water.
422. E. L. Hommel, G. Ma, and H. C. Allen, *Analytical Sciences*, **17**, 1325 (2001). Broadband Vibrational Sum Frequency Generation Spectroscopy of a Liquid Surface.
423. A. N. Bordenyuk and A. V. Benderskii, *J. Chem. Phys.*, **122**, 134713 (2005). Spectrally- and Time-Resolved Vibrational Surface Spectroscopy: Ultrafast Hydrogen-Bonding Dynamics at D₂O/CaF₂ Interface.
424. I. Benjamin, *J. Phys. Chem. B*, **106**, 9375 (2006). Theoretical Studies of Solute Vibrational Energy Relaxation at Liquid Interfaces.
425. H. Gai and G. A. Voth, *J. Chem. Phys.*, **99**, 740 (1993). Vibrational-Energy Relaxation of Si-H Stretching Modes on the H/Si(111)1x1 Surface.
426. S. A. Egorov and J. L. Skinner, *J. Chem. Phys.*, **105**, 7047 (1996). A Theory of Vibrational Energy Relaxation in Liquids.
427. R. Rey and J. T. Hynes, *J. Chem. Phys.*, **104**, 2356 (1996). Vibrational Energy Relaxation of HOD in Liquid D₂O.
428. J. L. Skinner and K. Park, *J. Phys. Chem. B*, **105**, 6716 (2001). Calculating Vibrational Energy Relaxation Rates from Classical Molecular Dynamics Simulations: Quantum Correction Factors for Processes Involving Vibration-Vibration Energy Transfer.
429. R. M. Whitnell, K. R. Wilson, and J. T. Hynes, *J. Chem. Phys.*, **96**, 5354 (1992). Vibrational Relaxation of a Dipolar Molecule in Water.
430. L. Landau and E. Teller, *Phys. Z. Sovietunion*, **10**, 34 (1936). Theory of Sound Dispersion.
431. R. Zwanzig, *Ann. Rev. Phys. Chem.*, **16**, 67 (1965). Time-Correlation Functions and Transport Coefficients in Statistical Mechanics.
432. J. S. Bader and B. J. Berne, *J. Chem. Phys.*, **100**, 8359 (1994). Quantum and Classical Relaxation Rates from Classical Simulations.
433. J. L. Skinner, *J. Chem. Phys.*, **107**, 8717 (1997). Semiclassical Approximations to Golden Rule Rate Constants.
434. J. Viecelli, I. Chorny, and I. Benjamin, *J. Chem. Phys.*, **117**, 4532 (2002). Vibrational Relaxation at Water Surfaces.
435. I. Chorny, J. Viecelli, and I. Benjamin, *J. Phys. Chem. B*, **107**, 229 (2003). Photodissociation and Vibrational Relaxation of OCIO at Liquid Surfaces.

436. I. Chorny and I. Benjamin, *J. Mol. Liq.*, **110**, 133 (2004). Molecular Dynamics Study of the Vibrational Relaxation of OCl and OCl⁻ in the Bulk and the Surface of Water and Acetonitrile.
437. I. Benjamin, *J. Chem. Phys.*, **121**, 10223 (2004). Vibrational Relaxation at the Liquid/Liquid Interface.
438. J. Vieceli, I. Chorny, and I. Benjamin, *Chem. Phys. Lett.*, **364**, 446 (2002). Vibrational Relaxation of ICN in Bulk and Surface Chloroform.
439. R. G. Gordon, *J. Chem. Phys.*, **42**, 3658 (1965). Relations between Raman Spectroscopy and Nuclear Spin Relaxation.
440. C. Hu and R. Zwanzig, *J. Chem. Phys.*, **60**, 4354 (1974). Rotational Friction Coefficients for Spheroids with the Slipping Boundary Condition.
441. V. E. Bondybey and L. E. Brus, *J. Chem. Phys.*, **62**, 620 (1975). Rigid Cage Effect on ICI Photodissociation and B O⁺ Fluorescence in Rare-Gas Matrices.
442. J. T. Hynes, R. Kapral, and M. Weinberg, *J. Chem. Phys.*, **67**, 3256 (1977). Microscopic Boundary Layer Effects and Rough Sphere Rotation.
443. J. L. Dote, D. Kivelson, and R. N. Schwartz, *J. Phys. Chem.*, **85**, 2169 (1981). A Molecular Quasi-Hydrodynamic Free-Space Model for Molecular Rotational Relaxation in Liquids.
444. A. J. Barnes, W. J. Orville-Thomas, and J. Yarwood, *Molecular Liquids Dynamics and Interactions*, Dordrecht, Reidel, 1984.
445. G. van der Zwan and J. T. Hynes, *J. Phys. Chem.*, **89**, 4181 (1985). Time-Dependent Fluorescence Solvent Shifts, Dielectric Friction, and Nonequilibrium Solvation in Polar Solvents.
446. C. H. Wang, *Spectroscopy of Condensed Media*, New York, Academic Press, 1985.
447. B. J. Berne and R. Pecora, *Dynamic Light Scattering*, Robert E. Krieger, Malabar, 1990.
448. Y. Hu and G. R. Fleming, *J. Chem. Phys.*, **94**, 3857 (1991). Molecular Dynamics Study of Rotational Reorientation of Tryptophan and Several Indoles in Water.
449. J. M. Polson, J. D. D. Fyfe, and K. R. Jeffrey, *J. Chem. Phys.*, **94**, 3381 (1991). The Reorientation of *t*-Butyl Groups in Butylated Hydroxytoluene: A Deuterium Nuclear Magnetic Resonance Spectral and Relaxation Time Study.
450. M. Cho, S. J. Rosenthal, N. F. Scherer, L. D. Ziegler, and G. R. Fleming, *J. Chem. Phys.*, **96**, 5033 (1992). Ultrafast Solvent Dynamics: Connection between Time Resolved Fluorescence and Optical Kerr Measurements.
451. Y. J. Chang and E. W. Castner, *J. Chem. Phys.*, **99**, 113 (1993). Femtosecond Dynamics of Hydrogen-Bonding Solvents. Formamide and N-Methylformamide in Acetonitrile, DMF, and Water.
452. A. I. Krylov and R. B. Gerber, *J. Chem. Phys.*, **100**, 4242 (1994). Photodissociation of ICN in Solid and Liquid Ar⁻ Dynamics of the Cage Effect and of Excited-State Isomerization.
453. M. P. Heitz and F. V. Bright, *J. Phys. Chem.*, **100**, 6889 (1996). Probing the Scale of Local Density Augmentation in Supercritical Fluids: A Picosecond Rotational Reorientation Study.
454. G. S. Jas, Y. Wang, S. W. Pauls, C. K. Johnson, and K. Kuczera, *J. Chem. Phys.*, **107**, 8800 (1997). Influence of Temperature and Viscosity on Anthracene Rotational Diffusion in Organic Solvents: Molecular Dynamics Simulations and Fluorescence Anisotropy Study.
455. M.-L. Horng, J. A. Gardecki, and M. Maroncelli, *J. Phys. Chem. A*, **101**, 1030 (1997). Rotational Dynamics of Coumarin 153: Time-Dependent Friction, Dielectric Friction, and Other Nonhydrodynamic Effects.
456. C. J. Bardeen, J. Che, K. R. Wilson, V. V. Yakovlev, V. A. Apkarian, C. C. Martens, R. Zadayan, B. Kohler, and M. Messina, *J. Chem. Phys.*, **106**, 8486 (1997). Quantum Control of I₂ in the Gas Phase and in Condensed Phase Solid Kr Matrix.
457. A. Blokhin and M. F. Gelin, *J. Phys. Chem. B*, **101**, 236 (1997). Rotation of Nonspherical Molecules in Dense Fluids: A Simple Model Description.
458. J. S. Baskin, M. Chachisvilis, M. Gupta, and A. H. Zewail, *J. Phys. Chem. A*, **102**, 4158 (1998). Femtosecond Dynamics of Solvation: Microscopic Friction and Coherent Motion in Dense Fluids.

-
459. M. G. Kurnikova, N. Balabai, D. H. Waldeck, and R. D. Coalson, *J. Am. Chem. Soc.*, **120**, 6121 (1998). Rotational Relaxation in Polar Solvents. Molecular Dynamics Study of Solute-Solvent Interaction.
460. A. Idrissi, M. Ricci, P. Bartolini, and R. Righini, *J. Chem. Phys.*, **111**, 4148 (1999). Optical Kerr-Effect Investigation of the Reorientational Dynamics of CS₂ in CCl₄ Solutions.
461. D. J. Cook, J. X. Chen, E. A. Morlino, and R. M. Hochstrasser, *Chem. Phys. Lett.*, **309**, 221 (1999). Terahertz-Field-Induced Second-Harmonic Generation Measurements of Liquid Dynamics.
462. O. Kajimoto, *Chem. Rev.*, **99**, 355 (1999). Solvation in Supercritical Fluids: Its Effects on Energy Transfer and Chemical Reactions.
463. J. Jang and R. M. Stratt, *J. Chem. Phys.*, **112**, 7524 (2000). The Short-Time Dynamics of Molecular Reorientation in Liquids. 1. The Instantaneous Generalized Langevin Equation.
464. G. B. Dutt, T. K. Ghanty, and K. K. Singh, *J. Chem. Phys.*, **115**, 10845 (2001). Rotational Dynamics of Neutral Red in Dimethylsulfoxide: How Important Is the Solute's Charge in Causing Additional Friction?
465. J. E. Adams and A. Siavosh-Haghighi, *J. Phys. Chem. B*, **106**, 7973 (2002). Rotational Relaxation in Supercritical CO₂.
466. Y. Zhang, J. Jiang, and M. A. Berg, *J. Chem. Phys.*, **118**, 7534 (2003). Ultrafast Dichroism Spectroscopy of Anthracene in Solution. IV. Merging of Inertial and Diffusive Motions in Toluene (and References Therein for Earlier Work by the Same Authors).
467. T.-M. Chang and L. X. Dang, *J. Chem. Phys.*, **118**, 8813 (2003). On Rotational Dynamics of an NH₄⁺ Ion in Water.
468. A. C. Moskun, A. E. Jailaubekov, S. E. Bradforth, G. Tao, and R. M. Stratt, *Science*, **311**, 1907 (2006). Rotational Coherence and a Sudden Breakdown in Linear Response Seen in Room-Temperature Liquids.
469. A. Castro, E. V. Sitzmann, D. Zhang, and K. B. Eisenthal, *J. Phys. Chem.*, **95**, 6752 (1991). Rotational Relaxation at the Air/Water Interface by Time-Resolved Second Harmonic Generation.
470. K. B. Eisenthal, *J. Phys. Chem.*, **100**, 12997 (1996). Photochemistry and Photophysics of Liquid Interfaces by Second Harmonic Spectroscopy.
471. D. Zimdars, J. I. Dadap, K. B. Eisenthal, and T. F. Heinz, *J. Phys. Chem. B.*, **103**, 3425 (1999). Anisotropic Orientational Motion of Molecular Adsorbates at the Air-Water Interface.
472. R. Antoine, A. A. Tamburello-Luca, P. Hebert, P. F. Brevet, and H. H. Girault, *Chem. Phys. Lett.*, **288**, 138 (1998). Picosecond Dynamics of Eosin B at the Air/Water Interface by Time-Resolved Second Harmonic Generation: Orientational Randomization and Rotational Relaxation.
473. K. T. Nguyen, X. Shang, and K. B. Eisenthal, *J. Phys. Chem. B.*, **110**, 19788 (2006). Molecular Rotation at Negatively Charged Surfactant/Aqueous Interfaces.
474. Y. Rao, D. H. Song, N. J. Turro, and K. B. Eisenthal, *J. Phys. Chem. B*, **112**, 13572 (2008). Orientational Motions of Vibrational Chromophores in Molecules at the Air/Water Interface with Time-Resolved Sum Frequency Generation.
475. X. M. Shang, K. Nguyen, Y. Rao, and K. B. Eisenthal, *J. Phys. Chem. C*, **112**, 20375 (2008). In-Plane Molecular Rotational Dynamics at a Negatively Charged Surfactant/Aqueous Interface.
476. K. Raghavan, K. Foster, K. Motakabbir, and M. Berkowitz, *J. Chem. Phys.*, **94**, 2110 (1991). Structure and Dynamics of Water at the Pt(111) Interface: Molecular Dynamics Study.
477. D. A. Pantano and D. Laria, *J. Phys. Chem. B*, **107**, 2971 (2003). Molecular Dynamics Study of Solvation of Coumarin-314 at the Water/Air Interface.
478. I. Benjamin, *J. Chem. Phys.*, **127**, 204712 (2007). Solute Rotational Dynamics at the Water Liquid/Vapor Interface.
479. I. Benjamin, *J. Phys. Chem. C.*, **112**, 8969 (2008). Solute Orientational Dynamics at the Water/Carbon Tetrachloride Interface.

480. P. Debye, *Polar Molecules*, New York, Dover, 1945.
481. S. J. Byrnes, P. L. Geissler, and Y. R. Shen, *Chem. Phys. Lett.*, **516**, 115 (2011). Ambiguities in Surface Nonlinear Spectroscopy Calculations.
482. J. P. Ryckaert, G. Ciccotti, and H. J. C. Berendsen, *J. Comput. Phys.*, **23**, 327 (1977). Numerical Integration of the Cartesian Equations of Motion of a System with Constraints: Molecular Dynamics of n-Alkanes.
483. G. Tao and R. M. Stratt, *J. Chem. Phys.*, **125**, 114501 (2006). The Molecular Origins of Nonlinear Response in Solute Energy Relaxation: The Example of High-Energy Rotational Relaxation.
484. M. L. Johnson, C. Rodriguez, and I. Benjamin, *J. Phys. Chem. A*, **113**, 2086 (2009). Rotational Dynamics of Strongly Adsorbed Solute at the Water Surface.
485. T. W. Nee and R. Zwanzig, *J. Chem. Phys.*, **52**, 6353 (1970). Theory of Dielectric Relaxation in Polar Liquids.
486. D. S. Alavi and D. H. Waldeck, *J. Chem. Phys.*, **94**, 6196 (1991). Rotational Dielectric Friction on a Generalized Charge Distribution.
487. D. S. Alavi and D. H. Waldeck, *J. Chem. Phys.*, **98**, 3580 (1993). Erratum: Rotational Dielectric Friction on a Generalized Charge Distribution [*J. Chem. Phys.* **94**, 6196 (1991)].
488. L. R. Pratt and A. Pohorille, *Chem. Rev.*, **102**, 2671 (2002). Hydrophobic Effects and Modeling of Biophysical Aqueous Solution Interfaces.
489. M. Maroncelli, *J. Mol. Liq.*, **57**, 1 (1993). The Dynamics of Solvation in Polar Liquids.
490. P. J. Rossky and J. D. Simon, *Nature*, **370**, 263 (1994). Dynamics of Chemical Processes in Polar Solvents.
491. B. Bagchi and B. Jana, *Chem. Soc. Rev.*, **39**, 1936 (2010). Solvation Dynamics in Dipolar Liquids.
492. W. H. Thompson, *Ann. Rev. Phys. Chem.*, **62**, 599 (2011). Solvation Dynamics and Proton Transfer in Nanoconfined Liquids.
493. J. D. Simon, *Acc. Chem. Res.*, **21**, 128 (1988). Time-Resolved Studies of Solvation in Polar Media.
494. P. F. Barbara and W. Jarzeba, *Adv. Photochem.*, **15**, 1 (1990). Ultrafast Photochemical Intramolecular Charge and Excited State Solvation.
495. R. Jimenez, G. R. Fleming, P. V. Kumar, and M. Maroncelli, *Nature*, **369**, 471 (1994). Femtosecond Solvation Dynamics of Water.
496. G. C. Walker, W. Jarzeba, T. J. Kang, A. E. Johnson, and P. F. Barbara, *J. Opt. Soc. Am. B*, **7**, 1521 (1990). Ultraviolet Femtosecond Fluorescence Spectroscopy - Techniques and Applications.
497. B. M. Ladanyi and M. Maroncelli, *J. Chem. Phys.*, **109**, 3204 (1998). Mechanisms of Solvation Dynamics of Polyatomic Solutes in Polar and Nondipolar Solvents: A Simulation Study.
498. M. N. Kobrak, *J. Chem. Phys.*, **127** (2007). A Comparative Study of Solvation Dynamics in Room-Temperature Ionic Liquids.
499. D. F. Underwood and D. A. Blank, *J. Phys. Chem. A*, **107**, 9736 (2003). Ultrafast Solvation Dynamics: A View from the Solvent's Prospective Using a Novel Resonant-Pump, Nonresonant-Probe Technique.
500. N. E. Levinger, *Curr. Opin. Coll. Interf. Sci.*, **5**, 118 (2000). Ultrafast Dynamics in Reverse Micelles, Microemulsions, and Vesicles.
501. N. E. Levinger, *Science*, **298**, 1722 (2002). Water in Confinement.
502. E. M. Corbeil and N. E. Levinger, *Langmuir*, **19**, 7264 (2003). Dynamics of Polar Solvation in Quaternary Microemulsions.
503. J. A. Ingram, R. S. Moog, N. Ito, R. Biswas, and M. Maroncelli, *J. Phys. Chem. B*, **107**, 5926 (2003). Solute Rotation and Solvation Dynamics in a Room-Temperature Ionic Liquid.

-
504. H. Shirota and H. Segawa, *Langmuir*, **20**, 329 (2004). Solvation Dynamics of Formamide and N,N-Dimethylformamide in Aerosol OT Reverse Micelles.
505. M. Sakurai and A. Yoshimori, *J. Chem. Phys.*, **122**, 104509 (2005). Bandwidth Analysis of Solvation Dynamics in a Simple Liquid Mixture.
506. S. Dey, D. K. Sasmal, D. K. Das, and K. Bhattacharyya, *Chemphyschem*, **9**, 2848 (2008). A Femtosecond Study of Solvation Dynamics and Anisotropy Decay in a Catanionic Vesicle: Excitation-Wavelength Dependence.
507. T. N. Burai and A. Datta, *J. Phys. Chem. B*, **113**, 15901 (2009). Slow Solvation Dynamics in the Microheterogeneous Water Channels of Nafion Membranes.
508. H. K. Kashyap and R. Biswas, *J. Phys. Chem. B*, **114**, 254 (2010). Solvation Dynamics of Dipolar Probes in Dipolar Room Temperature Ionic Liquids: Separation of Ion-Dipole and Dipole-Dipole Interaction Contributions.
509. P. Setua, C. Ghatak, V. G. Rao, S. K. Das, and N. Sarkar, *J. Phys. Chem. B*, **116**, 3704 (2012). Dynamics of Solvation and Rotational Relaxation of Coumarin 480 in Pure Aqueous-AOT Reverse Micelle and Reverse Micelle Containing Different-Sized Silver Nanoparticles inside Its Core: A Comparative Study.
510. M. Yanagimachi, N. Tamai, and H. Masuhara, *Chem. Phys. Lett.*, **200**, 469 (1992). Solvation Dynamics of a Coumarin Dye at Liquid Solid Interface Layer - Picosecond Total Internal-Reflection Fluorescence Spectroscopic Study.
511. T. Yamashita, T. Uchida, T. Fukushima, and N. Teramae, *J. Phys. Chem. B*, **107**, 4786 (2003). Solvation Dynamics of Fluorophores with an Anthroyloxy Group at the Heptane/Water Interface as Studied by Time-Resolved Total Internal Reflection Fluorescence Spectroscopy.
512. T. Yamashita, Y. Amino, A. Yamaguchi, and N. Teramae, *Chem. Lett.*, **34**, 988 (2005). Solvation Dynamics at the Water/Mica Interface as Studied by Time-Resolved Fluorescence Spectroscopy.
513. D. Zimdars, J. I. Dadap, K. B. Eisenthal, and T. F. Heinz, *Chem. Phys. Lett.*, **301**, 112 (1999). Femtosecond Dynamics of Solvation at the Air/Water Interface.
514. D. Zimdars and K. B. Eisenthal, *J. Phys. Chem. A*, **103**, 10567 (1999). Effect of Solute Orientation on Solvation Dynamics at the Air/Water Interface.
515. A. V. Benderskii and K. B. Eisenthal, *J. Phys. Chem. B*, **104**, 11723 (2000). Effect of Organic Surfactant on Femtosecond Solvation Dynamics at the Air-Water Interface.
516. A. V. Benderskii and K. B. Eisenthal, *J. Phys. Chem. B*, **105**, 6698 (2001). Aqueous Solvation Dynamics at the Anionic Surfactant Air/Water Interface.
517. A. V. Benderskii and K. B. Eisenthal, *J. Phys. Chem. B*, **108**, 3376 (2004). Effect of Organic Surfactant on Femtosecond Solvation Dynamics at the Air-Water Interface (Vol 104, p. 11723, 2000.).
518. Y. Rao, N. J. Turro, and K. B. Eisenthal, *J. Phys. Chem. C*, **114**, 17703 (2010). Solvation Dynamics at the Air/Water Interface with Time-Resolved Sum-Frequency Generation.
519. A. V. Benderskii and K. B. Eisenthal, *J. Phys. Chem. A*, **106**, 7482 (2002). Dynamical Time Scales of Aqueous Solvation at Negatively Charged Lipid/Water Interface.
520. A. V. Benderskii, J. Henzie, S. Basu, X. M. Shang, and K. B. Eisenthal, *J. Phys. Chem. B*, **108**, 14017 (2004). Femtosecond Aqueous Solvation at a Positively Charged Surfactant/Water Interface.
521. E. A. Carter and J. T. Hynes, *J. Chem. Phys.*, **94**, 5961 (1991). Solvation Dynamics for an Ion Pair in a Polar Solvent: Time Dependent Fluorescence and Photochemical Charge Transfer.
522. T. Fonseca and B. M. Ladanyi, *J. Phys. Chem.*, **95**, 2116 (1991). Breakdown of Linear Response for Solvation Dynamics in Methanol.
523. T. Fonseca and B. M. Ladanyi, *J. Mol. Liq.*, **60**, 1 (1994). Solvation Dynamics in Methanol – Solute and Perturbation Dependence.
524. M. S. Skaf and B. M. Ladanyi, *J. Phys. Chem.*, **100**, 18258 (1996). Molecular Dynamics Simulation of Solvation Dynamics in Methanol–Water Mixtures.

525. P. L. Geissler and D. Chandler, *J. Chem. Phys.*, **113**, 9759 (2000). Importance Sampling and the Theory of Nonequilibrium Solvation Dynamics in Water.
526. A. E. Bragg, M. C. Cavanagh, and B. J. Schwartz, *Science*, **321**, 1817 (2008). Linear Response Breakdown in Solvation Dynamics Induced by Atomic Electron-Transfer Reactions.
527. P. G. Wolynes, *J. Chem. Phys.*, **86**, 5133 (1987). Linearized Microscopic Theories of Nonequilibrium Solvation.
528. I. Rips, J. Klafter, and J. Jortner, *J. Chem. Phys.*, **89**, 4288 (1988). Solvation Dynamics in Polar Liquids.
529. A. L. Nichols and D. F. Calef, *J. Chem. Phys.*, **89**, 3783 (1988). Polar Solvent Relaxation: The Mean Spherical Approximation Approach.
530. B. Bagchi, *Annu. Rev. Phys. Chem.*, **40**, 115 (1989). Dynamics of Solvation and Charge Transfer Reactions in Dipolar Liquids.
531. M. Maroncelli, *J. Chem. Phys.*, **94**, 2084 (1991). Computer Simulations of Solvation Dynamics in Acetonitrile.
532. I. Benjamin, in *Reaction Dynamics in Clusters and Condensed Phases*, J. Jortner, R. D. Levine, and B. Pullman (Eds.), Kluwer, Dordrecht, The Netherlands, 1994, p. 179, Solvation and Charge Transfer at Liquid Interfaces.
533. A. Chandra and B. Bagchi, *J. Chem. Phys.*, **94**, 3177 (1991). Inertial Effects in Solvation Dynamics.
534. I. Benjamin, *Chem. Phys.*, **180**, 287 (1994). Solvent Dynamics Following Charge Transfer at the Liquid-Liquid Interface.
535. D. Michael and I. Benjamin, *J. Phys. Chem.*, **99**, 16810 (1995). Proposed Experimental Probe of the Liquid/Liquid Interface Structure: Molecular Dynamics of Charge Transfer at the Water/Octanol Interface.
536. D. Michael and I. Benjamin, *J. Chem. Phys.*, **114**, 2817 (2001). Molecular Dynamics Computer Simulations of Solvation Dynamics at Liquid/Liquid Interfaces.
537. I. Benjamin, *Chem. Phys. Lett.*, **469**, 229 (2009). Solute Dynamics at Aqueous Interfaces.
538. D. Chandler, *J. Chem. Phys.*, **68**, 2959 (1978). Statistical Mechanics of Isomerization Dynamics in Liquids and the Transition State Approximation.
539. J. T. Hynes, in *The Theory of Chemical Reactions*, M. Baer (Ed.), CRC Press, Boca Raton, FL, 1985, Vol. 4, p. 171, The Theory of Reactions in Solution.
540. B. J. Berne, M. Borkovec, and J. E. Straub, *J. Phys. Chem.*, **92**, 3711 (1988). Classical and Modern Methods in Reaction Rate Theory.
541. R. M. Whitnell and K. R. Wilson, in *Reviews in Computational Chemistry*, K. B. Lipkowitz and D. B. Boyd (Eds.), VCH, New York, 1993, Vol. 4, p. 67, Computational Molecular Dynamics of Chemical Reactions in Solution.
542. C. Dellago, P. G. Bolhuis, F. S. Csajka, and D. Chandler, *J. Chem. Phys.*, **108**, 1964 (1998). Transition Path Sampling and the Calculation of Rate Constants.
543. B. Peters, *Molecular Simulation*, **36**, 1265 (2010). Recent Advances in Transition Path Sampling: Accurate Reaction Coordinates, Likelihood Maximisation and Diffusive Barrier-Crossing Dynamics.
544. I. Benjamin, *Prog. React. Kin. Mech.*, **27**, 87 (2002). Chemical Reaction Dynamics at Liquid Interfaces. A Computational Approach.
545. S. Z. Wang, R. Bianco, and J. T. Hynes, *Computational and Theoretical Chemistry*, **965**, 340 (2011). An Atmospherically Relevant Acid: HNO_3 .
546. Y. I. Kharkats and A. G. Volkov, *J. Electroanal. Chem.*, **184**, 435 (1985). Interfacial Catalysis: Multielectron Reactions at the Liquid-Liquid Interface.
547. W. Schmickler, *Interfacial Electrochemistry*, Oxford University Press, Oxford, 1996.
548. D. J. Fermin, H. D. Duong, Z. F. Ding, P. F. Brevet, and H. H. Girault, *Electrochem. Commun.*, **1**, 29 (1999). Solar Energy Conversion Using Dye-Sensitised Liquid Vertical Bar Liquid Interfaces.

549. R. Lahtinen, D. J. Fermin, K. Kontturi, and H. H. Girault, *J. Electroanal. Chem.*, **483**, 81 (2000). Artificial Photosynthesis at Liquid Vertical Bar Liquid Interfaces: Photoreduction of Benzoquinone by Water Soluble Porphyrin Species.
550. P. F. Barbara and E. J. J. Olson, *Adv. Chem. Phys.*, **107**, 647 (1999). Experimental Electron Transfer Kinetics in a DNA Environment.
551. A. G. Volkov and D. W. Deamer, *Liquid-Liquid Interfaces*, CRC, Boca Raton, 1996.
552. C. Wei, A. J. Bard, and M. V. Mirkin, *J. Phys. Chem.*, **99**, 16033 (1995). Scanning Electrochemical Microscopy. 31. Application of SECM to the Study of Charge-Transfer Processes at the Liquid-Liquid Interface.
553. M. Tsionsky, A. J. Bard, and M. V. Mirkin, *J. Phys. Chem.*, **100**, 17881 (1996). Scanning Electrochemical Microscopy. 34. Potential Dependence of the Electron-Transfer Rate and Film Formation at the Liquid/Liquid Interface.
554. B. Liu and M. V. Mirkin, *J. Am. Chem. Soc.*, **121**, 8352 (1999). Potential-Independent Electron Transfer Rate at the Liquid/Liquid Interface.
555. B. Liu and M. V. Mirkin, *J. Phys. Chem. B*, **106**, 3933 (2002). Electron Transfer at Liquid/Liquid Interfaces. The Effects of Ionic Adsorption, Electrolyte Concentration, and Spacer Length on the Reaction Rate.
556. J. Zhang and P. R. Unwin, *Phys. Chem. Chem. Phys.*, **4**, 3820 (2002). Microelectrochemical Measurements of Electron Transfer Rates at the Interface between Two Immiscible Electrolyte Solutions: Potential Dependence of the Ferro/Ferricyanide-7,7,8,8-Tetracyanoquinodimethane (TCNQ)/TCNQ System.
557. Y. M. Bai, P. Sun, M. Q. Zhang, Z. Gao, Z. Y. Yang, and Y. H. Shao, *Electrochimica Acta*, **48**, 3447 (2003). Effects of Solution Viscosity on Heterogeneous Electron Transfer across a Liquid/Liquid Interface.
558. D. G. Georganopoulou, M. V. Mirkin, and R. W. Murray, *Nano Letters*, **4**, 1763 (2004). SECM Measurement of the Fast Electron Transfer Dynamics between Au_{38}^{1+} Nanoparticles and Aqueous Redox Species at a Liquid/Liquid Interface.
559. M. Q. Zhang, H. Liu, H. Hu, S. B. Xie, P. Jing, Y. Kou, and Y. H. Shao, *Chemical Journal of Chinese Universities-Chinese*, **27**, 1355 (2006). Studies of Electron Transfer Reactions at the Interface between Room-Temperature Ionic Liquid+1,2-Dichloroethane Solutions and Water by Scanning Electrochemical Microscopy.
560. F. Li, A. L. Whitworth, and P. R. Unwin, *J. Electroanal. Chem.*, **602**, 70 (2007). Measurement of Rapid Electron Transfer across a Liquid/Liquid Interface from 7,7,8,8-Tetracyanoquinodimethane Radical Anion in 1,2-Dichloroethane to Aqueous Tris(2,2-Bipyridyl)-Ruthenium (III).
561. C. Shi and F. C. Anson, *J. Phys. Chem. B.*, **103**, 6283 (1999). Electron Transfer Between Reactants Located on Opposite Sides of Liquid/Liquid Interfaces.
562. C. Shi and F. C. Anson, *J. Phys. Chem. B.*, **105** (2001). Rates of Electron-Transfer Across Liquid/Liquid Interfaces. Effects of Changes in Driving Force and Reaction Reversibility.
563. K. L. Kott, D. A. Higgins, R. J. McMahon, and R. M. Corn, *J. Am. Chem. Soc.*, **115**, 5342 (1993). Observation of Photoinduced Electron Transfer at a Liquid-Liquid Interface by Optical Second Harmonic Generation.
564. R. A. W. Dryfe, Z. Ding, R. G. Wellington, P. F. Brevet, A. M. Kuznetsov, and H. H. Girault, *J. Phys. Chem. A.*, **101**, 2519 (1997). Time-Resolved Laser-Induced Fluorescence Study of Photoinduced Electron Transfer at the Water/1,2-Dichloroethane Interface.
565. K. Weidemaier, H. L. Tavernier, and M. D. Fayer, *J. Phys. Chem. B.*, **101**, 9352 (1997). Photoinduced Electron Transfer on the Surfaces of Micelles.
566. D. J. Fermin, Z. Ding, H. D. Duong, P.-F. Brevet, and H. H. Girault, *J. Phys. Chem. B.*, **102**, 10334 (1998). Photoinduced Electron Transfer at Liquid/Liquid Interfaces. 1. Photocurrent Measurements Associated with Heterogeneous Quenching of Zinc Porphyrins.
567. D. J. Fermin, H. D. Duong, Z. Ding, P.-F. Brevet, and H. H. Girault, *J. Am. Chem. Soc.*, **121**, 10203 (1999). Photoinduced Electron Transfer at Liquid/Liquid Interfaces. Part III. Photoelectrochemical Responses Involving Porphyrin Ion Pairs.

568. H. Jensen, J. J. Kakkassery, H. Nagatani, D. J. Fermin, and H. H. Girault, *J. Am. Chem. Soc.*, **122**, 10943 (2000). Photoinduced Electron Transfer at Liquid/Liquid Interfaces. Part IV. Orientation and Reactivity of Zinc Tetra(4-Carboxyphenyl) Porphyrin Self-Assembled at the Water/1,2-Dichloroethane Junction.
569. N. Eugster, D. J. Fermin, and H. H. Girault, *J. Phys. Chem. B*, **106**, 3428 (2002). Photoinduced Electron Transfer at Liquid/Liquid Interfaces. Part VI. On the Thermodynamic Driving Force Dependence of the Phenomenological Electron-Transfer Rate Constant.
570. N. Eugster, D. J. Fermin, and H. H. Girault, *J. Am. Chem. Soc.*, **125**, 4862 (2003). Photoinduced Electron Transfer at Liquid/Liquid Interfaces: Dynamics of the Heterogeneous Photoreduction of Quinones by Self-Assembled Porphyrin Ion Pairs.
571. E. A. McArthur and K. B. Eisenthal, *J. Am. Chem. Soc.*, **128**, 1068 (2006). Ultrafast Excited-State Electron Transfer at an Organic Liquid/Aqueous Interface.
572. S. Ghosh, K. Sahu, S. K. Mondal, P. Sen, and K. Bhattacharyya, *J. Chem. Phys.*, **125**, 054509 (2006). A Femtosecond Study of Photoinduced Electron Transfer from Dimethylaniline to Coumarin Dyes in a Cetyltrimethylammonium Bromide Micelle.
573. S. Ghosh, S. K. Mondal, K. Sahu, and K. Bhattacharyya, *J. Phys. Chem. A*, **110**, 13139 (2006). Ultrafast Electron Transfer in a Nanocavity. Dimethylaniline to Coumarin Dyes in Hydroxypropyl Gamma-Cyclodextrin.
574. S. Ghosh, S. K. Mondal, K. Sahu, and K. Bhattacharyya, *J. Chem. Phys.*, **126**, 204708 (2007). Ultrafast Photoinduced Electron Transfer from Dimethylaniline to Coumarin Dyes in Sodium Dodecyl Sulfate and Triton X-100 Micelles.
575. A. Chakraborty, D. Chakrabarty, P. Hazra, D. Seth, and N. Sarkar, *Chem. Phys. Lett.*, **382**, 508 (2003). Photoinduced Intermolecular Electron Transfer between Coumarin Dyes and Electron Donating Solvents in Cetyltrimethylammonium Bromide (CTAB) Micelles: Evidence for Marcus Inverted Region.
576. A. Chakraborty, D. Seth, D. Chakrabarty, P. Hazra, and N. Sarkar, *Chem. Phys. Lett.*, **405**, 18 (2005). Photoinduced Electron Transfer from Dimethyl Aniline to Coumarin Dyes in Reverse Micelles.
577. A. Chakraborty, D. Seth, P. Setua, and N. Sarkar, *J. Phys. Chem. B*, **110**, 16607 (2006). Photoinduced Electron Transfer in a Protein-Surfactant Complex: Probing the Interaction of SDS with BSA.
578. A. Chakraborty, D. Seth, P. Setua, and N. Sarkar, *J. Chem. Phys.*, **124**, 074512 (2006). Photoinduced Electron Transfer from N,N-Dimethylaniline to 7-Amino Coumarins in Protein-Surfactant Complex: Slowing Down of Electron Transfer Dynamics Compared to Micelles.
579. M. Tsionsky, A. J. Bard, and M. V. Mirkin, *J. Am. Chem. Soc.*, **119**, 10785 (1997). Long-Range Electron Transfer through a Lipid Monolayer at the Liquid/Liquid Interface.
580. Y. B. Zu, F. R. F. Fan, and A. J. Bard, *J. Phys. Chem. B*, **103**, 6272 (1999). Inverted Region Electron Transfer Demonstrated by Electrogenerated Chemiluminescence at the Liquid/Liquid Interface.
581. Z. Ding, B. M. Quinn, and A. J. Bard, *J. Phys. Chem. B*, **105**, 6367 (2001). Kinetics of Heterogeneous Electron Transfer at Liquid/Liquid Interfaces as Studied by SECM.
582. H. Jensen, D. J. Fermin, and H. H. Girault, *Phys. Chem. Chem. Phys.*, **3**, 2503 (2001). Photoinduced Electron Transfer at Liquid/Liquid Interfaces. Part V. Organisation of Water-Soluble Chlorophyll at the Water/1,2-Dichloroethane Interface.
583. K. Yoshihara, *Adv. Chem. Phys.*, **107**, 371 (1999). Ultrafast Intermolecular Electron Transfer in Solution.
584. E. W. Castner, D. Kennedy, and R. J. Cave, *J. Phys. Chem. A*, **104**, 2869 (2000). Solvent as Electron Donor: Donor/Acceptor Electronic Coupling is a Dynamical Variable.
585. V. O. Saik, A. A. Goun, and M. D. Fayer, *J. Chem. Phys.*, **120**, 9601 (2004). Photoinduced Electron Transfer and Geminate Recombination for Photoexcited Acceptors in a Pure Donor Solvent.

-
586. A. Chakraborty, D. Seth, D. Chakrabarty, and N. Sarkar, *Spectrochimica Acta Part A-Molecular and Biomolecular Spectroscopy*, **64**, 801 (2006). Photoinduced Intermolecular Electron Transfer from Dimethyl Aniline to 7-Amino Coumarin Dyes in the Surface of Beta-Cyclodextrin.
587. R. A. Marcus, *J. Chem. Phys.*, **43**, 679 (1965). On the Theory of Electron-Transfer Reactions. VI. Unified Treatment for Homogeneous and Electrode Reactions.
588. J. Ulstrup, *Charge Transfer Processes in Condensed Media*, Springer, Berlin, 1979.
589. M. D. Newton and N. Sutin, *Ann. Rev. Phys. Chem.*, **35**, 437 (1984). Electron Transfer Reactions in Condensed Phases.
590. M. J. Weaver, *Chem. Rev.*, **92**, 463 (1992). Dynamical Solvent Effects on Activated Electron-Transfer Reactions: Principles, Pitfalls, and Progress.
591. R. A. Marcus, *Ann. Rev. Phys. Chem.*, **15**, 155 (1964). Chemical and Electrochemical Electron-Transfer Theory.
592. A. M. Kuznetsov and Y. I. Kharkats, in *The Interface Structure and Electrochemical Processes at the Boundary between Two Immiscible Liquids*, V. E. Kazarinov (Ed.), Springer, Berlin, 1987, p. 11, Problems of a Quantum Theory of Charge Transfer Reactions.
593. R. A. Marcus, *J. Phys. Chem.*, **94**, 1050 (1990). Reorganization Free Energy for Electron Transfers at Liquid-Liquid and Dielectric Semiconductor-Liquid Interfaces.
594. R. A. Marcus, *J. Phys. Chem.*, **94**, 4152 (1990). Theory of Electron-Transfer Rates across Liquid-Liquid Interfaces.
595. R. A. Marcus, *J. Phys. Chem.*, **95**, 2010 (1991). Theory of Electron-Transfer Rates across Liquid-Liquid Interfaces. 2. Relationships and Application.
596. C. Zener, *Proc. R. Soc. London, Ser. A*, **137**, 696 (1932). Non-Adiabatic Crossing of Energy Levels.
597. Y. I. Kharkats, *Elektrokhimiya*, **12**, 1370 (1976). On the Calculation of Probability of Electron Transfer through the Interface between Two Dielectric Media.
598. I. Benjamin and Y. I. Kharkats, *Electrochimica Acta*, **44**, 133 (1998). Reorganization Free Energy for Electron Transfer Reactions at Liquid/Liquid Interfaces.
599. J. K. Hwang and A. Warshel, *J. Am. Chem. Soc.*, **109**, 715 (1987). Microscopic Examination of Free-Energy Relationships for Electron Transfer in Polar Solvents.
600. G. King and A. Warshel, *J. Chem. Phys.*, **93**, 8682 (1990). Investigation of the Free Energy Functions for Electron Transfer Reactions.
601. R. A. Kuharski, J. S. Bader, D. Chandler, M. Sprik, M. L. Klein, and R. W. Impey, *J. Chem. Phys.*, **89**, 3248 (1988). Molecular Model for Aqueous Ferrous-Ferric Electron Transfer.
602. E. A. Carter and J. T. Hynes, *J. Phys. Chem.*, **93**, 2184 (1989). Solute-Dependent Solvent Force Constants for Ion Pairs and Neutral Pairs in Polar Solvent.
603. R. A. Marcus, *J. Chem. Phys.*, **24**, 979 (1956). Electrostatic Free Energy and Other Properties of States Having Nonequilibrium Polarization.
604. J. C. Rasaiah and J. J. Zhu, *J. Chem. Phys.*, **129**, 214503 (2008). Reaction Coordinates for Electron Transfer Reactions.
605. M. Tachiya, *J. Phys. Chem.*, **93**, 7050 (1989). Relation between the Electron-Transfer Rate and the Free Energy Change of Reaction.
606. I. Benjamin, *J. Phys. Chem.*, **95**, 6675 (1991). Molecular Dynamics Study of the Free Energy Functions for Electron Transfer Reactions at the Liquid-Liquid Interface.
607. J. Vieceli and I. Benjamin, *Chem. Phys. Lett.*, **385**, 79 (2004). Electron Transfer at the Interface between Water and Self-Assembled Monolayers.
608. D. V. Matyushov and G. A. Voth, *J. Chem. Phys.*, **113**, 5413 (2000). Modeling the Free Energy Surfaces of Electron Transfer in Condensed Phases.
609. I. Benjamin, in *Structure and Reactivity in Aqueous Solution: ACS Symposium Series 568*, C. J. Cramer and D. G. Truhlar (Eds.), American Chemical Society, Washington,

- DC, 1994, p. 409, A Molecular Model for an Electron Transfer Reaction at the Water/1,2-Dichloroethane Interface.
610. I. Benjamin, *Acc. Chem. Res.*, **28**, 233 (1995). Theory and Computer Simulations of Solvation and Chemical Reactions at Liquid Interfaces.
611. Y. Rao, M. Xu, S. Jockusch, N. J. Turro, and K. B. Eisenthal, *Chem. Phys. Lett.*, **544**, 1 (2012). Dynamics of Excited State Electron Transfer at a Liquid Interface Using Time-Resolved Sum Frequency Generation.
612. M. Makosza, *Pure Appl. Chem.*, **72**, 1399 (2000). Phase Transfer Catalysis. A General Green Methodology in Organic Synthesis.
613. D. Albanese, *Catalysis Reviews-Science and Engineering*, **45**, 369 (2003). Liquid-Liquid Phase Transfer Catalysis: Basic Principles and Synthetic Applications (Reprinted from Interfacial Catalysis, p. 203–226, 2003).
614. C. A. Eckert, C. L. Liotta, D. Bush, J. S. Brown, and J. P. Hallett, *J. Phys. Chem. B.*, **108**, 18108 (2004). Sustainable Reactions in Tunable Solvents.
615. D. Albanese, *Mini-Reviews in Organic Chemistry*, **3**, 195 (2006). New Applications of Phase Transfer Catalysis in Organic Synthesis.
616. Y. H. Shao, M. V. Mirkin, and J. F. Rusling, *J. Phys. Chem. B*, **101**, 3202 (1997). Liquid/Liquid Interface as a Model System for Studying Electrochemical Catalysis in Microemulsions. Reduction of Trans-1,2-Dibromocyclohexane with Vitamin B-12.
617. C. K. Ingold, *Structure and Mechanism in Organic Chemistry*, 2nd edition, Cornell University, Ithaca, NY, 1969.
618. A. Warshel and R. M. Weiss, *J. Am. Chem. Soc.*, **102**, 6218 (1980). An Empirical Valence Bond Approach for Comparing Reactions in Solutions and in Enzymes.
619. J. K. Hwang, G. King, S. Creighton, and A. Warshel, *J. Am. Chem. Soc.*, **110**, 5297 (1988). Simulation of Free-Energy Relationships and Dynamics of S_N2 Reactions in Aqueous-Solution.
620. J. Chandrasekhar, S. F. Smith, and W. L. Jorgensen, *J. Am. Chem. Soc.*, **106**, 3049 (1984). S_N2 Reaction Profiles in the Gas-Phase and Aqueous-Solution.
621. W. L. Jorgensen and J. K. Buckner, *J. Phys. Chem.*, **90**, 4651 (1986). Effect of Hydration on the Structure of an S_N2 Transition-State.
622. J. R. Mathis, R. Bianco, and J. T. Hynes, *J. Mol. Liq.*, **61**, 81 (1994). On the Activation Free-Energy of the $Cl^- + CH_3Cl$ S_N2 Reaction in Solution.
623. W.-P. Hu and D. G. Truhlar, *J. Am. Chem. Soc.*, **116**, 7797 (1994). Modeling Transition State Solvation at the Single-Molecule Level: Test of Correlated Ab Initio Predictions against Experiment for the Gas-Phase S_N2 Reaction of Microhydrated Fluoride with Methyl Chloride.
624. G. Vayner, K. N. Houk, W. L. Jorgensen, and J. I. Brauman, *J. Am. Chem. Soc.*, **126**, 9054 (2004). Steric Retardation of S_N2 Reactions in the Gas Phase and Solution.
625. G. I. Almerindo and J. R. Pliego, *Chem. Phys. Lett.*, **423**, 459 (2006). Rate Acceleration of S_N2 Reactions through Selective Solvation of the Transition State.
626. J. R. Pliego, *J. Phys. Chem. B*, **113**, 505 (2009). First Solvation Shell Effects on Ionic Chemical Reactions: New Insights for Supramolecular Catalysis.
627. Y. Kim, C. J. Cramer, and D. G. Truhlar, *J. Phys. Chem. A*, **113**, 9109 (2009). Steric Effects and Solvent Effects on S_N2 Reactions.
628. D. Landini, A. Maia, and A. Rampoldi, *J. Org. Chem.*, **54**, 328 (1989). Dramatic Effect of the Specific Solvation on the Reactivity of Quaternary Ammonium Fluorides and Poly(Hydrogen Fluorides), (HF) in Media of Low Polarity.
629. A. Maia, *Pure Appl. Chem.*, **67**, 697 (1995). Anion Activation by Quaternary Onium Salts and Polyether Ligands in Homogeneous and Heterogeneous Systems.
630. D. Albanese, D. Landini, A. Maia, and M. Penso, *Industrial & Engineering Chemistry Research*, **40**, 2396 (2001). Key Role of Water for Nucleophilic Substitutions in Phase-Transfer-Catalyzed Processes: A Mini-Review.

-
631. D. K. Bohme and A. B. Raksit, *Can. J. Chem.*, **63**, 3007 (1985). Gas-Phase Measurements of the Influence of Stepwise Solvation on the Kinetics of S_N2 Reactions of Solvated F^- with CH_3Cl and CH_3Br and of Solvated Cl^- with CH_3Br .
632. X. G. Zhao, S. C. Tucker, and D. G. Truhlar, *J. Am. Chem. Soc.*, **113**, 826 (1991). Solvent and Secondary Kinetic Isotope Effects for the Microhydrated S_N2 Reaction of $Cl^-(H_2O)_N$ with CH_3Cl .
633. M. Re and D. Laria, *J. Chem. Phys.*, **105**, 4584 (1996). Solvation Effects on a Model S_N2 Reaction in Water Clusters.
634. J. M. Hayes and S. M. Bachrach, *J. Phys. Chem. A*, **107**, 7952 (2003). Effect of Micro and Bulk Solvation on the Mechanism of Nucleophilic Substitution at Sulfur in Disulfides.
635. K. V. Nelson and I. Benjamin, *J. Phys. Chem. C*, **114**, 1154 (2010). A Molecular Dynamics-Empirical Valence Bond Study of an S_N2 Reaction at the Water/Chloroform Interface.
636. I. Benjamin, *J. Chem. Phys.*, **129**, 074508 (2008). Empirical Valence Bond Model of an S_N2 Reaction in Polar and Non-Polar Solvents.
637. S. C. Tucker and D. G. Truhlar, *J. Am. Chem. Soc.*, **112**, 3338 (1990). A 6-Body Potential-Energy Surface for the S_N2 Reaction $Cl^-(G)+CH_3Cl(G)$ and a Variational Transition-State-Theory Calculation of the Rate-Constant.
638. I. Benjamin, *J. Chem. Phys.*, **103**, 2459 (1995). Photodissociation of ICN in Liquid Chloroform; Molecular Dynamics of Ground and Excited State Recombination, Cage Escape and Hydrogen Abstraction Reaction.
639. J. J. I. Timoneda and J. T. Hynes, *J. Phys. Chem.*, **95**, 10431 (1991). Nonequilibrium Free-Energy Surfaces for Hydrogen-Bonded Proton-Transfer Complexes in Solution.
640. R. S. Mulliken, C. A. Rieke, D. Orloff, and H. Orloff, *J. Chem. Phys.*, **17**, 1248 (1949). Formulas and Numerical Tables for Overlap Integrals.
641. K. V. Nelson and I. Benjamin, *J. Chem. Phys.*, **130**, 194502 (2009). Microhydration Effects on a Model S_N2 Reaction in a Nonpolar Solvent.
642. B. J. Gertner, K. R. Wilson, and J. T. Hynes, *J. Chem. Phys.*, **90**, 3537 (1989). Nonequilibrium Solvation Effects on Reaction-Rates for Model S_N2 Reactions in Water.
643. B. J. Gertner, J. P. Bergsma, K. R. Wilson, S. Lee, and J. T. Hynes, *J. Chem. Phys.*, **86**, 1377 (1987). Nonadiabatic Solvation Model for S_N2 Reactions in Polar Solvents.
644. K. V. Nelson and I. Benjamin, *J. Phys. Chem. C*, **115**, 2290 (2011). Effect of a Phase Transfer Catalyst on the Dynamics of an S_N2 Reaction. A Molecular Dynamics Study.